

HIGH-STRENGTH, HIGH-CONDUCTIVITY, TWO-PHASE MATERIALS

By

JEFFREY TODD WOOD, M.A.Sc.

A Thesis

Submitted to the School of Graduate Studies

in Partial Fulfilment of the Requirements

for the Degree

Doctor of Philosophy

McMaster University

© Copyright by Jeffrey Todd Wood, December, 1994

HIGH-STRENGTH, HIGH-CONDUCTIVITY, TWO-PHASE MATERIALS

DOCTOR OF PHILOSOPHY (1994)
(Materials Science)

McMaster University
Hamilton, Ontario

TITLE: High-Strength, High-Conductivity, Two-Phase Materials

AUTHOR: Jeffrey Todd Wood, B.A.Sc. (University of Waterloo)
M.A.Sc. (University of Waterloo)

SUPERVISOR: Professor J.D. Embury

NUMBER OF PAGES: xv, 154

Abstract

Heavily deformed, two-phase materials have been shown to exhibit strengths well in excess of the rule-of-mixtures prediction using the bulk properties of the constituents. The work described in this thesis investigates a number of aspects regarding high-strength, high-conductivity, two-phase materials. Microstructural observations and mechanical testing were used to examine the process of co-deformation, the evolution of mechanical properties, and the thermal stability of these heavily deformed structures. Materials selection procedures for the design of high-field magnet coils were developed.

The sustained co-deformation of the two-phases leads to the conclusion that the second phase behaves as a shearable obstacle to dislocation motion. The increase in strength displayed by the two-phase material over the bulk constituent strengths may be explained by existing models of particle shearing if increased interfacial energy due to residual stress is accounted for. The increased work hardening displayed by copper-silver alloys subjected to intermediate annealing treatments is explained by a continuum description of the evolution of slip line length.

The combination of materials selection procedures and investigations into the strengthening and resistive mechanisms have led to a new approach to the design of non-uniform composite materials to optimize strength and resistivity in two-phase materials.

Acknowledgements

The author would like to express his sincere gratitude to Dr. J. D. Embury for both his guidance and unending patience during this work. The time I have spent at McMaster has been especially enjoyable and enlightening.

Thanks are due to Mrs. Mary Ann Hill, and Drs. D. M. Parkin, M. F. Stevens, L. J. Campbell, M. E. Hawley, M. F. Hundley and S. I. Hong of Los Alamos National Lab. for advice, encouragement, and access to a variety of experimental equipment not available here at McMaster. Their contributions to this work are greatly appreciated. At McMaster, the help of Mrs. Teresa Castillo with TEM, and Mr. J. D. Garrett with materials preparation are thankfully acknowledged. Further thanks are due to Los Alamos National Lab and the National High Magnetic Field Lab for financial support during the writing of this thesis.

Finally, the author wishes to thank his fellow graduate students for helpful discussions, experimental advice, and the occasional game of baseball to keep things in perspective.

Dedication

To my wife Brenda,

who, in these three years, has provided the ideal combination of her love, her patience, and her drive to succeed, and without whom this would not have been possible.

Table of Contents

Abstract	iii
Acknowledgements	iv
Dedication	v
List of Figures	x
List of Tables	xv
1. Introduction	1
2. Literature Review	4
High-Field, Pulsed Magnet Design	4
The Current Loop	5
The Simple Solenoid	7
High-Field, Pulsed Magnets	13
High-Strength, High-Conductivity Materials	16
Strength of Materials	17
Effects of Dislocation Density	19
Dislocation Generation and Accumulation	23
Internal Energy Storage	26
Macroscopic Strengthening	29
Fe-Fe ₃ C Wires	30

Copper-Niobium Wires	32
Copper-Silver Wires	36
Stability of Two-Phase Wires	39
Elastic Stored Energy	40
Resistivity in Metals	42
Materials Selection	47
Deriving Performance Indices	48
Selection Charts	49
Multiple Objectives	51
3. Experimental Procedures	53
Materials	53
Pure Materials	53
Copper-Niobium Alloys	53
Copper-Silver Alloy	56
Experimental Objectives	56
Co-deformation of Copper-Niobium Wires	57
Evolution of Electrical Resistivity	58
Morphological Stability of CuNb and CuAg Wires	59
Intermediate Heat Treatments	60
Investigation of the Strengthening Mechanisms	60
Experimental Techniques	61
Wire Drawing	61
Metallography	64
Extracted Niobium Filaments	65
Resistivity Measurements	65

Texture Measurements	67
Dilatometry	67
Mechanical Testing	67
4. Experimental Results	69
Microstructural Evolution	69
Copper-Silver Wires	69
Copper-Niobium Wires	72
Extracted Niobium Filaments	72
Dimensional and Microstructural Stability	77
Dilatometry	77
Isochronal Annealing	80
Intermediate Annealing Treatments	81
Mechanical Testing	84
Resistivity	88
5. Discussion	91
The Codeformation and Strengthening of Two-Phase Alloys	91
Starting Materials	92
Alignment	93
Refinement	102
Continuum Considerations	104
Scale-Dependent Considerations	109
Microstructural and Dimensional Stability	118
The Energy of Strained Interfaces	124
Intermediate Heat Treatments	125

Electrical Resistivity	127
Solute Concentration	128
Dislocation Density	129
Interface Scattering	129
6. Materials Selection for Pulsed Magnet Design	132
Selection Chart Development	132
Processing and Selection Charts	136
Alternate Processing Technologies	138
7. Conclusions and Future Work	144
References	150

List of Figures

Figure 2-1: The current loop.	6
Figure 2-2: The geometry of a simple solenoid.	8
Figure 2-3: The field factor, $F(\alpha, \beta)$, plotted as a function of α and β	9
Figure 2-4: The geometry of a current sheet.	11
Figure 2-5: Profiles of a) field strength and b) tangential stress as a function of position in the coil.	12
Figure 2-6: A fibreglass reinforced, copper coil designed for 50 T a) before and b) after testing to destruction at 57 T.	15
Figure 2-7: Dislocation bowing by the Orowan mechanism.	21
Figure 2-8: a) The curvature arising from an array of like edge dislocations. b) A random array of edge dislocations.	24
Figure 2-9: a) Characteristic slip distances and b) dislocation density as a function of shear strain from Ashby (1971)	25
Figure 2-10: a) The increase in surface area to volume ratio for an initially cubic grain subject to various modes of deformation. b) The predicted increase in flow stress due to the increased stored energy.	28
Figure 2-11: The effect of initial microstructural scale on the evolution of flow stress in drawn pearlite (Embury and Fisher, 1966).	31
Figure 2-12: a) The influence of niobium volume fraction and imposed strain on the tensile strength of drawn Cu-Nb wires. b) The effect of initial scale on the evolution of tensile strength.	33

Figure 2-13: Normalized strength versus normalized filament spacing for Cu-Nb and Cu-Ta wires. (See Spitzig and Krotz, 1988)	34
Figure 2-14: Strength versus interphase spacing for materials made by vapour deposition and by deformation processing.	35
Figure 2-15: Elastic modulus and internal friction versus mean fibre diameter for drawn copper-silver wires.	37
Figure 2-16: Hardness, strength and electrical conductivity as a function of strain and intermediate heat treatment.	38
Figure 2-17: A schematic representation of the spheroidization process.	41
Figure 2-18: Resistivity versus temperature for a typical metal. Θ is the Debye temperature.	44
Figure 2-19: A materials selection chart based on the strength and Young's modulus of the material.	50
Figure 3-1: The copper-niobium phase diagram after Okamoto and Massalski. (1991) .	55
Figure 3-2: The copper-silver phase diagram after Subramanian and Perepezko, (1993).	55
Figure 3-3: The nominal imposed temperature profile of the dilatometry experiments.	59
Figure 3-4: Geometry of the a) Cu-24wt%Ag and b) Cu-18wt%Nb tensile samples. .	62
Figure 3-5: Drawing of the major components of the wire drawing apparatus.	63
Figure 3-6: Schematic diagram showing the vacuum process for preparing niobium filament samples for the SEM.	66
Figure 3-7: Schematic representation of the electrical connections for the 4-probe, electrical resistivity measurement	66
Figure 4-1: An optical micrograph of the as-cast Cu-24wt%Ag alloy. The structure consists of primary copper dendrites surrounded by copper-silver eutectic.	70

Figure 4-2: TEM micrographs of a) transverse and b) longitudinal sections of the Cu-24wt%Ag wire drawn to a strain of 4.3	71
Figure 4-3: TEM micrographs of a) transverse and b) longitudinal sections of the drawn Cu-15wt%Nb wire.	73
Figure 4-4: A transverse SEM micrograph of the drawn Cu-18wt%Nb wire with the copper matrix etched to reveal the niobium filaments.	74
Figure 4-5: SEM micrographs of niobium extracted from the Cu-1wt%Nb wire in the a) as-cast condition and b) after a strain of 5.	75
Figure 4-6: A TEM micrograph of a niobium filament extracted after a strain of 5. The filament is dislocation free.	76
Figure 4-7: An AFM image of a niobium filament extracted after a strain of 5. The striations make an angle of 57° with the filament axis.	76
Figure 4-8: Expansion (in parts per million) versus temperature for a) annealed copper, b) drawn copper, c) drawn copper-silver, and d) drawn copper-niobium.	78
Figure 4-9: Examples of microstructural instability in annealed copper-silver wires. a) spheroidization, b) reprecipitation, and c) discontinuous coarsening.	82
Figure 4-10: Tensile data for Cu-24wt%Ag and Cu-18wt%Nb in the as-drawn condition, and after recovery at 250°C for one hour.	86
Figure 4-11: Resistivity versus temperature and strain in drawn, pure copper.	89
Figure 4-12: Resistivity versus temperature and strain for drawn Cu-1wt% Nb.	89
Figure 4-13: Resistivity versus temperature and strain for drawn Cu-24wt%Ag.	90
Figure 4-14: The low temperature ($<10\text{K}$) resistivity plateau for Cu, Cu-1wt%Nb, and Cu-24wt%Ag as a function of strain.	90
Figure 5-1: Experimental data of Spitzig and Krotz, (1987) for ultimate strengths of copper, niobium and two copper niobium composites.	93

Figure 5-2: The evolution of the misorientation angle, θ , with strain.	95
Figure 5-3: The evolution of interphase spacing with strain during the alignment process.	96
Figure 5-4: The change in mean slip line length with strain for various initial misorientation angles.	98
Figure 5-5: The shape of the flow curve predicted during the alignment phase by an inverse square root relationship.	99
Figure 5-6: The generation of geometrically necessary dislocations to accommodate the curvature due to a non-deforming second phase. (from Ashby, 1971)	100
Figure 5-7: Extracted niobium filaments after various strains and heat treatments. a) $\epsilon=3$, b) $\epsilon=4$, c) $\epsilon=5$, d) $\epsilon=5$ extracted after annealing for one hour at 500°C.	106
Figure 5-8: Schematic diagram of a dislocation bowing through obstacles of different spacings.	111
Figure 5-9: The difference in strain across an interface caused by unequal Burger's vectors.	114
Figure 5-10: An AFM image of a niobium filament extracted from the wire after an imposed strain of 5	115
Figure 5-11: The evolution with strain of the surface area to volume ratio of a drawn cylinder.	117
Figure 5-12: Spheroidization of a) niobium and b) silver filaments in a copper matrix after exposure to 400°C for one hour.	119
Figure 5-13: Spheroidization times for copper-niobium and copper-silver wires as a function of temperature predicted by Equation (5-22).	121
Figure 5-14: Discontinuous coarsening in a Cu-24wt%Ag wire after exposure to 450°C for one hour	122

Figure 5-15: A schematic representation of the discontinuous coarsening reaction from Livingston and Cahn, (1974).	123
Figure 5-16: A two-stage, linear hardening model base on the data of Sakai et al. (1992). See text for a description of the modelling methodology.	126
Figure 5-17: The effect of second phase radius on the concentration of niobium atoms in the copper matrix.	128
Figure 5-18: The models of Dingle (1950) and Sondheimer (1952), Skomski et al. (1992), and experimental data for resistivity as a function of microstructural scale. . .	130
Figure 5-19: A collection of data for high-strength, high-conductivity, two-phase materials showing the general inverse relationship between strength and conductivity . . .	131
Figure 6-1: The proposed selection chart for high-field, pulsed magnets.	134
Figure 6-2: The data of Frommeyer and Wassermann (1975a, b) showing the effects of cold work on single and two-phase materials on the materials selection chart.	135
Figure 6-3: Modelled strength and resistivity data plotted a) as functions of strain and b) on the materials selection chart.	137
Figure 6-4: The data of Sakai et al. (1992) for copper-silver wires subjected to intermediate heat treatments plotted on the pulsed magnet material selection chart.	138
Figure 6-5 : Micrographs of the “jelly-roll” structured copper-niobium composite. . .	140
Figure 6-6: A schematic drawing of the “jelly-roll” fabrication technique.	141
Figure 6-7: The modelled results of the “jelly-roll” structure compared to the conventionally cast and drawn material.	143

List of Tables

Table 2-1: Strength data for some selected, high-strength materials.	18
Table 2-2: Debye temperatures for some pure materials.	43
Table 3-1: Analysis of impurities in the as-received copper (in ppm) supplied by Copper and Brass Sales.	54
Table 3-2: Analysis of impurities in the as-received niobium (in ppm) supplied by Johnson Matthey.	54
Table 4-1: Vickers hardness data from current experiments and literature for copper-silver wires subjected to intermediate heat treatments.	82
Table 4-2: Tensile data for Cu-18wt%Nb measured at Los Alamos National Lab.	87

1. Introduction

In the past 40 years, extraordinary effort has been made in the development of composite materials and also in producing materials with yield strengths which are high fractions of the theoretical strength (Kelly and Macmillan, 1986). The production of composite materials may exploit new technology such as vapour deposition, or may rely on conventional forming processes such as wire drawing. An important aspect of composite materials is the potential of controlling more than one engineering parameter simultaneously. An example of this is in the wire required for a high-field solenoid where both high mechanical strength and high electrical conductivity are required. Much of the present work has been conducted in collaboration with Los Alamos National Laboratory with the goal to produce wires with this combination of properties.

The National High Magnetic Field Laboratory (NHMFL) facility at Los Alamos, New Mexico, is dedicated to the generation of long pulsed (100ms), high (60T) magnetic fields via capacitively driven coils, and short pulsed, explosively driven flux compression magnets (1ms, 100-200T). As scientists strive to generate higher and higher magnetic fields for research in all branches of science, a unique class of problems in materials science has been created. The generation of very high magnetic fields requires winding materials that have simultaneously high electrical conductivity to avoid resistive heating and high mechanical strength to support the large Lorentz force present in the energized coil. These properties do not generally co-exist in the same material, and it is the primary interest of

this work to investigate methods of obtaining this novel combination of physical properties and to relate the properties to the design and performance of the magnet.

There are essentially two types of solution to this design problem. It is possible to satisfy the constraints on the windings with two different materials, creating what will be referred to as a supported coil. A soft copper coil wrapped in fibreglass is an example of this type of solution. The second solution is to find or develop a class of materials that have both sufficient strength and conductivity to design a monolithic coil. In recent years, a class of materials alternately known as heavily deformed in-situ composites (HDISC), or in-situ formed multifilamentary composites, but broadly named fine-scale, two-phase materials have been found to exhibit these properties to varying degrees.

Heavily deformed, two-phase wires have been shown to have strengths well in excess of any rule-of-mixtures prediction from the constituent materials and have, in fact, exhibited strengths approaching the theoretical maximum. It is not yet understood, however, what mechanism(s) are responsible for the evolution of these high strengths. It is almost certain that one mechanism is not dominant over the entire range of processing strain. A variety of processing techniques have also been reported including a range of casting techniques, and deformation with and without intermediate annealing steps. Little, however, has been said with regard to optimizing the processing methods to most efficiently obtain the final product.

With these points in mind, it is the goal of this thesis to meet the following objectives:

1. To first identify a means of choosing the best materials for high-field, pulsed magnet design.

2. To identify the mechanism(s) responsible for the evolution of the mechanical and electrical properties of these high-strength, high-conductivity, two-phase materials.
3. To investigate the stability of these materials related to changes in temperature and to processing related deformation.
4. To relate the results of the above to processing variables to optimize the processing route and efficiently produce the desired final product.

Following this introduction, Chapter 2 will present a literature review of materials selection procedures, pulsed magnet design, and what is currently known about high-strength, high-conductivity two-phase materials. Chapter 3 will describe the various experimental procedures employed in doing this work. The results of the experiments are presented in Chapter 4, followed by a discussion of these results in Chapter 5. Chapter 6 presents the development of materials selection and processing procedures and finally, Chapter 7 presents the conclusions of this thesis and makes suggestions for future work in this area.

2. Literature Review

It is not the intent of this chapter to be an exhaustive review of all of the literature related to magnet design and high-strength materials but to provide sufficient background on the topics directly related to this thesis. Although the primary focus of this thesis is the investigation of high-strength, high-conductivity materials, the design requirements of high-field, pulsed magnets provides the framework in which these properties are considered. For this reason, the salient features of pulsed magnet design will be discussed first in order to gain an understanding of the strength and electrical conductivity required of the construction materials. Having established the need for high strength and high conductivity in the winding materials, a review of the physical mechanisms which govern these properties is presented. The final section of this chapter reviews an approach to materials selection which enables the designer to express the performance of the final design in terms of the available materials property combinations.

2.1 High-Field, Pulsed Magnet Design

Whereas the field strength of an iron-cored, electromagnet (on a scrap-yard crane, for instance) is limited to the saturation field in iron of 1 - 1.5 Tesla, the quest to generate the highest possible magnetic fields in electromagnets is limited by the physical properties of the coil windings. This section will begin with a discussion of the simplest case of a current loop to develop the basic relationships describing field strength, power consumption, etc. and progress to the more complex case of compound coils and pulsed magnetic fields.

At this point, it is important to reemphasize that this thesis is concerned with pulsed magnets only to the extent that their fabrication requires high-strength, high-conductivity materials. As such, many of the details of their construction and exact solutions to field strength and stress distribution equations are omitted in favour of simpler expressions which still capture the essence of the coil's operation. Much of the material presented here can be found in any one of a number of texts on the subject. Unless otherwise noted, the primary reference for this work has been "Solenoid Magnet Design" by D. B. Montgomery (1969).

2.1.1 The Current Loop

The simplest form of solenoid magnet is a single loop of wire carrying a current as shown in Figure 2-1. There are essentially four aspects of its operation of concern here:

- i. An electrical current has an associated magnetic field.
- ii. There is an interaction force (Lorentz force) between a moving charge and a magnetic field.
- iii. Power is required to move a charge and is lost as heat.
- iv. The temperature of a conductor will increase according to the balance of the energy stored and lost to the surroundings, and its specific heat.

The field generated at the centre of the loop in Figure 2-1 (at $z=0$) is given by:

$$H_0 = \mu_0 \frac{I}{2a} \quad (2.1)$$

where μ_0 is the permeability of free space and equals $4\pi \times 10^{-7}$ [Wb / A m], I is the current in Amperes and a is the radius of the loop in metres. The field strength, H , is measured in

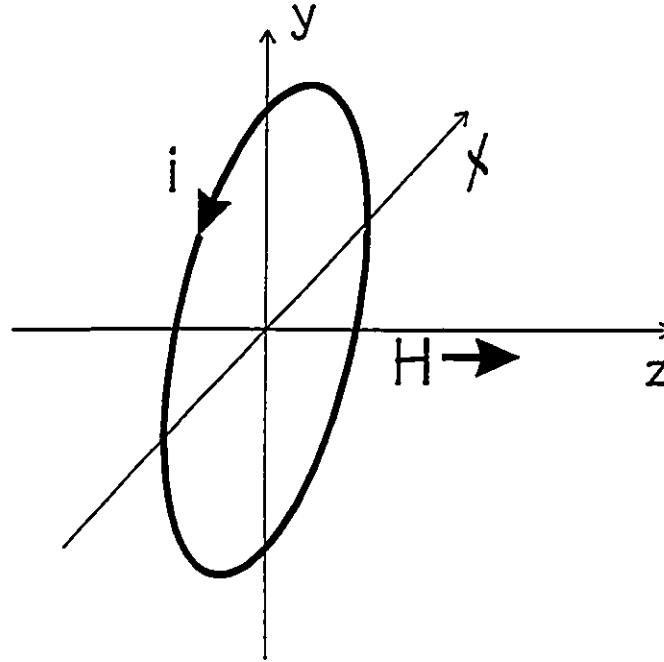


Figure 2-1 The current loop.

Tesla ($1\text{T} = 1 \text{ kg./A s}^2$). If, as an initial simplification, it is assumed that this field is constant everywhere around the loop (i.e. generated by something other than the loop itself) there would be an outward force everywhere on the loop equal to:

$$F = HI(2\pi a) \quad (2.2)$$

In a manner analogous to the hoop stress in a pressure vessel, this force corresponds to a tensile stress in the conductor:

$$\sigma_t = \frac{HIa}{A_c} \quad (2.3)$$

where A_c is the cross-sectional area of the conductor.

The power required to generate the magnetic field is simply that required to overcome the resistance of the conductor. In its simplest form, this relationship is:

$$P = I^2 R \quad \text{or} \quad P = j^2 \rho V \quad (2.4)$$

where j is the current density, ρ is the resistivity and V is the volume of the conductor. This energy is converted to heat which may be stored in the conductor and/or lost to the surroundings. If the energy was all stored in the conductor, the increase in temperature of the conductor would be described by the energy balance:

$$j^2 \rho V t = m c_p \Delta T \quad (2.5)$$

$$\frac{\Delta T}{t} = \frac{j^2 \rho}{c_p d}$$

where ΔT is the temperature increase, t is the time, c_p is the specific heat and d is the density of the conductor.

To this point, although a number of assumptions have been made, the basic physics of solenoid magnet design have been addressed and the following points have arisen. The field strength is proportional the current; the stress, power and temperature rise are proportional to the square of the field.

2.1.2 The Simple Solenoid

The geometry of a simple solenoid is illustrated in Figure 2-2. The relationships for this geometry may be derived by taking volume integrals of the relationships for the current loop and are described by Montgomery. The derivations, therefore, will not be repeated here, but the pertinent equations and any inherent assumptions will be discussed.

It is convenient, at this point, to introduce the geometric terms, α and β , described in Figure 2-2, as well as a filling factor, λ , equal to the ratio of the cross-sectional area of active conductor to the cross-sectional area of the coil. It is also convenient to use current

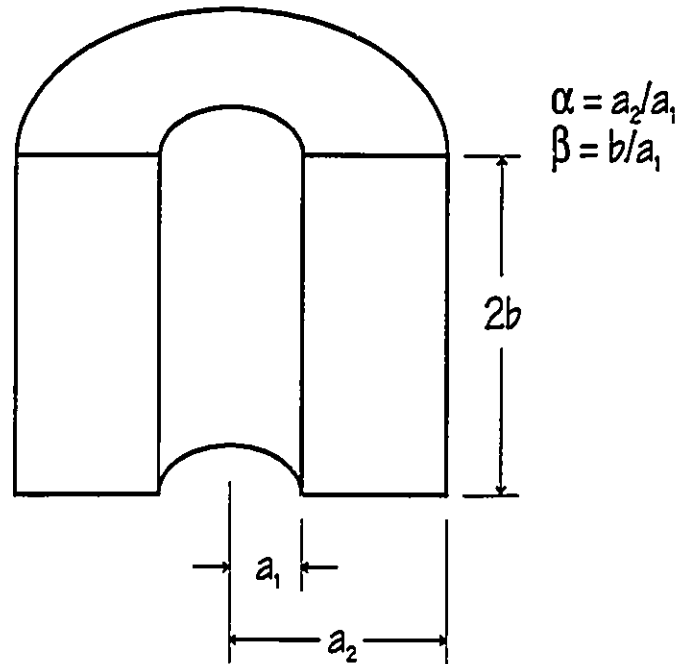


Figure 2-2 The geometry of a simple solenoid.

density and resistivity, rather than absolute current and resistance to describe the operation of the coil. This will be done for the remainder of the thesis.

The central field of a uniform current density solenoid is described exactly by the equation:

$$H_0 = \mu_0 j \lambda a_1 \beta \ln \left[\frac{\alpha + (\alpha^2 + \beta^2)^{1/2}}{1 + (1 + \beta^2)^{1/2}} \right] \quad (2.6)$$

By defining a field factor:

$$F(\alpha, \beta) = \mu_0 \beta \ln \left[\frac{\alpha + (\alpha^2 + \beta^2)^{1/2}}{1 + (1 + \beta^2)^{1/2}} \right] \quad (2.7)$$

which is entirely geometry dependent, the equation for the central field may be more simply expressed as:

$$H_0 = j \lambda a_1 F(\alpha, \beta) \quad (2.8)$$

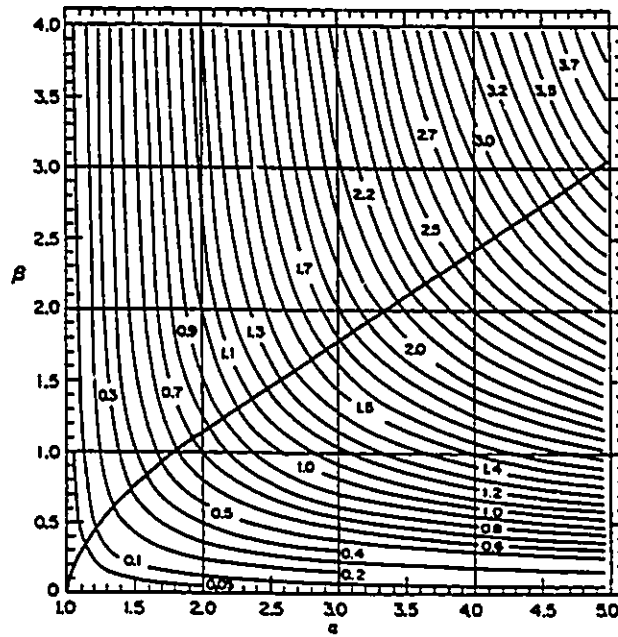


Figure 2-3 The field factor, $F(\alpha, \beta)$, plotted as a function of α and β .

The field factor can be considered as expressing the efficiency of a given geometry in converting current density into a magnetic field. Figure 2-3 plots lines of constant field factor as a function of α and β . The line which passes through the contours of constant $F(\alpha, \beta)$ connects the points of minimum coil volume for each value of field factor. In practical solenoid designs, however, it is the volume of the coil which indirectly limits the possible field. Equation 2.8 indicates that a larger field may be generated for coils with larger field factors, however, larger field factors infer greater coil volumes. Therefore, higher currents will be required to maintain the same current density and power requirements will increase.

As in the simple case of a current loop, the power required to generate a given field is given (for uniform current density) by Equation 2.4 with the addition of the filling factor, λ :

$$P = j^2 \rho \lambda V \quad (2.9)$$

By rearranging Equation 2.8 to solve for current density, the substitution into Equation 2.9 may be made, and the power expressed in terms of field strength as:

$$P = \frac{H_0^2 \rho V}{\lambda a_1^2 F^2(\alpha, \beta)} \quad (2.10)$$

As the power is still lost as heat due to the resistance of the conductor, the rate of temperature increase in a simple solenoid is unchanged from that of the current loop with the exception of the introduction of the filling factor.

$$\frac{\Delta T}{t} = \frac{j^2 \rho \lambda}{c_p d} \quad (2.11)$$

In a more complete solution, however, it may be necessary to include the effects of the insulation and incorporate them into composite values for the specific heat and density.

To make the progression from the stress in a current loop to that in a solenoid is not as straight forward as for field strength and power. For this reason, it will be discussed in slightly more detail here.

If one first considers a thin ($\alpha \approx 1$) solenoid, or current sheet, in a field produced by itself, the field is no longer constant but varies from a value close to H_0 at the inside radius to something close to zero at the outside radius if $\beta > 1$. The average field is then approximately $H/2$. From the geometry shown in Figure 2-4, the stress in the current sheet is given by:

$$\sigma = \frac{H I a_1}{2 \times 2 b t} \quad (2.12)$$

To make the next step from a current sheet to a coil is analogous to the transition from a thin-walled to a thick-walled pressure vessel with the added difficulty that the coil

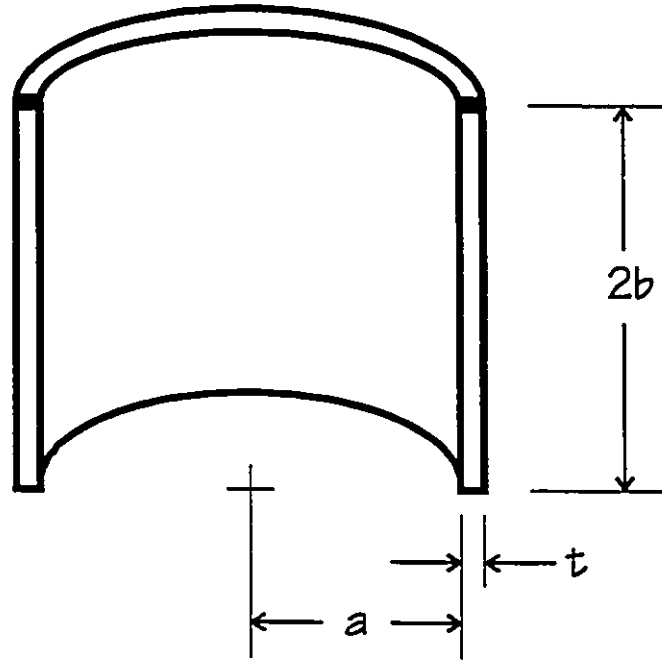


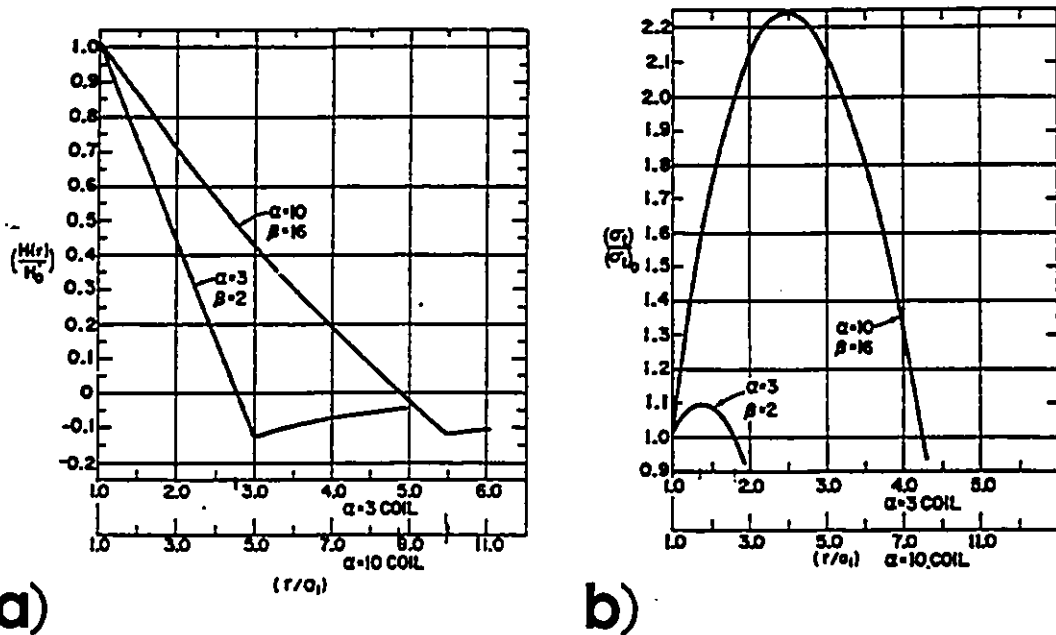
Figure 2-4 The geometry of a current sheet.

is not a continuum, but a series of windings which may or may not interact. This complicates the exact solution for stress because if, as one might expect, the maximum stress is found at the inner windings, where the field is the highest, the turns will expand to a greater degree than those farther away from the centre of the coil. If this occurs, a radial compressive stress will be set up in the windings as well as the imposed tangential stress. If the assumption is made that there is no interaction and zero initial stress, then the tangential stress on a turn at radius r at the midplane of the coil ($z=0$) is given by an equation similar to Equation 2.12:

$$\sigma_t(r) = \frac{H I r}{2 b t} \quad (2.13)$$

where H is the local value of the field which is varying with r . Recognizing that $I/2bt = j\lambda$, and rearranging Equation 2.8, the stress in the individual winding at a radius r is:

$$\sigma_t = \frac{H H_0 r}{a_1 F(\alpha, \beta)} \quad (2.14)$$



a) **b)**
Figure 2-5 Profiles of a) field strength and b) tangential stress as a function of position in the coil.

Thus, the stress at any point in a coil is a function of r and H which is decreasing with r .

The profiles of field and tangential stress have been calculated and are shown in Figures 2-5 a) and b) (Montgomery, Figures 5.2 a and b). It is interesting to note in Figure 2-5 b) that the tangential stress is not a maximum at the inside radius, but at some point just inside the coil. This would tend to separate, rather than concentrate the windings in this region of increasing tangential stress. The assumption of no interaction between windings would appear to be valid in this region. From the point of maximum radial stress outwards, because the stress is decreasing, the outer windings actually serve to reinforce the most highly stressed windings. However, while the exact distribution of stresses may be critical in the final construction of these magnet coils, it is only important here to note that the use of Equation 2.14 is valid and only a slight over estimation of the stress in the windings. The maximum stress in the coil may be written as:

$$\sigma_{\max} = H_0 j \lambda a_1 = \frac{H_0^2}{F(\alpha, \beta)} \quad (2.15)$$

2.1.3 High-Field, Pulsed Magnets

The previous sections have discussed the basic aspects of simple solenoid magnets. In this section, the developed relationships will be applied in a simple way to help explain the evolution of what have become very complex designs. In the brief examples that follow, a single coil ($a_1=1\text{cm}$, $\alpha=3$, $\beta=2$, $\lambda=0.9$) will be used to illustrate the problems encountered in generating high magnetic fields.

Let us consider the implications of generating a 10 Tesla field. If one first considers the current density required:

$$j = \frac{H_0}{\lambda a_1 F(\alpha, \beta)} \quad (2.16)$$

$$j = 6 \times 10^8 \text{ [A/m}^2\text{]}$$

one sees that this is a very large value of current density. Using values for pure copper, for the relatively small coil described here, this would require almost 620 kW of power and would heat up at a rate of 180 K/sec. The stress in the coil would reach 55 MPa. Clearly the generation of even these modest fields is not trivial. The quest to generate fields to 100 T will require a great deal of complex engineering design.

The problems of power consumption and resistive heating may be overcome with the use of superconducting coils. However, these coils are currently limited to fields of approximately 20 T due to critical current density, field, or Lorentz forces. A second solution to the ohmic heating problem is to incorporate forced water cooling channels into the coil.

While this avoids overheating, it also reduces the filling factor, λ , thereby affecting the efficiency of the coil. This solution will have an upper limit, beyond which the cooling effect can not keep up with the loss in efficiency.

Fields up to 30 T have been generated by making use of the additivity of magnetic fields. The field at the centre of two concentric coils is the sum of the two individual fields. A water-cooled copper coil generating 10 T has been placed inside a 20 T superconducting coil to produce these fields.

Beyond 30 T, the power consumption and ohmic heating are so great that, to date, the only solution is to generate pulsed magnetic fields. In a pulsed field, the coil is only energized for a short period of time; the current density and, hence, the generated field may be greater without overheating the coil. In the typical operation of these magnets, the coil is immersed in liquid nitrogen, and the maximum current density (or field) is set by the time of the pulse and a maximum allowable increase in temperature. It should be noted here that many of the material properties used in the equations of the previous section are temperature dependent. Exact solutions to these equations for the pulsed magnet case would have to account for this dependence.

As the generated fields increase, however, another limitation arises. The stress in the coil, which at 10 T was not a factor for soft copper, increases with the square of the field. For the same coil as in the previous example, the generation of a 50 T pulsed field requires a winding strength of 1.4 GPa — over three times the ultimate strength of drawn pure copper wire.

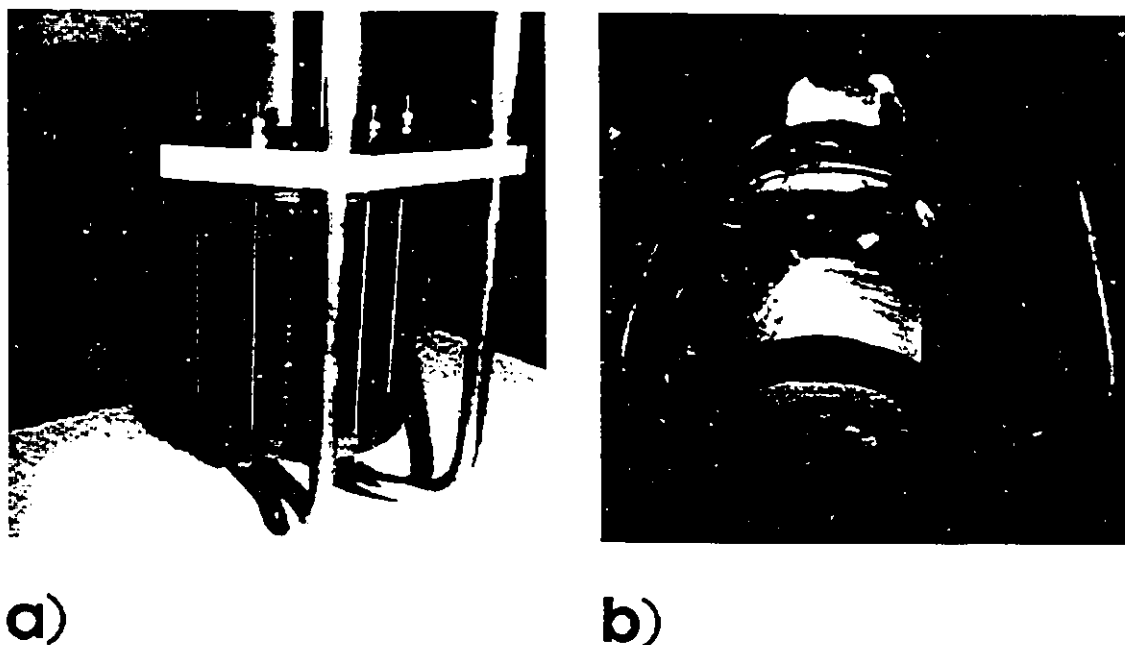


Figure 2-6 A fibreglass reinforced, copper coil designed for 50 T a) before and b) after testing to destruction at 57 T.

It becomes clear that, to generate higher magnetic fields for longer times, it is essential to design coils with both high electrical conductivity for power and temperature considerations, and high mechanical strength to resist the Lorentz force. One class of solution to this problem has been to use a highly conductive material such as annealed, pure copper and reinforce the coil with a strong, insulating material such as glass fibre reinforced epoxy. This type of coil has generated pulsed fields of 50T for 5 msec. The coil is shown in Figure 2-6 before and after testing to destruction at 57 T [NHMFL Reports, 1992]. This is a viable solution for single coil applications. However, in compound coil designs such as the one described by Sims et al. (1993), the need to reinforce a coil with a poor conductor decreases the overall filling factor of the magnet, decreasing efficiency and increasing power consumption and heating rates. This sets the materials science goal - to find materials that combine high conductivity and high mechanical strength.

2.2 High-Strength, High-Conductivity Materials

The preceding review of the materials requirements for the construction of high-field, pulsed magnets has illustrated the need for materials with combinations of high mechanical strength and high electrical conductivity. To this end, there are a number of topics to be examined in this section. In considering the strength of materials, particularly ultra-high strength materials, it is instructive to first examine the theoretical limits on strength, how these limits can be approached and why most engineering materials exhibit strengths well below these limits. With this information, it is possible to suggest ways in which engineering materials may be efficiently strengthened. An examination of the literature on some high-strength materials which are candidates for use in pulsed magnets will consider the applicability of the proposed strengthening mechanisms.

The very fine microstructural scales observed in heavily drawn, two-phase wires give rise to questions regarding the stability of these materials. To provide background for later discussion, aspects of codeformation and both dimensional and morphological stability of the drawn wires will be examined.

The final part of this section of the review will deal with the mechanisms that govern the electrical resistivity of metals. Particular attention will be paid to the effects which may arise as a result of the fine-scale structure of high-strength materials.

2.2.1 Strength of Materials

Kelly and Macmillan (1986) have described the theoretical limits on the strength of materials, and the ways in which these limits may be approached. The theoretical strength of a crystalline material may be described as the stress required to shear one lattice plane over another in a perfect lattice. Depending upon the model and the approximations made, the theoretical strength of a metal is calculated to be in the range $\mu/20$ to $\mu/30$, where μ is the shear modulus. It is convenient, for wire products, to convert these values to equivalent tensile strengths. Making the general approximation that $\mu = \frac{3E}{8}$ (where E is Young's Modulus), for a material such as copper ($\mu=47$ GPa, $E=120$ GPa) this suggests a theoretical tensile strength of the order of $\sigma \approx \frac{E}{65} \approx 2$ GPa. The fact that the yield stress of pure copper is of the order of 30 MPa is due to the existence of dislocations and that plastic deformation is accomplished by dislocation motion. To create a strong material, therefore, it is necessary to develop a microstructure that contains no dislocations or dislocation sources, or, one which has many strong obstacles to dislocation motion.

In examining methods to strengthen metals for use in high-field magnets, it is worthwhile to first look at the characteristics of some inherently strong materials. Kelly and Macmillan (1986), in their first appendix, list the properties of a number of materials that approach their theoretical strength. The list is reproduced here, in part, as Table 2-1. An examination of these materials suggests that they fall into one of essentially two categories. In the first of these are materials with high lattice friction — materials in which it is very difficult to move a dislocation. The majority of the materials in this group are either ceramics with strong ionic bonds or materials such as silicon and diamond with directional, covalent

bonds and complex crystal structures. The inherently poor electrical conductivity of these materials, however, makes them a poor choice for the application considered here.

The second category of materials found in Table 2-1 are those that exist on a very fine scale. A fine scaled microstructure implies either very closely spaced obstacles to dislocation motion, as in the case of heavily drawn, pearlitic wire (patented wire Table 2-1), or materials in whisker form (diameters typically less than $10\text{ }\mu\text{m}$) which exhibit exceptional strength due to their surface and internal crystallographic perfection. As the whiskers increase in size, the chance of them containing dislocations also increases. The stress to

Table 2-1 Strength data for some selected, high-strength materials.

Material	Form	Tensile Strength [GPa]	Young's Modulus [GPa]	σ/E
Patented Steel	wire ($100\mu\text{m}$)	4.2	220	1/50
W	wire ($25\mu\text{m}$)	3.9	405	1/100
Mo	wire ($150\mu\text{m}$)	2.1	343	1/165
Be	wire ($150\mu\text{m}$)	1.3	315	1/250
Al_2O_3	whisker	22.3	420	1/18
$\alpha\text{-Fe}$	whisker	12.6	196	1/15
Si	whisker	7.6	163	1/21
Si	large crystal	4.1	163	1/40
B_4C	whisker	21	483	1/23

move a dislocation is significantly lower than that required to homogeneously nucleate one in most materials. Therefore, once dislocations are present in the lattice, the stress required for slip is drastically reduced.

To obtain a strong material, therefore, it is necessary to prevent slip in one of two ways — by forcing the homogeneous nucleation of new dislocations, or by restricting the motion of existing dislocations. Although there are a number of ways to envisage both scenarios, there are considerably more methods available for hindering the motion of dislocations. These will be considered next.

2.2.2 Effects of Dislocation Density

In moving a dislocation through a crystal, work is done on the crystal as the local strain field of the dislocation passes through the otherwise undistorted lattice. Any type of obstacle that increases the amount of work required for a dislocation to move a given distance will hinder the motion of the dislocation. This additional work is done either by shearing the obstacle and creating new surface, or by increasing the line length of the dislocation as it bends around the obstacle.

The most common way of strengthening pure, single-phase materials is through the accumulation of dislocation density by strain hardening. Experimental evidence over a wide range of strains has shown that the increase in flow stress due to dislocation density is described by an equation of the form:

$$\Delta\sigma = \alpha\mu b\sqrt{n} \quad (2.17)$$

where b is the Burger's vector, n is the dislocation density and $\alpha=0.2$ for fcc metals and 0.4 for bcc metals.

To check the ability to reach the theoretical strength of a material by dislocation storage alone, it is useful to further examine Equation 2.17. Assuming an fcc material with a Burgers vector of 2\AA , to reach $\mu/25$ would require:

$$n = (25ab)^{-2}$$

$$n \approx 10^{18} \text{ m}^{-2}$$

A dislocation density of this magnitude would require a mean spacing of roughly 1 nm. Because dislocations are subject to recovery and annihilation precesses, dislocation densities of this magnitude are not generally observed. Thus, it appears unlikely that a material will reach its theoretical strength by dislocation storage unless annihilation mechanisms are inhibited. The potential for this has been demonstrated in some ordered materials. (Gray and Embury, 1993)

The majority of engineering materials are polycrystalline and it is, therefore, appropriate to examine the influence of grain size on the flow stress of a metal. Hall (1951) and Petch (1953) first proposed the well known empirical relationship relating the flow stress to the internal, microstructural scale:

$$\sigma_y = \sigma_0 + kd^{-1/2} \quad (2.18)$$

where σ_0 is the stress required to move a dislocation in a single crystal, k is a measure of the strength of the barrier (grain boundary or second phase) and d is the characteristic length (grain diameter or interphase spacing). As mentioned above, the introduction of a second phase will act as a barrier for dislocation motion. To reach the theoretical tensile strength by grain refinement would require a grain size in copper ($\sigma_0 = 25 \text{ MPa}$, $k = 0.11 \text{ MPa}\cdot\text{m}^{1/2}$, $\sigma_{th} = 2 \text{ GPa}$) of:

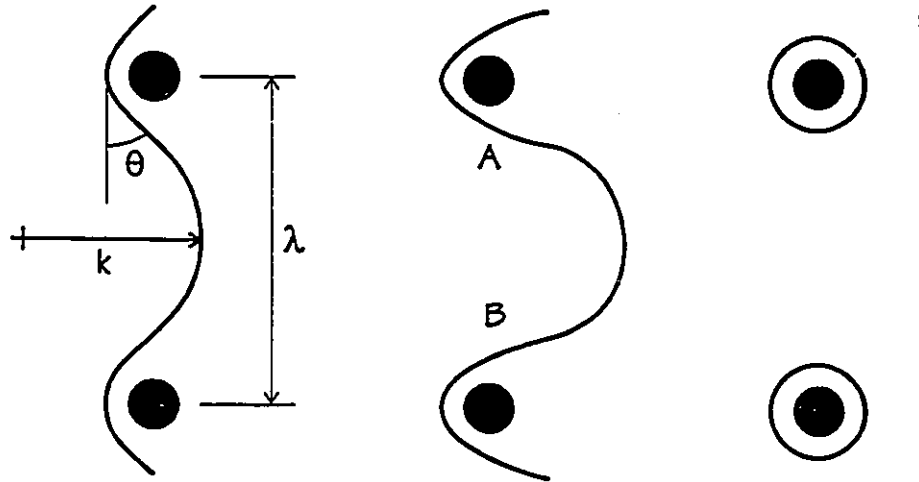


Figure 2-7 Dislocation bowing by the Orowan mechanism.

$$d = \left(\frac{k}{\sigma_{th} - \sigma_0} \right)^2 \quad (2.19)$$

$$d \approx 3 \text{ nm}$$

Grain sizes of this magnitude are typically not obtained by cold working processes, however, vapour deposition techniques are capable of making materials on this scale. Kelly and Macmillan (1986) point out that the increase in stored energy in very fine grained metals is very small (of the order of 10^4 kJ/m^3) and thus it should be possible to make very strong materials by grain size refinement.

The introduction of a second phase to the microstructure is another method of achieving high strength materials. As a detailed example of the influence of second phase particles, let us consider the case of the introduction of hard second-phase particles to the material. Apart from “restraining” a dislocation (as a grain boundary might), a second phase that is in particle or rod form can store dislocations in another manner. When a

dislocation meets an array of hard, second phase particles, it is forced to bow between them as in Figure 2-7 (see e.g. Brown and Ham, 1971). This causes an increase in the flow stress because energy is required to create additional line length. At a critical stress, the dislocation will leave a loop around the particle and continue on. This stress, the Orowan stress, is given by:

$$\tau = \frac{\mu b}{L} \quad (2.20)$$

where L is the interparticle spacing. This predicts that the material would not approach the theoretical stress until the interparticle spacing was of the order of 50 nm. As will be shown later in this review, interphase spacings of this magnitude are attained in some heavily deformed materials.

There are, however, potential complications to the process when the particles are very closely spaced. If the passing dislocation line leaves a loop around the particle, there will be an elastic back stress generated which will make it more difficult for subsequent dislocations to pass — increasing the effective size of the particle and decreasing the space between neighbouring particles. If the particles are very close together, as the dislocation bows between the particles, there will be an interaction between the two segments marked A and B in Figure 2-7. These two segments have the same Burger's vector and opposite sense and their attraction will alter the line tension.

To this point, we have considered how dislocation density affects the flow stress of a material and how dislocations may be inhibited from moving. It is necessary, now, to consider mechanisms for the generation and accumulation of dislocations.

2.2.3 Dislocation Generation and Accumulation

The deformation of two-phase materials is a complex process. Maintaining compatibility requires that at least one of the following occur:

1. That the two-phases co-deform, meaning that the average shape change of individual grains is equal to the macroscopic shape change.
2. The second phase deforms elastically, resulting in residual stresses and increased plastic deformation of the matrix phase.
3. The second phase fractures and the matrix is forced to flow around the fractured particles.

To understand the mechanisms involved in the deformation of two-phase materials, it is of prime importance to follow the evolution of the shape of the second phase.

If one considers an array of like edge dislocations in a perfect lattice as shown in Figure 2-8 a), it can be seen that a net curvature of the lattice results. The radius of curvature is given by $1/nb$, where n is the density of dislocations and b is the Burger's vector (Ashby, 1971).

If we were to now consider a crystal with a random array of both positive and negative dislocations as shown in Figure 2-8 b), the contribution of these dislocations could be separated into two categories. If we take as positive all those dislocations with the same sense as in Figure 2-8 a), then these dislocations alone would tend to decrease the radius of curvature of the lattice and negative dislocations would tend to increase the radius. The total

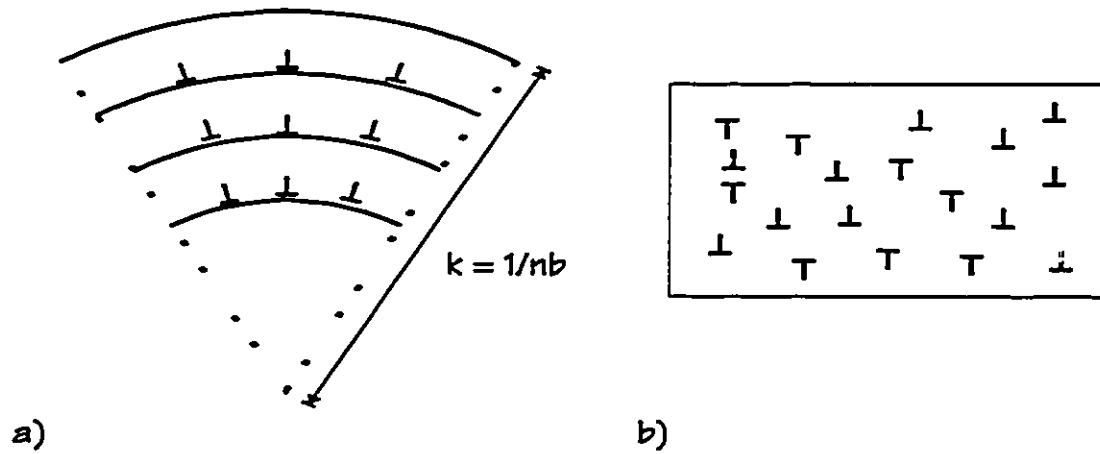


Figure 2-8 a) The curvature arising from an array of like edge dislocations. b) A random array of edge dislocations.

number of dislocations that “cancel-out” each other are known as *statistically stored* dislocations because they do not serve to alter the overall shape of the crystal. The net remaining dislocations are known as *geometrically necessary* dislocations because they exist due to the imposed geometry (i.e. the applied strain) on the crystal (Ashby, 1971). The total dislocation density is then the sum of the two components:

$$n_T = n_G + n_S \quad (2.21)$$

Following the development in Ashby (1971), the density of geometrically necessary dislocations may be predicted by the equation:

$$n_G = \left(\frac{1}{\lambda_G} \right) \frac{4\gamma}{b} \quad (2.22)$$

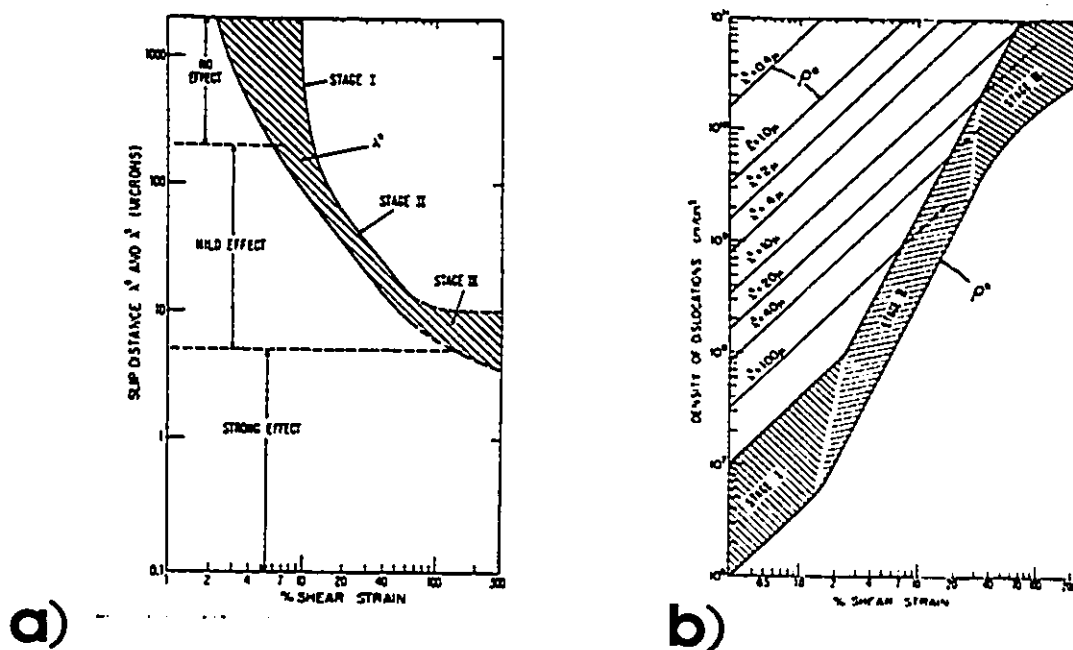


Figure 2-9 a) Characteristic slip distances and b) dislocation density as a function of shear strain from Ashby (1971)

where γ is the shear strain and λ_G , the geometric slip distance, is the barrier spacing for plate-like particles and grain boundaries. In the case of spherical particles, $\lambda_G = r/f$ where r is the radius of the particles and f is the volume fraction.

Figures 2-9 a) and b) from Ashby (1971) illustrate the relative effects of statistical and geometrical dislocations on the total dislocation density. The statistical slip distance, λ_s , varies with strain as shown by the shaded region in a). Over the range of strains shown, the geometric slip distance, λ_G , is essentially constant and would be a horizontal line on the graph. In Figure 2-9 b), the relative contributions of geometrical and statistical dislocations are shown. If one accepts that the greatest contribution to the total density will dominate the work hardening behaviour of the crystal, then Figure 2-9 b) shows that geometrically necessary dislocation generation will dominate overall dislocation density when initial

barrier spacings are below about 4 μm . The implication of this becomes evident when recalling Equation 2.17:

$$\Delta\sigma = \alpha\mu b\sqrt{n}$$

If one can influence the evolution of dislocation density via the barrier spacing, then control of the evolution of strength should be possible.

The development of Ashby is, for two-phase materials, an extreme in that the second phase is assumed to be non-deformable. In the case of copper-niobium and copper-silver and, in fact, Fe-Fe₃C wires, the second phase does deform to a certain extent. This co-deformation of the two phases will serve to decrease the generation of geometrically necessary dislocations.

2.2.4 Internal Energy Storage

To this point, consideration of the work done in deforming a metal has primarily been the work of overcoming obstacles. This energy is almost entirely lost in the form of heat, however, a fraction of the work done (estimates suggest roughly 5–10%) is stored in the material. There are a number of ways to store energy in a metal (for an excellent review, see Bever, Holt and Titchener, 1973) of which three are of primary importance here. The first mechanism of energy storage has already been dealt with to some extent. That is the energy associated with accumulated dislocations. The energy per unit length of a dislocation line is given by:

$$W_{\text{dist}} = \frac{\mu b^2}{2} \quad (2.23)$$

and thus, at modest dislocation densities (eg. 10^{16} m^{-2}) for a cold worked material such as copper ($\mu=47 \text{ GPa}$, $b=1.3 \text{ \AA}$), the dislocation density contributes stored energy of the order of:

$$W_{\text{disl}} = 4 \times 10^4 \text{ kJ/m}^3$$

The combination of Equations 2.17 and 2.23 also leads to the general result that the stored energy in a material is roughly proportional to the square of the flow stress.

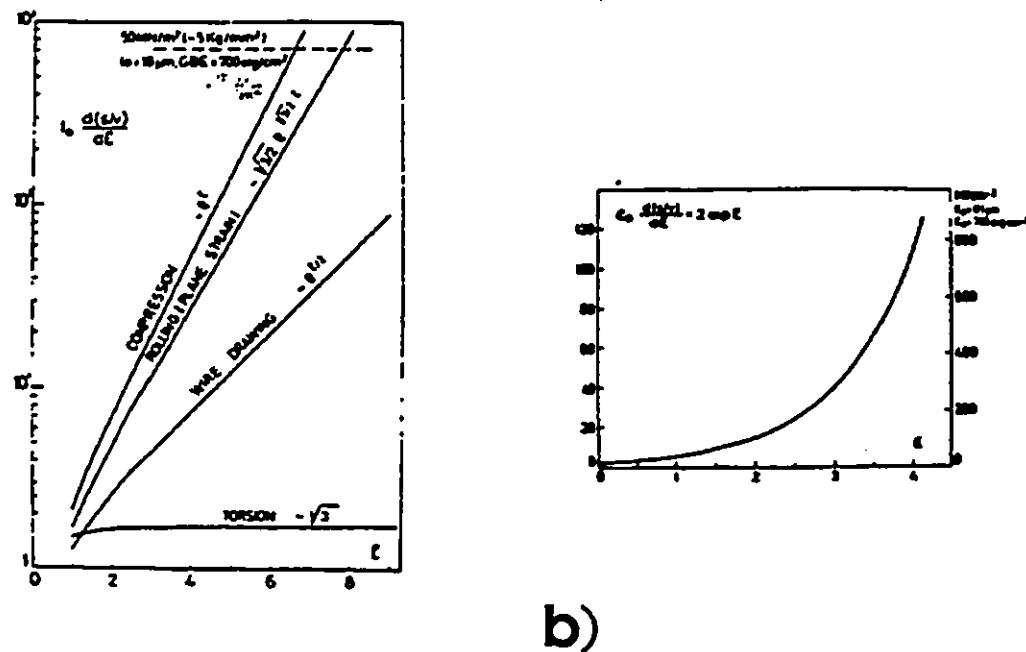
A second source of stored energy is the result of residual elastic stresses. Elastic stresses are stored in two-phase materials in which the two phases differ in strength and stiffness. The magnitude of the stored energy is dependent upon the volume fraction of the phases and their elastic properties. The elastic stored energy in a material just before yield (or fracture in a brittle material) is given by the area under the stress-strain curve and is simply:

$$W_{\text{el}} = \frac{\sigma_f^2}{2E} \quad (2.24)$$

If, for comparison, one considers a copper whisker ($\sigma_f = E/65$), then the stored energy is of the order:

$$\begin{aligned} W &= \frac{(E/65)^2}{2E} \\ W &= \frac{E}{8450} \\ W &\approx 1.5 \times 10^4 \text{ kJ/m}^3 \end{aligned}$$

and is comparable to the energy previously calculated for dislocation storage. In a two-phase material, this energy could be stored in the second phase.



a) The increase in surface area to volume ratio for an initially cubic grain subject to various modes of deformation. **b)** The predicted increase in flow stress due to the increased stored energy.

The third mechanism for energy storage to be considered here is due to the creation of internal surface. Originally proposed by Nutting (1974) as the driving force for dynamic recrystallization and considered in the review by Gil Sevillano et al. (1981) for two-phase materials, this approach estimates the contribution to the flow stress (or energy required for deformation) due to the creation of internal surface. As shown in Figure 2-10 a), for an initially cubic grain, the ratio of grain boundary surface to volume increases exponentially with strain in a manner dependent upon the geometry of deformation (i.e. rolling, wire drawing, etc.). For each increment of strain, the flow stress must increase by an amount at least as great as the surface energy times the increase in surface area. Calculations in Gil Sevillano et al. (1981) demonstrate that, for common grain sizes and manufacturing strains, these effects are minimal. However, due to the exponential dependence on strain, for processes such as wire drawing in which very large strains may be imparted, the predicted

increase in flow stress can easily reach large fractions of 1 GPa (see Figure 2-10 b)). The greatest difficulty in quantifying this stored energy is in determining the appropriate value of the surface energy. For an interface that is under traction, the surface energy will be different than that of interface under equilibrium conditions (see Greer, 1992).

2.2.5 Macroscopic Strengthening

There exists one other possibility for strengthening a soft material. While mechanisms discussed to this point have been concerned with the pinning and storage of dislocations, the concept of fibre strengthening treats the constituent materials as continua and is based on the transference of load from the matrix material to a reinforcing phase. There are numerous methods of manufacturing these materials and numerous models of varying complexity for predicting the composite properties (cf. Chawla, 1987). It is sufficient here, however, to deal with the simplest of these models and its assumptions. The rule-of-mixtures approach to modelling composite behaviour should be valid for many of the high-strength materials to be discussed in the next section in light of the structure of these materials and the assumptions of the model. The rule-of-mixtures for composite strength and stiffness are given below:

$$E_c = E_f V_f + E_m (1 - V_f) \quad (2.25)$$

$$\sigma_c = \sigma_f V_f + \sigma_m (1 - V_f) \quad (2.26)$$

where the subscripts c , f , and m refer to the composite, reinforcing fibre, and matrix materials.

Inherent in the use of these equations are the following assumptions:

1. The reinforcing phase is long with respect to its diameter and aligned in the direction of the applied load.

2. The strain in each phase is equal.
3. There exists a strong bond between the matrix and the reinforcing phase.

As will become apparent in the following section, these criteria appear to be satisfied. The question that remains, for the case of the composite strength, is what values are appropriate for the strength of the constituent materials?

Having considered the basic strengthening mechanisms available to two-phase materials, it is appropriate to further consider how they apply to some engineering materials. As a model system, Fe-Fe₃C wires will be considered first, followed by a discussion of the work on copper-niobium and copper-silver wires.

2.2.6 Fe-Fe₃C Wires

Of all the materials commercially available in wire form, one of the strongest is patented and drawn wire (music wire) (Kelly and Macmillan, 1986). This wire is made from steel of eutectoid composition, transformed at 500°C, and subsequently cold drawn. The resultant microstructure is a fine-scale mixture of cementite (Fe₃C) lamella in a ferrite matrix. After drawing, the lamella are aligned with the wire axis and the Fe₃C is both plastically deformed and fragmented (e.g. Langford, 1977). The study by Embury and Fisher (1966) on drawn pearlite proposed that the strength of the wires was dependent upon the spacing of the substructural barriers (both cementite lamella and dislocation cell walls) by a Hall-Petch relationship. The observation that the interlamellar spacing decreased in proportion to the wire diameter leads to the expression:

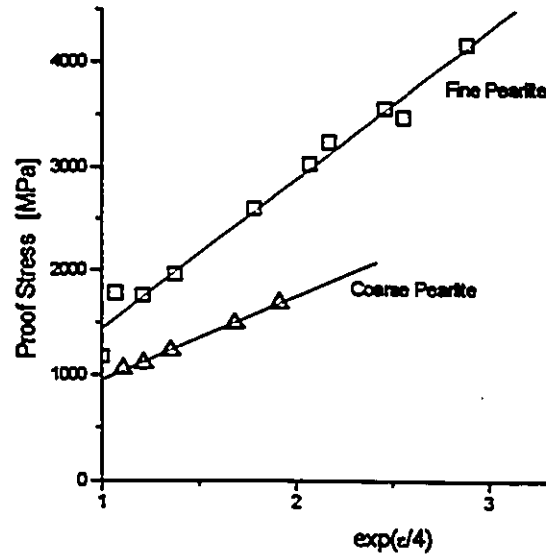


Figure 2-11 The effect of initial microstructural scale on the evolution of flow stress in drawn pearlite (Embury and Fisher, 1966).

$$\sigma_f = \sigma_i + \frac{k}{d_0^{1/2}} \exp(\epsilon/4) \quad (2.27)$$

where σ_i is the apparent friction stress of the matrix, k is the Hall-Petch slope, d_0 is the initial barrier spacing and ϵ is the true strain. The data from this investigation is shown in Figure 2-11. The fine pearlite began with an interlamellar spacing of approximately 70 nm, while the coarse pearlite had an initial interlamellar spacing of 200 nm. This data illustrates very well the advantages in terms of strength that are gained from starting with a very fine-scaled initial structure.

The model is simplistic in that it gives a simple scaling law for two-phase structures and ignores the complex issues of the co-deformation of two-phase materials (see eg. Langford, 1977). The model also ignores the effects of elastic stresses in the cementite.

2.2.7 Copper-Niobium Wires

The original work on heavily drawn copper-niobium wires were a result of their use as a precursor to Cu-Nb₃Sn superconducting wires. (See e.g. Harbison and Bevk, 1977.) With further investigation (Bevk, Harbison and Bell, 1978) strengths in excess of 2 GPa were obtained in the finest wires. The fact that these values are well in excess of a rule-of-mixtures prediction using the bulk properties of copper and niobium, led Bevk et al. to the simple model that the strength of these materials is simply a rule-of-mixtures based on the theoretical strength of the constituent materials.

The as-cast copper niobium consists of niobium dendrites ranging in size from 1 to 10 μm (Bevk et al., 1978; Verhoeven et al., 1989a). As-cast rods are subsequently swaged and drawn to their final diameters. Owing to the development of the $\langle 110 \rangle$ texture in the niobium on drawing, the niobium filaments adopt a ribbon-shaped cross section and are forced to take on complex shapes to maintain continuity with the surrounding matrix. (See Hosford, 1964.)

Figures 2-12 a) and b) are from Bevk and Karasek (1979) and Spitzig and Krotz (1987) respectively. Figure 2-12 a) shows the increased tensile strength as a function of both niobium volume fraction and imposed wire drawing strain. Figure 2-12 b) demonstrates the effect of alloying the copper with niobium and the effect of the initial scale of the structure. The open and solid triangles are values for drawn copper and niobium with the dashed line representing the rule-of-mixtures prediction for a Cu-20%Nb composite. The open squares and circles are the experimental results for the Cu-20%Nb composite. These curves show no sign of the saturation of flow stress apparent in the pure materials.

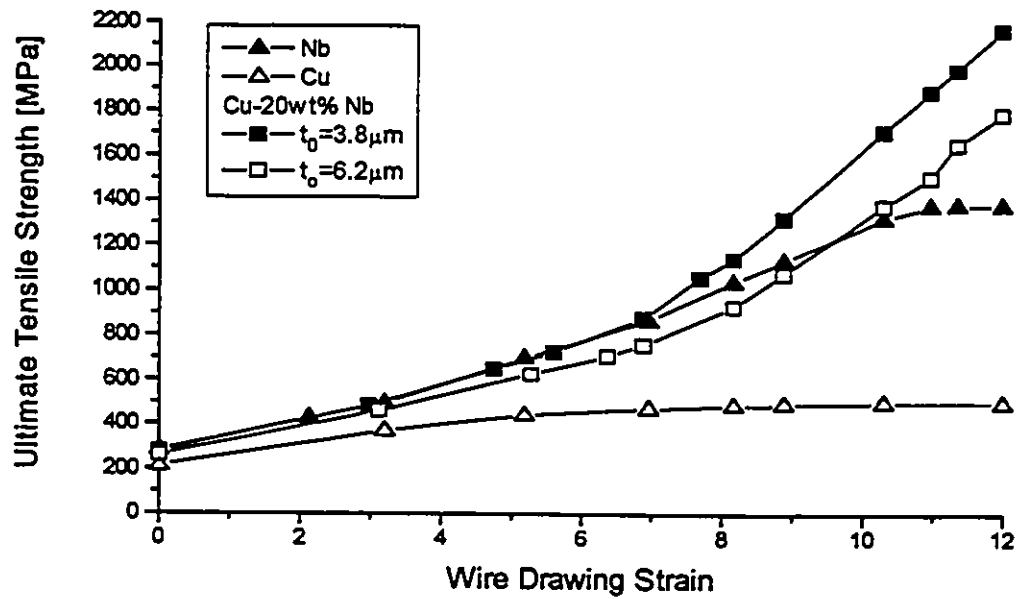
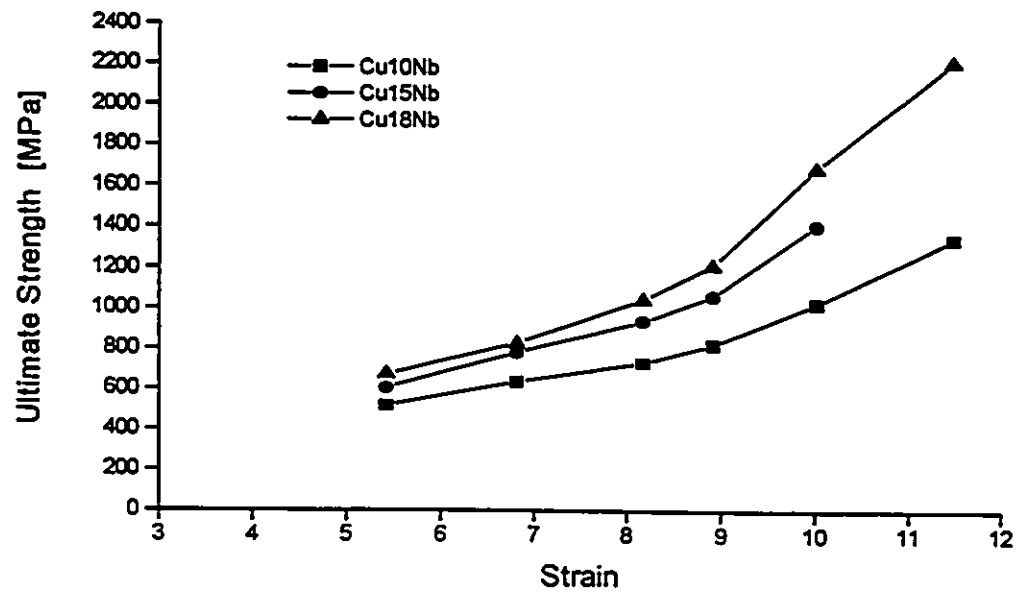


Figure 2-12 a) The influence of niobium volume fraction and imposed strain on the tensile strength of drawn Cu-Nb wires. b) The effect of initial scale on the evolution of tensile strength.

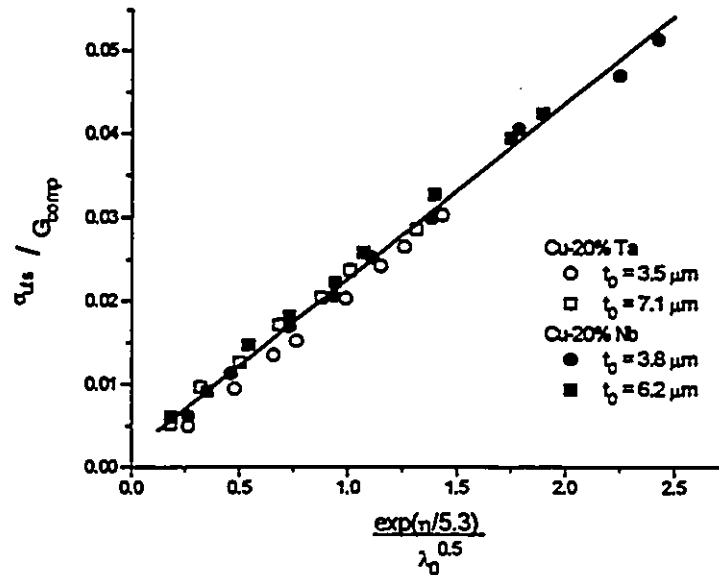


Figure 2-13 Normalized strength versus normalized filament spacing for Cu-Nb and Cu-Ta wires. (See Spitzig and Krotz, 1988)

The curves of Figure 2-12 b) also illustrate the effect of decreasing the initial scale of the composite. The wire with the smaller initial dendrite arm spacing has a significantly higher flow stress at similar wire drawing strains (400 MPa at $\epsilon=12$). Figure 2-13 from Spitzig and Krotz (1988) shows the data for both Cu-Nb and Cu-Ta composites in which the UTS (normalized by the shear modulus of the composite) is plotted against a normalized filament spacing to give a reasonable correlation. This correlation suggests that the flow stress of the composite is dependent more so upon the filament spacing than the actual wire drawing strain.

There are essentially two models prevalent in the literature for the strengthening of heavily deformed copper-niobium wires — over which an extensive debate has been published (Funkenbusch and Courtney, 1989; Spitzig et al., 1990; et seq.) Funkenbusch and Courtney propose a model based on substructural hardening due to the storage of disloca-

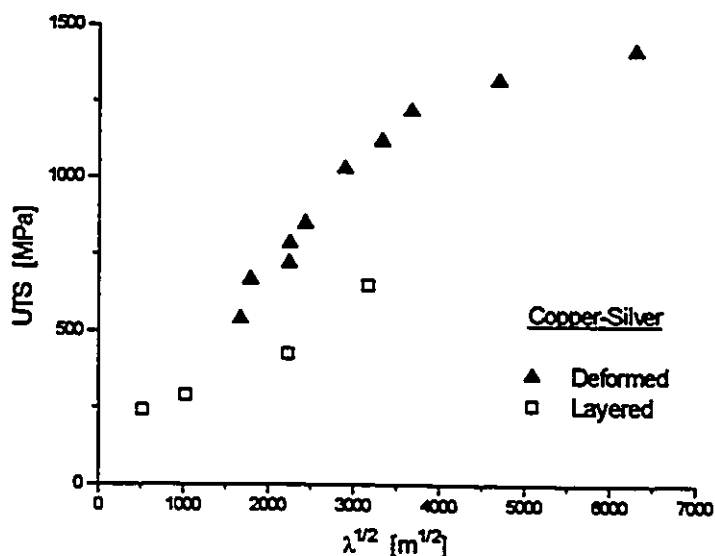


Figure 2-14 Strength versus interphase spacing for materials made by vapour deposition and by deformation processing.

tions, while Spitzig et al. suggest a barrier strengthening model (as do Bevk and co-workers, eg. 1978).

An extensive review by Everett (1988) on similar systems, attempted to provide some insight into the barrier strengthening model. Comparisons were made of wire drawn and vapour-deposited films of Ag-Cu, Cu-Cr, and Cu-Fe composites. Figure 2-14 shows the data compiled by Everett for strength versus interphase spacing in copper-silver materials. The fact that the vapour-deposited, layered composites exceed a rule-of-mixtures prediction of strength indicates that the interphase spacing is important in determining the mechanical properties of the materials. However, the effects of deformation in reaching these spacings must also play a role in the strengthening of the composite as the deformation processed composites were consistently stronger than deposited materials of the same scale. The most obvious difference in the two materials, while not reported by Everett, must be

the morphology of the second phase. While the deformation processed materials have been shown to consist of a heavily deformed matrix containing what are essentially whiskers of the second phase, the deposited materials will consist of polycrystalline layers of each phase.

2.2.8 Copper-Silver Wires

Heavily deformed copper-silver alloys were first successfully developed for high-strength, high-conductivity alloys in the late 1940's as a potential replacement for copper-clad steel (Hodge et al., 1949, 1951). The subsequent investigation of Frommeyer and Wassermann (1975a, b) on the copper-silver eutectic (60at%Ag) examined the mechanical and electrical properties of these wires. The initial microstructure is that of a rod eutectic with an initial scale of 1-3 μ m. As in the case of the CuNb wires, the rods were then drawn to final reductions up to 99.99%. However, in contrast to the Cu-Nb case, the Cu-Ag system is an fcc-fcc combination. The drawn silver filaments, therefore, do not display the complex, ribbon-shape of the niobium filaments, but remain essentially round in cross-section.

Figure 2-15 a) shows the experimental results of Frommeyer and Wassermann for drawn copper, silver, and the copper-silver eutectic. The flow stress of the eutectic reaches a value of 1.4 GPa after the highest drawing strains. The interesting observations of their work involves the combined measurements of dislocation density, internal friction, and elastic moduli as a function of mean fibre diameter. Figure 2-15 b) shows their graph of internal friction and elastic moduli versus the mean fibre diameter. The elastic moduli and internal friction were measured by the resonant frequency method. The maxima and minima in these curves correspond to the parallel electron microscopy observations of maximum dislocation density at an interphase spacing of roughly 500 - 600 Å. Specimens reduced

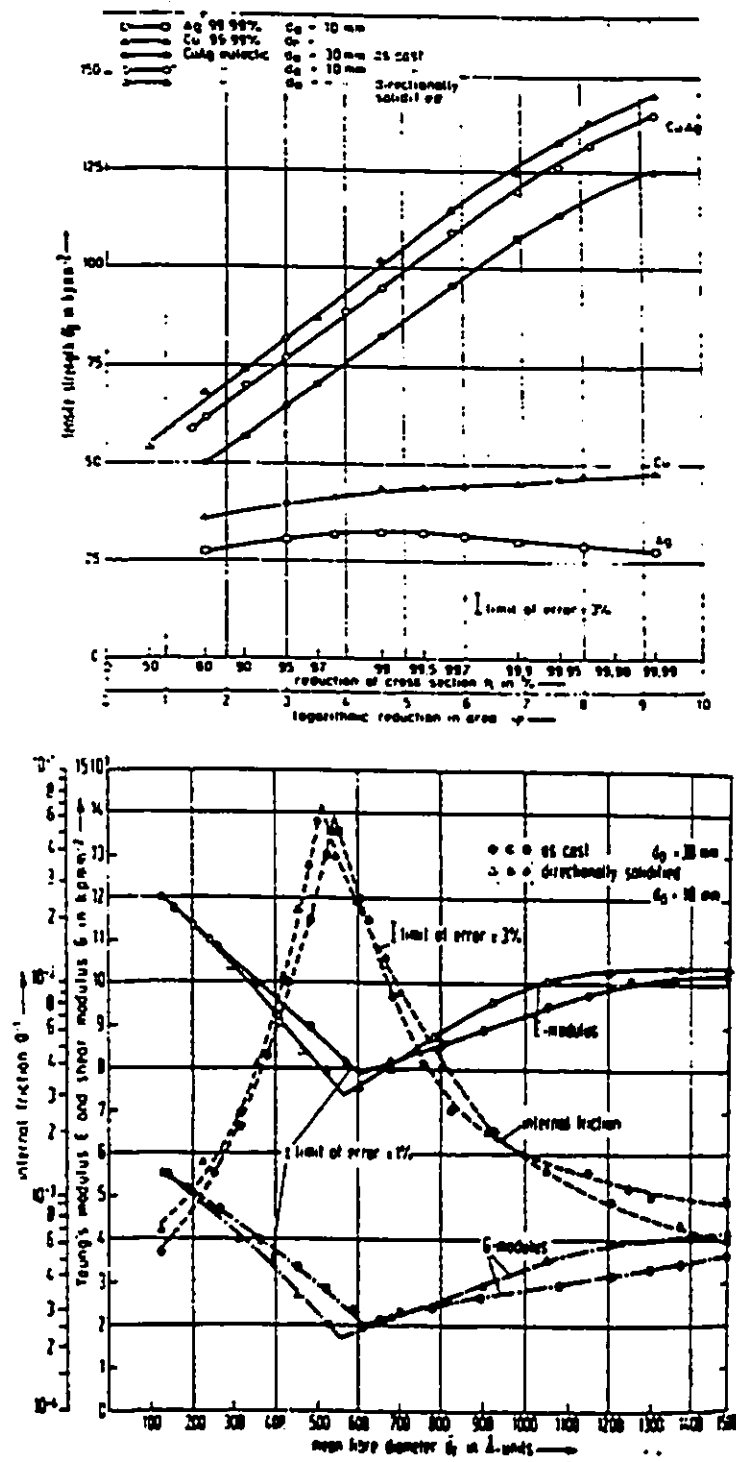
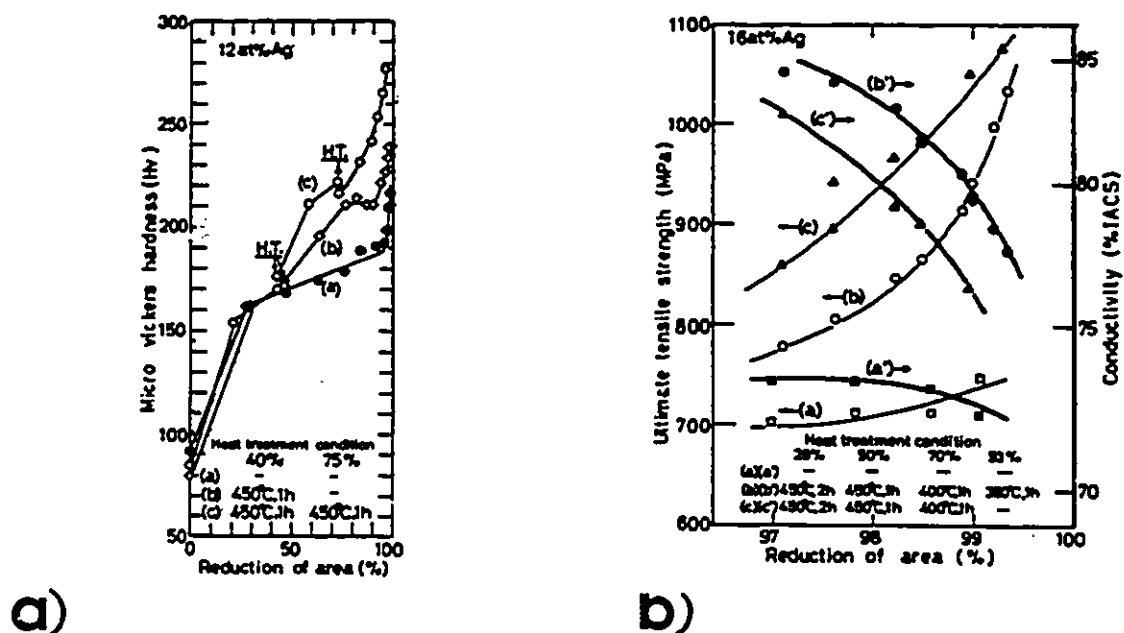


Figure 2-15 Elastic modulus and internal friction versus mean fibre diameter for drawn copper-silver wires.



a) **b)**
Figure 2-16 Hardness, strength and electrical conductivity as a function of strain and intermediate heat treatment.

further from this point were observed to have a marked decrease in dislocation density. When the spacing went below 250 Å the fibres were observed to be essentially dislocation free. While this is qualitatively similar to observations made in Cu-Nb wires, the work of Frommeyer and Wassermann is the most thorough, quantitative investigation of this phenomenon.

A second interesting phenomenon was observed by Sakai et al., (1991) in their investigation of copper-silver wires. These researchers found, by interrupting the drawing process and annealing the wires at 450°C for one hour, that the subsequently drawn material showed both a higher hardness and higher electrical conductivity. The data for a copper-12% silver alloy is presented in Figure 2-16 a) and b). The authors proposed that the increased work hardening after the heat treatments was the result of fine silver precipitates in the copper matrix, although micrographs to support this model were not provided.

It is interesting to examine the implications of the results in Figure 2-16 a). The net effect of the intermediate heat treatment appears to be a temporary increase in the subsequent work hardening rate, thereby reaching a higher strength level at the same imposed strain as the non-heat treated sample. To understand this process, however, it is necessary to first understand the stability of the microstructure and the effects of the intermediate heat treatments.

While it is unlikely that any one mechanism is responsible for the strengthening of two-phase materials over the range of applied strains, the preceding review has revealed that the essential aspect of high strength materials is related to their fine scale.

2.3 Stability of Two-Phase Wires

All of the strengthening mechanisms discussed in the preceding sections have associated with them an increase in stored energy. As the most stable form of any materials is that which has the lowest free energy, materials strengthened through cold deformation are inherently metastable.

The general concept of instability involves a reaction which lowers the free energy of, in this case, a deformed metal. The necessary prerequisites for this reaction to take place are a driving force and sufficient mobility. In the cases to be considered here, the mobility term is always related to some form of diffusional mass transport. The driving force for the various reactions is due to the excess energy present due to the operating strengthening mechanism(s). For the case of heavily-drawn, two-phase wires, however, it is presently unclear what strengthening mechanisms are in operation and, therefore, how the energy is

stored. There are two potential situations for energy storage that merit examination at this point, and they will now be considered in turn.

2.3.1 Elastic Stored Energy

Upon plastic deformation of a composite material in which the phases have different elastic moduli and yield points, a system of residual stresses is set up. For a composite with strong fibre reinforcement, it is possible to store elastic strain energy given by Equation 2.4 equal to:

$$W_{el} = \frac{\sigma_f^2}{2E_f}$$

where f is the flow stress and E_f is the Young's Modulus of the fibre. If the temperature is increased to a sufficient level for diffusion (i.e. sufficient mobility is provided) the matrix will creep in order to diminish the elastic strain in the fibre [see e.g. Marschall and Maringer, 1977]. For an aligned fibre composite with the fibre initially in elastic tension, this dimensional instability will cause the composite to decrease in length.

The second form of instability to be considered concerns the morphology of the structure. The creation of long filaments such as the niobium in the drawn copper-niobium composites is a source of excess free energy due to the very large surface area to volume ratio. From a strictly geometric point of view, the shape which minimizes this ratio is a sphere. However, the total free energy is also dependent upon surface energy of the crystal, which will vary for different crystallographic planes. The relative magnitude of the surface energy of different planes can lead to various equilibrium shapes [Porter and Easterling, 1988]. For a material with isotropic surface energy (i.e. constant over all crystallographic

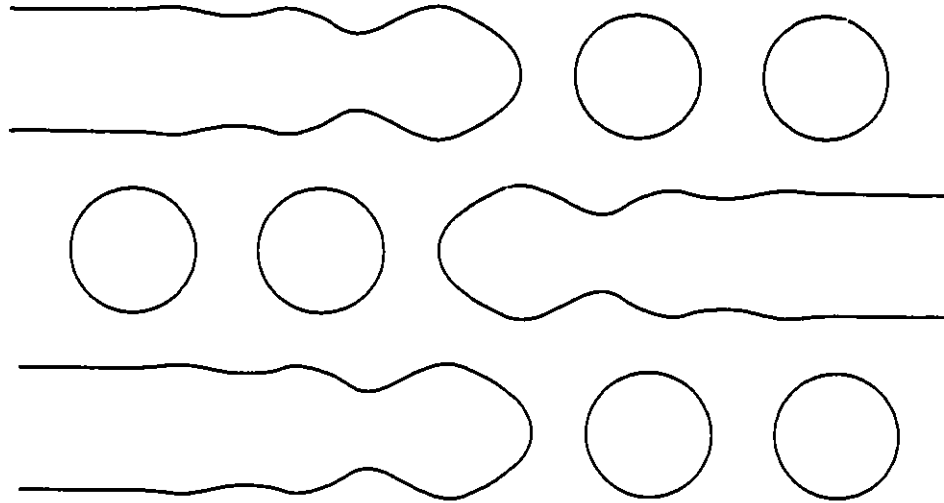


Figure 2-17 A schematic representation of the spheroidization process.

planes) the excess free energy is given by the excess surface per unit volume times the surface energy. For high aspect ratio filaments, this can amount to a substantial excess energy. Provided the diffusional mobility, it is expected that these filaments will spheroidize as shown schematically in Figure 2-17.

The work of Weatherly (1975) outlines the stability of rod-like structures at elevated temperatures. Based on the work of Nichols and Mullins (1965), assuming that interface diffusion is the dominant transport mechanism, the rate of growth of a sinusoidal perturbation in an infinite cylinder can be described by the equation:

$$\frac{d\delta}{dt} = \delta \frac{D_I \gamma v \Omega^2}{kT} \omega^2 \left(\frac{1}{r_0^2} - \omega^2 \right) \quad (2.28)$$

where D_I is the interface diffusion coefficient; δ is the perturbation amplitude; γ is the interfacial energy; v is the number of diffusing atoms per unit area; Ω is the atomic volume;

ω is the frequency of the perturbation; r_0 is the initial radius of the cylinder and kT has its usual meaning. The validity of Equation 2.28 as it is presented, is limited to the *small angle* approximation (i.e. when δ is small compared to r_0). A solution to the complete spheroidization reaction requires a numerical solution.

The solution to the spheroidization reaction is based on the reduction of surface energy in the system, and thus the driving force for the reaction enters as the equilibrium surface energy, γ , in Equation 2.28. In the case of heavily-drawn, two-phase wires, however, the interface between the two phases will be under traction and the true value of the surface energy is not known. Theoretical predictions suggest that the effective energy of a strained interface can reach values of the order of twice the equilibrium value — effectively doubling the spheroidization rate. [Greer, 1993]

2.4 Resistivity in Metals

Having described the microstructural aspects of strengthening in metals, it is the purpose of this section to provide a basic, and somewhat simplified, understanding of the effects of microstructure on the electrical properties of a metal. In designing materials for high-conductivity applications, a phenomenological view of the dependence of resistivity on temperature, solute content, dislocation density, and microstructural scale is required. To this end, a simple approach to describing resistivity will be reviewed.

If one considers a metal to be a lattice of atomic nuclei surrounded by a cloud of randomly moving electrons, then electrical current arises due to a net drift of electrons in the direction of decreasing potential. Resistance to the flow of current is due to the scattering

of electrons. An increase in the number or efficiency of scattering sites will increase the resistance of a metal. The resistance of a given piece of metal is dependent upon its geometry. For this reason, it is often more convenient to express the resistance to current flow in a material as the geometry independent resistivity, which in a wire of uniform cross-section is given by:

$$\rho = \frac{RA}{l} \quad (2.29)$$

where ρ is the resistivity in $\Omega \cdot \text{m}$, R is the resistance in Ω , A is the cross-sectional area in m^2 and l is the length in m.

By far the largest contribution to resistivity in pure metals is due to phonon scattering. The amplitude of lattice vibrations will increase with temperature, and thus it would be expected that the resistivity due to phonon scattering will also increase with temperature. A reasonable description of the variation of resistivity with temperature is given by the expression (Weiss, 1963):

Table 2-2 Debye temperatures for some pure materials.

Element	Θ [K]	Element	Θ [K]
Ag	220	Fe (bcc)	432
Au	177	Nb	250
Cu	315	Ni	390

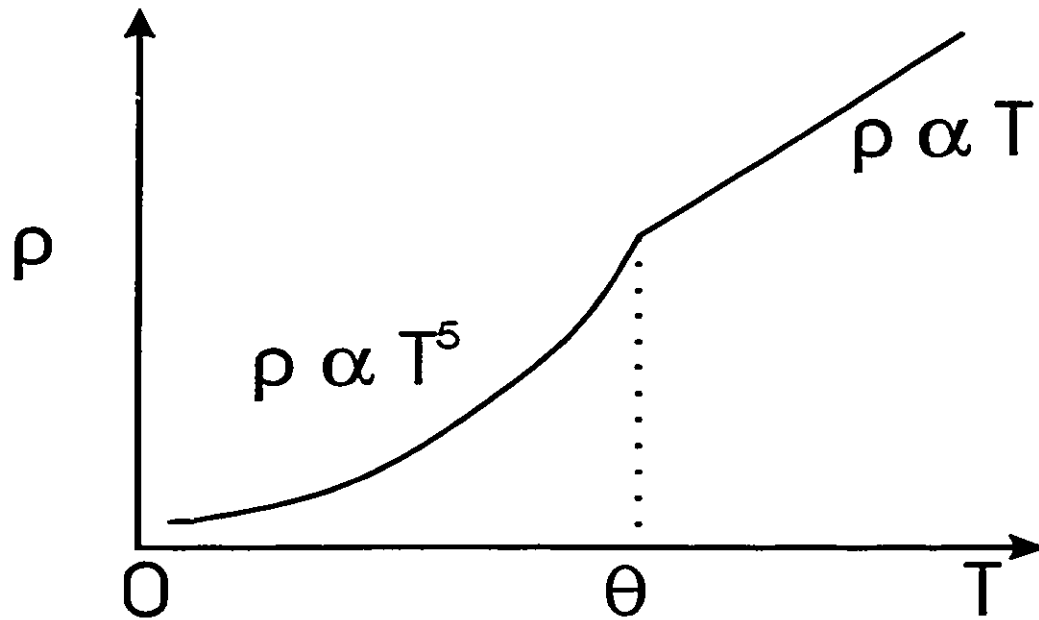


Figure 2-18 Resistivity versus temperature for a typical metal. Θ is the Debye temperature.

$$\rho_T = \frac{BT^5}{\Theta^5} J\left(\frac{\Theta}{T}\right) \quad (2.30)$$

$$J\left(\frac{\Theta}{T}\right) = \int_0^{\Theta/T} \frac{x^5 dx}{(e^x - 1)(1 - e^{-x})}$$

where T is the thermal resistivity, B is a material constant and Θ is the Debye temperature. The implication of this equation is shown schematically in Figure 2-18. Below the Debye temperature, the resistivity has a T^5 dependence, while it is generally linear above this temperature. The approximate values of Debye temperatures for various pure metals are listed in Table 2-2.

There are a number of potential scattering mechanisms in metals beside phonon scattering. The assumption that their contributions to the total resistivity are additive is known as Matthiessen's Rule. This can be simply expressed as:

$$\rho = \rho_T + \rho_a + \rho_b + \dots \quad (2.31)$$

where $\rho_{a,b,\dots}$ are the resistive contributions of other mechanisms. The assumption being made is that the individual mechanisms are independent of each other. For example, the contributions of other mechanisms are assumed to be independent of temperature.

Impurity atoms in the lattice provide a second source of electron scattering. At low concentrations, the impurity resistivity, ρ_i , is proportional to the concentration. Typical values are of the order 10^{-9} to $10^{-8} \Omega\cdot\text{m}$ per atom percent impurity [Weiss, 1963]. Thus the lowest resistivity in a single-phase material will be found in the purest form of that material and in two-phase alloys, those with the lowest mutual solid solubility.

Crystal defects also contribute to the bulk resistivity of a material. Their effect, however, is relatively small compared to impurity and particularly phonon scattering. Basinski and Saimoto (1967) have estimated the resistivity of a unit length of dislocation line to be of the order of $10^{-25} \Omega\cdot\text{m}^3$ ($10^{-19} \Omega\cdot\text{cm}^3$). To reach half of the room temperature resistivity of pure copper ($1.7 \times 10^{-8} \Omega\cdot\text{m}$) would require a dislocation density of 10^{17}m^{-2} . As was mentioned in the previous section on strengthening, densities of this magnitude are very unlikely.

The effects of grain boundaries and second phase particles are often very small in metals. The reason for this is found in comparing the grain size or interphase spacing with the mean free path of an electron. This in itself presents the first difficulty, as the mean free path of an electron is not easily calculated. It is typically estimated from measured values of resistivity by the formula:

$$\bar{x} = \frac{m \bar{v}}{n e^2 \rho} \quad (2.32)$$

where m is the mass, \bar{v} is the Fermi velocity, e is the charge, and n is the number of free electrons. For copper at room temperature, this mean free path is of the order of 40 nm; at liquid helium temperature the mean free path may increase by two or more orders of magnitude depending on the purity and defect content (i.e. the influence of other scattering mechanisms). For most materials at room temperature, therefore, the importance of grain boundaries and second phase particles as scattering sites is negligible because the distance between these obstacles is much larger than the mean free path of the electrons.

Frommeyer and Wassermann (1975b), in their investigation of the drawn copper-silver eutectic, found that at a given temperature, the resistivity of a sample increased significantly as the interphase spacing decreased. This was explained in terms of the ratio of the interphase spacing to the mean free path of electrons. Following the work of Dingle (1950) and Sondheimer (1952), the following relationships were found for the resistivity:

$$\rho_f = \begin{cases} \rho_b \left[1 + \frac{3\bar{x}}{4\lambda} (1+p) \right] & \lambda \gg \bar{x} \\ \rho_b \left(\frac{1-p}{1+p} \right) \frac{\bar{x}}{\lambda} & \lambda \ll \bar{x} \end{cases} \quad (2.33)$$

where ρ_f is the resistivity of the fibrous material, ρ_b is the resistivity of the bulk material, \bar{x} is the mean free path of the electrons, λ is the interphase spacing and p is the probability of the electrons being scattered elastically. Typical values of p were found experimentally to be in the range 0.10 to 0.15 (Frommeyer and Wassermann, 1975b). The result of applying these equations is the prediction that, at large interphase spacings, the resistivity is that of the bulk material, whereas at small spacings compared to the mean free path, the scattering at interfaces will dominate and the resistivity will be higher than that of the bulk.

A summary of these resistive mechanisms suggests that, to minimize the resistivity at a given temperature, it is necessary to minimize the impurity content in all of the phases in the material and to keep the microstructural scale larger than the mean free path of the electrons. Large dislocation densities will not make a significant contribution to the total resistivity except at very low temperatures, where the phonon contribution is significantly reduced.

2.5 Materials Selection

In the first section of this review, the design requirements of high-field, pulsed magnets were discussed in relation to the basic premise that the materials for construction of these magnets were required to have both high mechanical strength and high electrical conductivity. The second section described the underlying physical mechanisms which influence these properties and discussed the various materials that exhibit suitable combinations of strength and conductivity. If we consider that the design of a component requires definition of function and then selection of materials for that function, we require a rational method of examining the candidate materials in terms of a given design so that the best material may be chosen.

M. F. Ashby (eg. 1992) has developed a procedure which combines the design and materials aspects in the form of performance indices and selection charts. The result of adopting this approach is the ability to directly judge the relative merits of a set of materials as they relate to a specific design objective. In this section, the procedure for the derivation of performance indices and the use of selection charts will be explained to provide the background for their use in Chapter 5.

2.5.1 Deriving Performance Indices

The process of engineering design is one of characterization and optimization. Whether the design is for a new component or the replacement of an existing one, the goal is to achieve the best possible performance. Performance is judged by how well the design meets the objective(s) subject to the constraint(s) of the system. In engineering design, these objectives and constraints can virtually always be expressed in terms of mathematical equations, the variables in the equations falling into one of three categories:

1. **Function** - these values are typically fixed or have predetermined limits such as how fast a wheel must spin or what load a part must support.
2. **Geometry** - typically there is some leeway or range in which these values must fall.
3. **Material** - the material properties which govern the performance of the design.

The goal of deriving performance indices is to combine the objective and constraint equations to directly relate the physical properties of the candidate materials to the final performance of the design. The steps involved in this process are enumerated below.

1. Identify the attribute, p , to be maximized or minimized and develop an equation for this attribute. This equation is known as the **Objective Function**.

$$p = F(F, G, M) \quad (2.34)$$

2. Identify the free variable(s) in the objective function. These are quantities that are not fixed by some aspect of the design.

- 3 Identify and develop equations for the constraints in the design.
4. By algebraically rearranging the constraint equation, obtain an expression for the free variable and substitute that expression into the objective function.
5. You now have an expression for the design objective in terms of the constraints on the system. Rearrange the variables in the objective function into the three categories — Function, Geometry, and Materials.
6. Simply read the performance index, M , to be maximized (or minimized). Depending upon whether p is to be maximized or minimized, the material with the highest or lowest value of M will best meet the objective subject to the applied constraint.

2.5.2 Selection Charts

Having derived a performance index for a particular application, it is necessary to assess the merits of various materials in terms of this index. The most direct approach to this would be to calculate the indices for the materials of interest and simply choose the one with the highest performance index. However, in order to compare materials or develop a rationale for the improvement of materials, it is of value to develop selection charts. In its most general form, a performance index may be expressed as:

$$M = \frac{A^m}{B^n} \quad (2.35)$$

and all materials with the same value of M will perform equally well for the given objective and constraints. If the quantities A and B were plotted on logarithmic scales, materials of

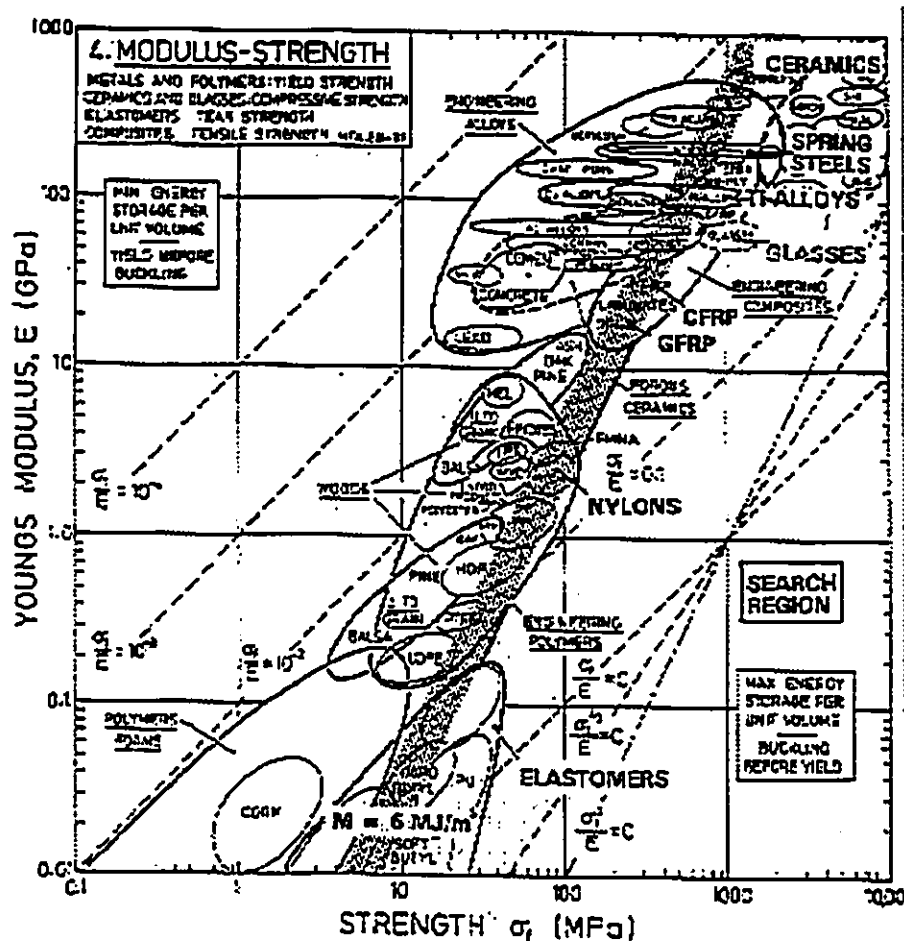


Figure 2-19 A materials selection chart based on the strength and Young's modulus of the material. (Ashby, 1992).

equal performance would be connected by straight lines of slope n/m , described by the equation:

$$\log A = \frac{n}{m} \log B + \frac{1}{m} \log M \quad (2.36)$$

Figure 2-19 is a selection chart from "Materials Selection in Mechanical Design" (Ashby, 1992) based on strength and stiffness. For the performance index $M = \sigma_f^2/E$, lines of slope 2 connect materials of equal performance levels. Materials above and to the left of these lines have higher values of M , while those below and right have lower values of M .

An advantage to this approach over calculating the individual performance indices is that, once the chart is constructed, it may be used for any combination of, in this case, σ_f and E raised to any power by simply using a selection line of a different slope.

2.5.3 Multiple Objectives

To this point, the use of selection charts has been dealt with for the case of a single objective and a single constraint. This scenario is the simplest case and yields one performance index which is dealt with using a single chart as in Figure 2-19. For the purposes of this thesis, however, it will be necessary to deal with the case of having a single objective and multiple constraints. The methods of approaching this will be discussed here.

In the case of an over constrained problem, the performance indices are derived independently for each constraint, (i.e. the previously outlined procedure is followed for each constraint as if it were the only constraint) generating n performance indices and n objective functions:

$$\begin{aligned} p_1 &> f(F_1, G_1, M_1) \\ p_2 &> f(F_2, G_2, M_2) \\ &\cdot \\ &\cdot \\ &\cdot \\ p_n &> f(F_n, G_n, M_n) \end{aligned} \tag{2.37}$$

For simplicity, we will consider the case of two independent performance indices. The performance limit due to the first constraint is established by the first objective function and the second objective function sets the limit due to the second constraint. The design will best utilize a material's properties if the performance limit due to both constraints are met simultaneously. That is:

$$\begin{aligned}
 p_1 &= p_2 \\
 F_1 G_1 M_1 &= F_2 G_2 M_2 \\
 M_1 &= \frac{F_2 G_2}{F_1 G_1} M_2
 \end{aligned}
 \tag{2.38}$$

If a selection chart is created which plots M_1 vs. M_2 on logarithmic scales, coupling lines of slope $F_2 G_2 / F_1 G_1$ may be plotted indicating the best combination of properties for a given design. The details of the design and final application are contained in the expression $F_2 G_2 / F_1 G_1$.

While there do exist other approaches to materials selection for overconstrained problems such as weighting functions (see eg. Charles and Crane, 1989; Dieter, 1991), this method has the advantage that it removes the need for judgements to be made on the relative importance of the individual constraints. It allows for a direct correlation to be made between a material choice and the final performance of the design.

3. Experimental Procedures

The experimental work included in this thesis covers a range of materials and experimental techniques. This chapter of the thesis is divided into three sections covering: 1) the materials involved, 2) the experiments and their objectives, and 3) the details of the techniques employed.

3.1 Materials

3.1.1 Pure Materials

Oxygen free, electrolytic (OFE) copper (designated C101) was obtained locally from Copper and Brass Sales Ltd. in the form of a $\frac{3}{8}$ inch (9.5 mm) diameter rod. The specified purity was 99.99% (see Table 3-1). This copper was used in the as-received condition (cold drawn to unknown strain) and also recast under vacuum to provide a common reference point with the cast copper-niobium alloys described below. Niobium (99.8%, see Table 3-2) was obtained from Johnson & Matthey in the form of 1 mm diameter wire.

3.1.2 Copper-Niobium Alloys

The copper-niobium phase diagram is shown in Figure 3-1 (Okamoto, 1991). There is uncertainty in the literature regarding the nature of the phase diagram at low niobium

concentrations, however, this aspect is of little consequence to the work described in this thesis.

Three copper-niobium alloys were used in this work. Alloys of 15 and 18 weight percent (16 and 19 atomic percent) niobium were provided by Los Alamos National Lab. in the form of drawn wire with a rectangular cross-section of 2 mm by 3 mm. These materials were produced at Ames Lab., Iowa via the consumable arc melting process described by Verhoeven et al. (1986). The cast ingot was reduced by a sequence of rod rolling, swaging and wire drawing at Supercon Ltd, (Shrewsbury, Mass.). After the initial reduction, the wire was consolidated by a process of rebundling, hot isostatic pressing and further reduction by wire drawing. The rebundling process was necessary to attain the combination of the high reduction necessary for strengthening and a suitable final cross-section. The total imposed strain in these two materials is unknown, however, it is estimated from the final dimensions to be of the order of $\epsilon=10$ (99.995% R.A.).

Table 3-1 Analysis of impurities in the as-received copper (in ppm) supplied by Copper and Brass Sales.

Bi	Cd	Pb	Hg	O ₂	P	Se	S	Te	Zn
<1	<1	4	<1	3	2	<1	9	<1	<1

Table 3-2 Analysis of impurities in the as-received niobium (in ppm) supplied by Johnson Matthey.

Al	C	Cr	Cu	Fe	H	Hf	Mo	N	Ni	O	Si	Ta	Ti	W	Zr
<20	<5	<20	14	46	2	<20	<20	24	<20	86	<20	400	<10	<200	<10

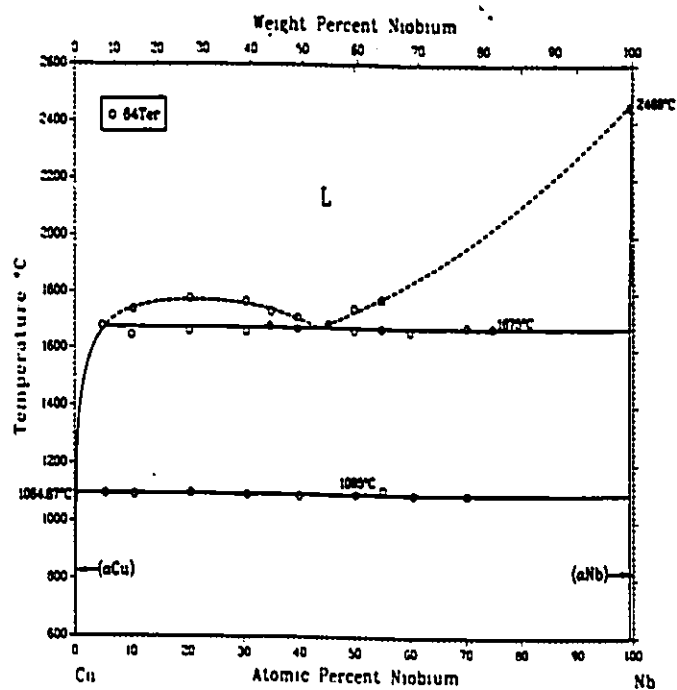


Figure 3-1 The copper-niobium phase diagram after Okamoto and Massalski, (1991).

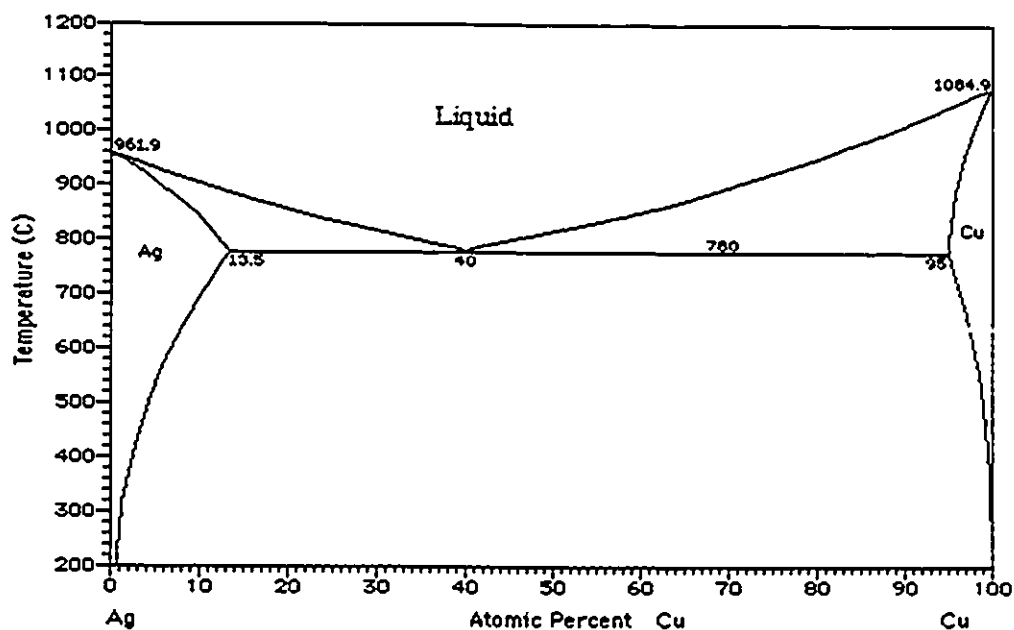


Figure 3-2 The copper-silver phase diagram after Subramanian and Perepezko, (1993).

A third alloy of 0.5wt% niobium was cast at McMaster University by vacuum induction melting in a high density, graphite mould. The starting materials were the pure copper and niobium described above. The directionally solidified, cylindrical casting had a final diameter of 10 mm and a length of 150 mm.

3.1.3 Copper-Silver Alloy

The copper-silver phase diagram is shown in Figure 3-2. This binary system exhibits a simple eutectic at 72wt% (60 at%) silver. The Cu-24wt%Ag (16at%) alloy used in this work was provided by Y. Sakai, NRIM, Japan, through NHMFL, Los Alamos. The alloy was continuously cast using conventional methods. The procedure was described by Sakai et al. (1992). The material was supplied in various forms including the as-cast condition, and after drawing to various strains with and without the intermediate heat treatments described in Chapter 2.

3.2 Experimental Objectives

It is convenient to subdivide this section with respect to the five principle objectives of the experimental work.

1. To provide a description of the co-deformation of two-phase wires.
2. To investigate the evolution of electrical resistivity with strain.
3. To study the morphological stability of drawn Cu-Nb and Cu-Ag wires.

4. To investigate the effects of intermediate heat treatments on the mechanical response of drawn Cu-Ag wires.

5. To investigate the strengthening mechanisms in heavily-drawn, two-phase wires.

To attain these objectives, combinations of various experimental procedures were used.

3.2.1 Co-deformation of Copper-Niobium Wires

To understand the mechanical behaviour of two-phase materials, it is necessary to know how the second phase deforms so that its role in strengthening may be evaluated. It is of interest determine if the second phase remains continuous or breaks up into smaller segments and to determine the magnitude of the residual stresses in the second phase. This series of experiments involved the drawn, Cu-1wt%Nb and Cu-15wt%Nb wires, and the Cu-24wt%Ag wire.

The copper-niobium system is especially well suited to this type of investigation as the niobium filaments may be extracted from the matrix by dissolving the copper in nitric acid. Niobium filaments were extracted from the Cu-1wt%Nb in the as-cast condition and after wire drawing strains of 3, 4, and 5 (95, 98, and 99% reduction in area). Scanning electron microscopy was used to obtain information on the general shape of the filaments, while atomic force microscopy allowed a detailed examination of the surface topology of the filaments. Filaments drawn to $\epsilon=5$ as well as filaments extracted from the Cu-15wt%Nb wire were observed using transmission electron microscopy to assess their internal structure.

To study the co-deformation of the copper-silver wires, longitudinal and transverse TEM samples were prepared after various imposed strains.

The degree of elastic stress in the filaments was assessed in two ways. The first, very simple experiment involved comparing the filaments exposed in the above experiment with those that had been extracted from wires after annealing at 300, 400, and 500°C. Stress-free filaments should remain straight, while those with residual elastic stresses will alter their shape to relieve the stress.

A second experiment was devised in an attempt to determine the magnitude of the residual stresses in the second phase filaments. Dilatometry measurements were made on four samples: 1) pure copper, drawn from the as-received material (additional strain $\epsilon=2.7$), 2) annealed, pure copper, 3) drawn Cu-18wt%Nb (strain unknown), and 4) drawn Cu-24wt%Ag ($\epsilon=4.3$, no int. heat treatment). Each sample was exposed to the temperature profile shown in Figure 3-3. The heating rate of 5°C/min was chosen as a compromise between fast heating and minimal overshoot of the plateau temperature. In these experiments, changes in length with temperature and time were measured to detect creep in the wires due to the relaxation of residual stresses.

3.2.2 Evolution of Electrical Resistivity

As was discussed in Chapter 2, it is a general effect that the mechanisms which are responsible for strengthening metals also cause an increase in the electrical resistivity. While it is not the primary thrust of this thesis work, it is important from the magnet design point of view to understand how the resistivity evolves during the deformation of these two-phase wires. Electrical resistivity was measured as a function of imposed strain and temperature

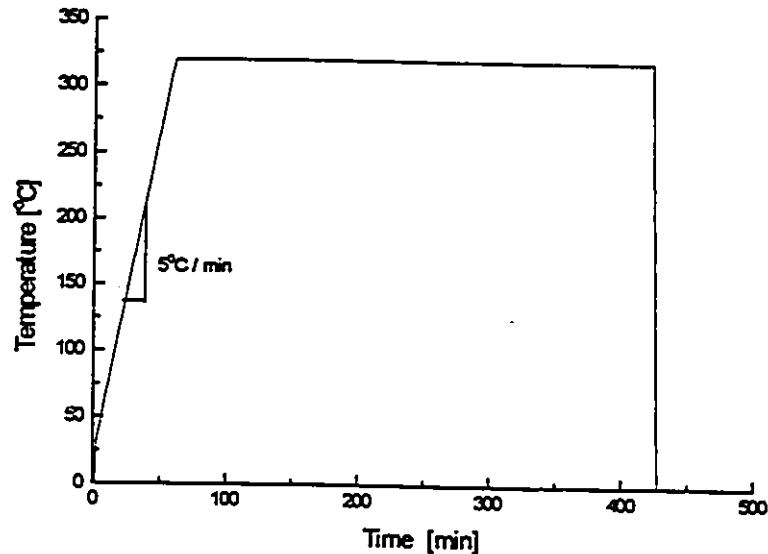


Figure 3-3 The nominal imposed temperature profile of the dilatometry experiments.

for three materials. To first provide a basis for comparison, measurements were made on drawn pure copper. Measurements were also performed on the Cu-1wt%Nb wires and a fully annealed and redrawn piece of the Cu-24wt%Ag.

3.2.3 Morphological Stability of CuNb and CuAg Wires

To investigate the morphological stability of these two-phase wires, a series of isochronal annealing experiments were conducted on the Cu-15wt%Nb and Cu-24wt%Ag wires. Samples of each wire were held at 100, 200, 300, 400, and 500°C for a period of one hour. Subsequent observations of longitudinal and transverse sections of each wire were made by transmission electron microscopy.

3.2.4 Intermediate Heat Treatments

The purpose of this set of experiments was to first, attempt to reproduce the results of Sakai et al., (1992), discussed in Section 2.2.8, and subsequently to provide an explanation for the increased hardening displayed by the samples after the imposition of the intermediate heat treatments.

A section of Cu-24wt%Ag materials in the as-cast condition was obtained from Y. Sakai (NRIM, Japan) and the following samples were prepared:

<u>Sample Number</u>	<u>Imposed Strain</u>	<u>Heat Treatment</u>
CA0_0	As-cast	No H.T.
CA63_0	$\epsilon=0.63$ (40% R.A.)	No H.T.
CA63_1	$\epsilon=0.63$	450°C, 1 hr @ $\epsilon=0.63$
CA136_0	$\epsilon=1.36$ (75% R.A.)	No H.T.
CA136_1	$\epsilon=1.36$	450°C, 1hr @ $\epsilon=0.63$
CA136_2	$\epsilon=1.36$	450°C, 1hr @ $\epsilon=0.63$ and 450°C, 1hr @ $\epsilon=1.36$

Each of these samples were observed by transmission electron microscopy and tested for Vickers hardness.

3.2.5 Investigation of the Strengthening Mechanisms

To gain an understanding of the mechanisms involved in strengthening heavily drawn, two-phase wires, it is necessary to be able to separate the possible effects of the various aspects of the deformation. For example, if the second phase is hard and does not

deform, then there is the possibility for the generation of geometrically necessary dislocations to accommodate the overall shape change or fragmentation of the second phase. The results of the previous experiments were used to quantify the shape change of the second phase with strain.

To assess the effect of macroscopic strengthening, tensile specimens were made from Cu-18wt%Nb and Cu-24wt%Ag. The dimensions of the samples are shown in Figure 3-4. Samples of each material were tested at room temperature, after annealing for one hour at 250°C, and after annealing at 500°C for one hour. If significant strengthening is due to load transfer to the second phase, then there may be an increase in flow stress of the copper-niobium sample between room temperature and liquid nitrogen due to the strong temperature dependence of the flow stress in the bcc niobium. The effects of residual stress in the second phase may be determined by comparing the room temperature and annealed sample tests.

3.3 Experimental Techniques

3.3.1 Wire Drawing

Wire drawing was performed using a drawing device constructed for use on a screw-driven Lloyd tensile testing machine. The major components of the apparatus are shown in Figure 3-5. The device consisted of three components. The bottom section held the wire die and was attached to top section by three, equally spaced connecting rods of six or twelve inches in length. Drawing was accomplished by fixing the top section to the

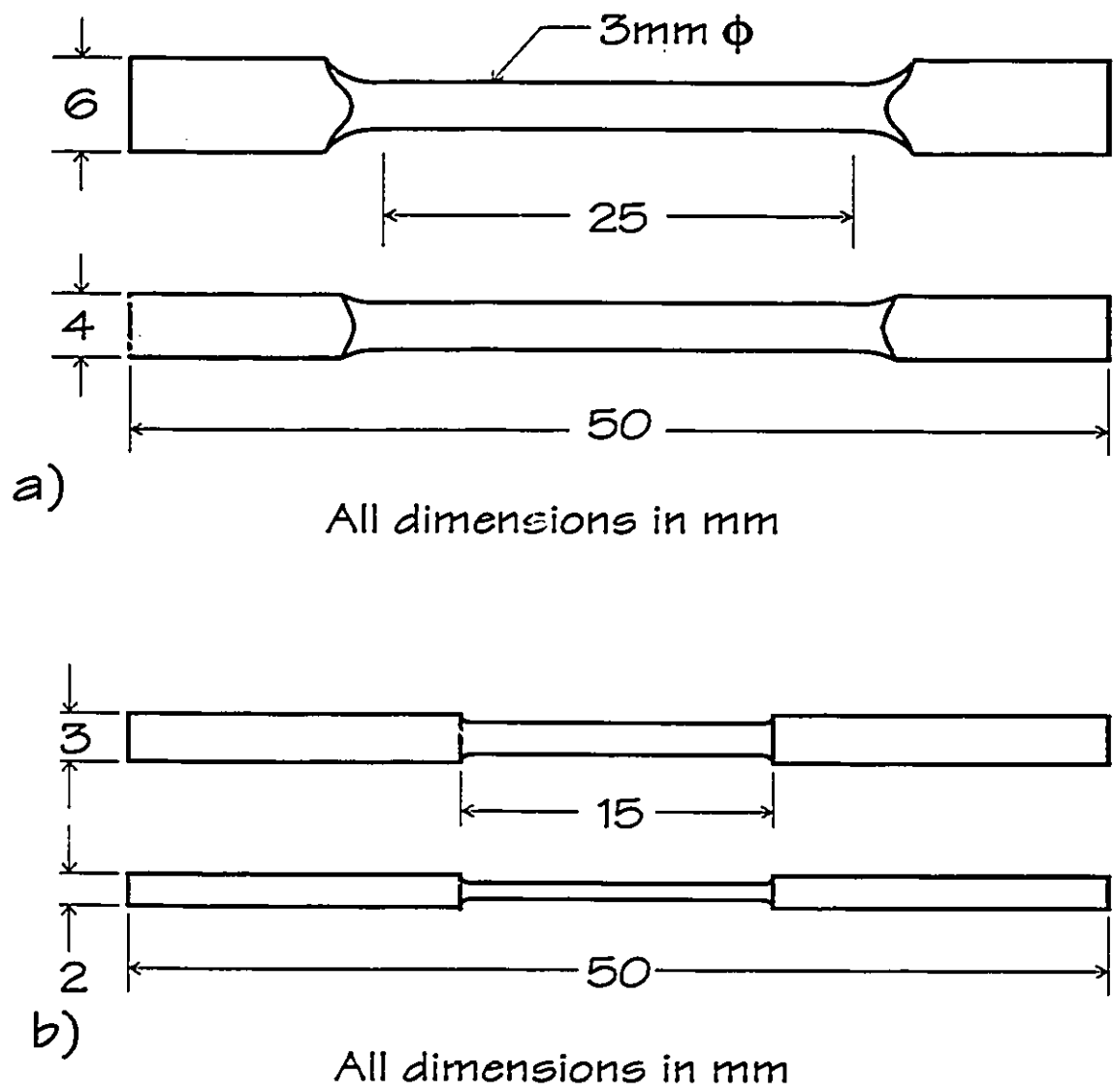
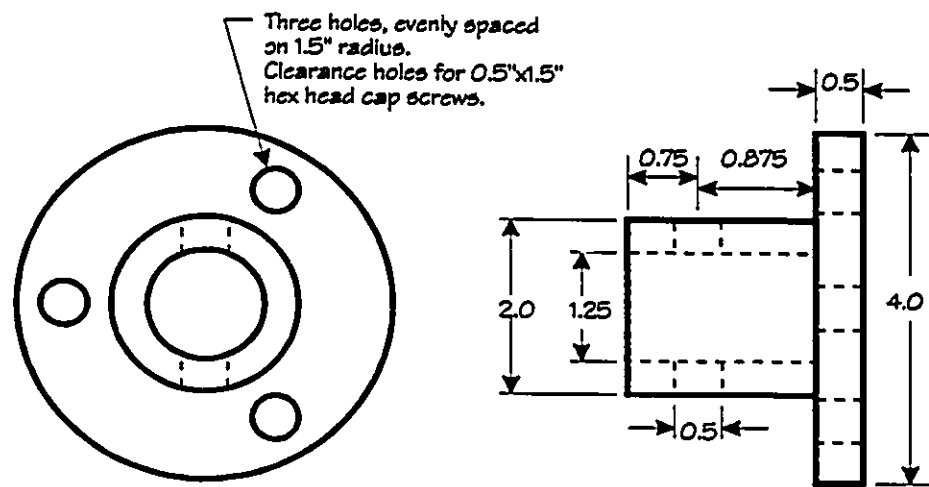
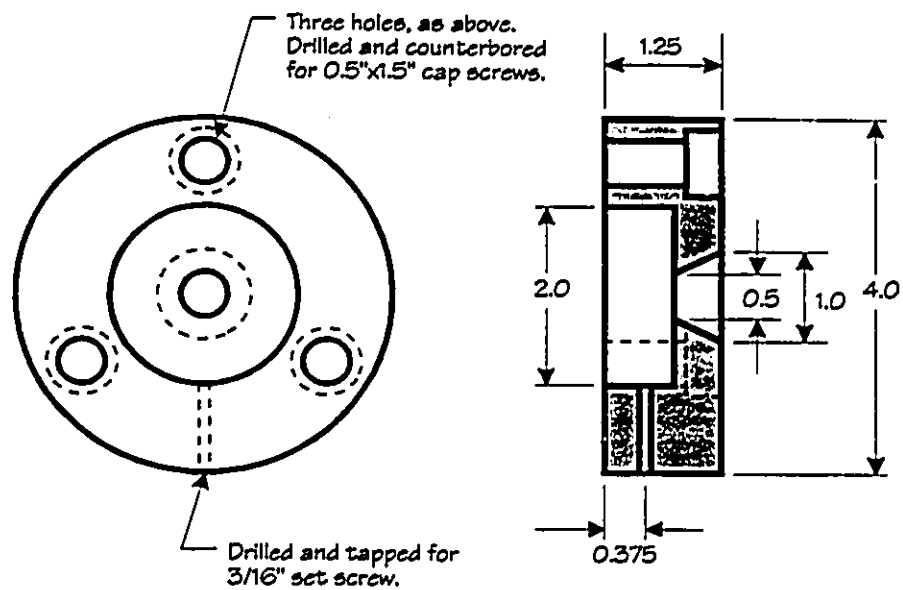


Figure 3-4 Geometry of the a) Cu-24wt%Ag and b) Cu-18wt%Nb tensile samples.



Top Section



Bottom Section

Material: Mild Steel

All dimensions in inches

Figure 3-5 Drawing of the major components of the wire drawing apparatus.

cross-head of the testing machine, passing the pointed wire through the die and holding the pointed end in the standard jaw grips of the testing machine.

Wires of initial diameter greater than 2.5 mm were pointed by rotary swaging, while wires of smaller diameters were pointed by chemical etching. For all wires except copper-niobium alloys, concentrated nitric acid was used for this procedure. Because niobium is unaffected by nitric acid, a solution of 2 HF : 1 HNO₃ : 2 HCl was used. Drawing speeds were typically 2 mm/sec. The available wire dies ranged in size from 10.0 mm (0.394 in) to 0.025 mm (0.001 in). For the copper alloys drawn in this work, liquid paraffin was found to be a suitable drawing lubricant.

3.3.2 Metallography

Samples for optical microscopy and Vickers hardness testing were prepared using standard metallographic techniques and polished to 1 μ m using diamond paste. Copper-niobium samples for SEM and TEM were prepared as outlined by Pelton et al. (1987) with the following exceptions.

1. TEM foils were ground to 250 μ m before dimpling.
2. Acetic acid (C₂H₃OOH) was used in place of methyl hydroperoxide (CH₃OOH) in the final etching solution.

TEM foils of the Cu-Ag wires were also fabricated by mechanical grinding and dimpling followed by ion milling on a liquid nitrogen cooled stage.

3.3.3 Extracted Niobium Filaments

The process of extracting the filaments involved first dissolving the copper matrix with concentrated nitric acid in a test tube. The remaining solution was diluted with distilled water and the niobium filaments allowed to settle to the bottom of the tube. The majority of the liquid was drawn off and then the tube was refilled with distilled water. These steps were repeated until visible traces of the copper nitrate solution were no longer present, and the liquid had a neutral pH level. The final step was to draw off as much water as was practical and refill the container with methanol. A methanol suspension was preferred for final SEM and TEM sample preparation because of the faster evaporation times.

From the alcohol suspension, specimens were made for TEM and AFM by placing one drop of the suspension on a carbon-coated, copper TEM grid and allowing the alcohol to evaporate. The same sample could be used for both TEM and AFM. Samples for SEM were prepared by drawing the alcohol through Nuclepore, polymer filter paper (0.1 μm pore size) as shown schematically in Figure 3-6 and leaving the niobium filaments. The filter paper was then mounted on the appropriate sample stub with silver paste and coated with platinum or gold to permit electrical conduction.

3.3.4 Resistivity Measurements

Resistivity measurements were made at Los Alamos National Lab. by Dr. M.F. Hundley. Resistivity was measured as a function of temperature from liquid helium (4 K) to 300 K. The temperature variation is accomplished by mounting the samples to a heated plate which is then submerged in a dewar of liquid helium. When the temperature has

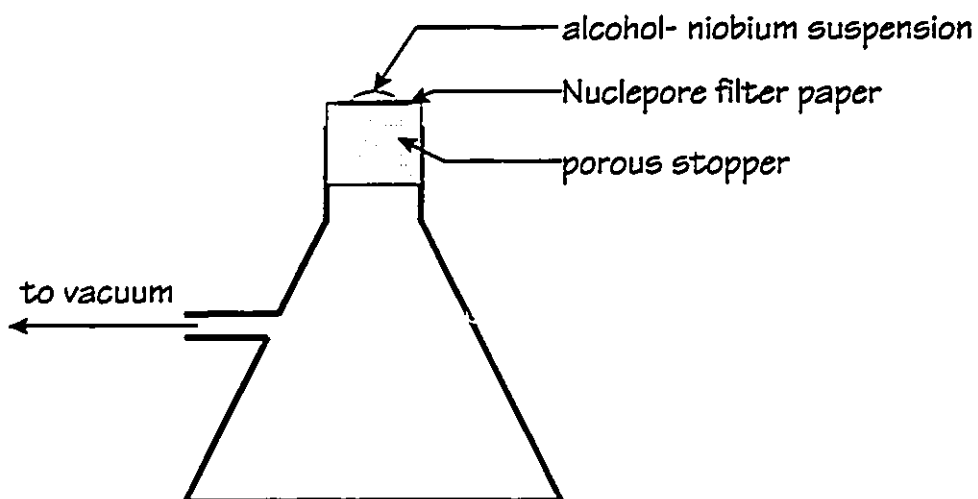


Figure 3-6 Schematic diagram showing the vacuum process for preparing niobium filament samples for the SEM.

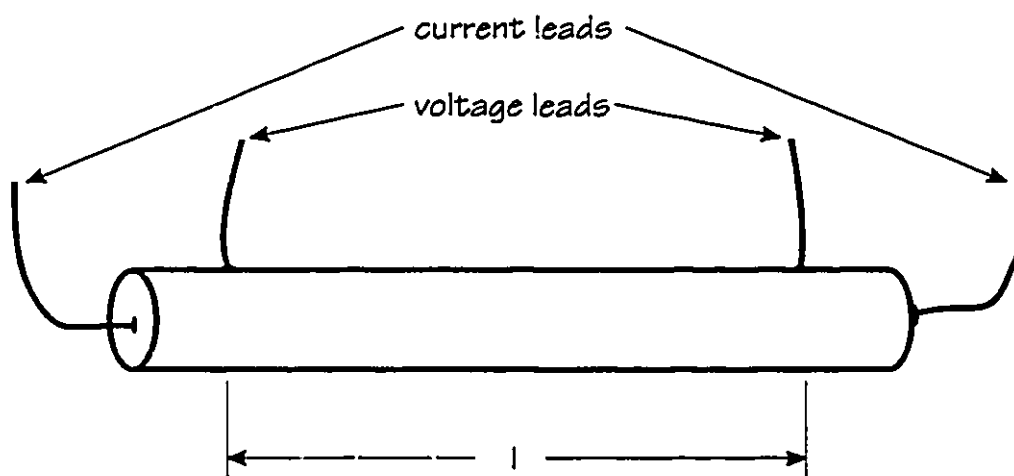


Figure 3-7 Schematic representation of the electrical connections for the 4-probe, electrical resistivity measurement.

stabilized, the plate temperature may be increased via a temperature controller to attain the desired heating profile.

Measurements were made by the standard 4-probe technique (as shown in Figure 3-7) and voltages were taken as the average of the forward and reversed polarity values to eliminate thermoelectric effects. Electrical connections were made with silver paste.

3.3.5 Texture Measurements

Texture measurements were performed at Los Alamos National Laboratory on a five-axis, Scintag goniometer with an oscillating stage. Using standard metallographic techniques, transverse sections of bundles of wires were prepared such that a minimum of 1 cm^2 of surface was provided for texture measurement.

3.3.6 Dilatometry

Dilatometry measurements were carried out on a Theta Industries dilatometer under a constant spring load. Samples were run against an alumina reference sample of similar size. Computer-based data acquisition collected data on specimen temperature and expansion.

3.3.7 Mechanical Testing

Vickers microhardness tests were performed on a Shimadzu Type M₁ microhardness tester using indentation loads of 200 g and a dwell time of 15 seconds.

Tensile tests were performed on an MTS, servohydraulic testing machine (model #810) fitted with a 100 kN load cell. A cross-head speed of 0.01 mm/sec was used for all tests on this machine.

4. Experimental Results

The purpose of this chapter is to present the results of the experimental work described in Chapter 3. The data will be presented in the following order.:

1. General microstructural observations of the materials at various points during the drawing process (i.e. at various imposed strains).
2. Observations of niobium filaments extracted from the wire after different levels of imposed strain.
3. Results from experiments on microstructural and dimensional stability.
4. Results from mechanical property tests performed at McMaster and Los Alamos National Laboratory.
5. Measurements of electrical resistivity.

4.1 Microstructural Evolution

4.1.1 Copper-Silver Wires

The initial structure of the the copper-silver wires is that of a typical hypoeutectic alloy. Figure 4-1 is an optical micrograph of the as-cast Cu-24wt%Ag material. The solidification microstructure consists of primary copper dendrites surrounded by regions

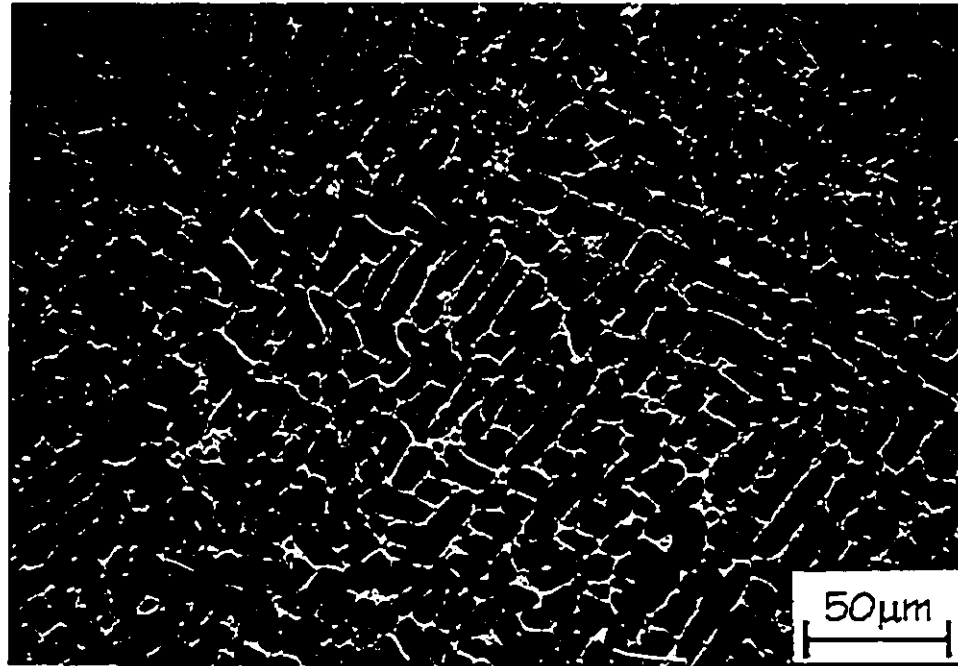


Figure 4-1 An optical micrograph of the as-cast Cu-24wt%Ag alloy. The structure consists of primary copper dendrites surrounded by copper-silver eutectic.

copper-silver eutectic with a rod morphology. The eutectic regions are revealed as the light areas in Figure 4-1, but the eutectic structure is too fine to resolve in this micrograph.

The heavily drawn structure of these two-phase wires is very fine. Observations of microstructural evolution, therefore, require transmission electron microscopy. Figure 4-2 a) and b) are TEM micrographs of transverse and longitudinal section of the same alloy drawn to a strain of 4.3. There are three important observations to be made regarding these micrographs: i) the silver filaments remain continuous and have aligned with the wire axis; ii) dislocation lines may be seen traversing the copper matrix between parallel silver filaments; and iii) in the longitudinal section, the matrix contrast remains constant over large distances compared to the filament spacing, indicating that large strain gradients are not present. In the transverse section, the contrast changes from grain to grain, although it is not seen to vary within individual grains. There were also observations of some twinning

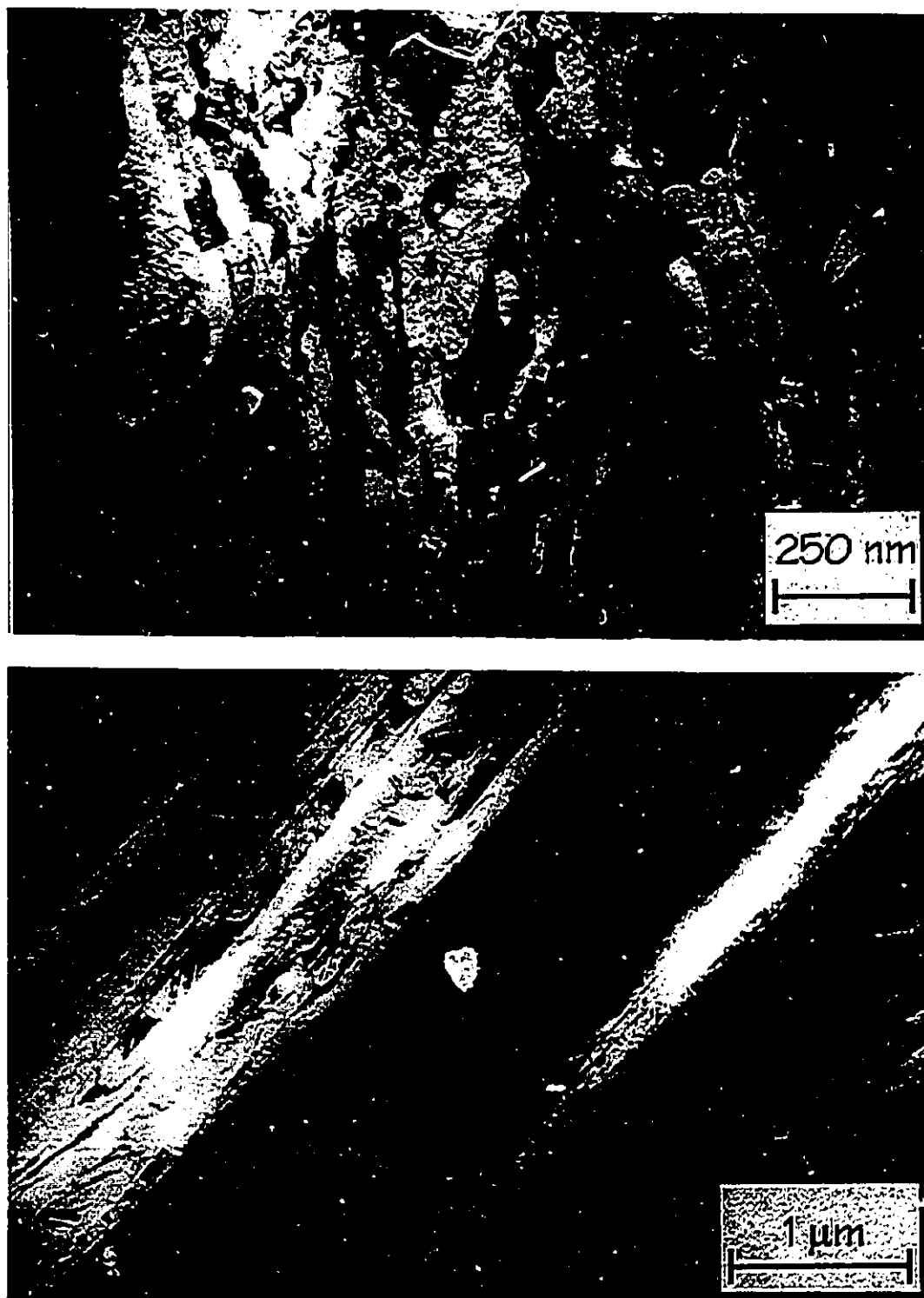


Figure 4-2 TEM micrographs of a) transverse and b) longitudinal sections of the Cu-24wt%Ag wire drawn to a strain of 4.3.

in the copper-silver wires, although it did not make a significant contribution to the total deformation, and will not be considered further.

4.1.2 Copper-Niobium Wires

The Cu-15wt%Nb and Cu-18wt%Nb wires were supplied in the as-drawn condition. From literature accounts, it is known that the initial microstructure consists of niobium dendrites in a copper matrix as described in Chapter 3. The dendrite arms were reported to be in the range 5 – 10 μm .

Transmission electron microscopy was used to examine the deformed structures. Figures 4-3 a) and b) are transverse and longitudinal micrographs of the as-drawn Cu-15wt%Nb wire after an estimated strain of 10. The longitudinal section is similar to the copper-silver alloy in that the niobium filaments are continuous and aligned with the wire axis and dislocation lines are visible between the niobium filaments. The transverse section reveals the elliptical cross-section of the niobium filaments due to the plane strain deformation created by the $\langle 110 \rangle$ bcc texture development (Hosford, 1964), and the complexity of the as-drawn structure in f.c.c. - b.c.c. composites.

4.2 Extracted Niobium Filaments

The copper-niobium system is particularly well suited to examination of the second phase morphology because the copper matrix may be dissolved in nitric acid without affecting the niobium. Figure 4-4 is a transverse section of the Cu-18wt%Nb wire. The

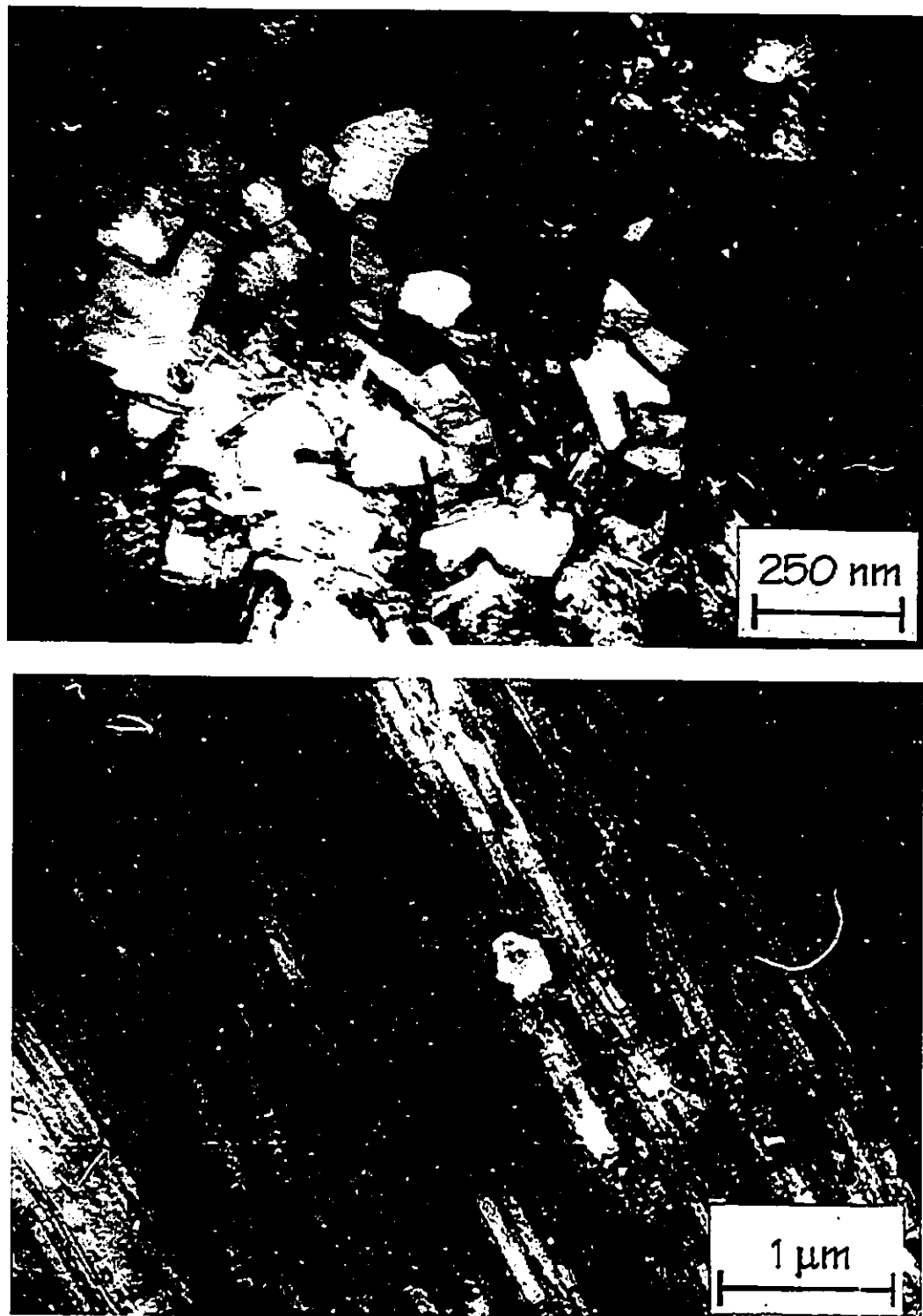


Figure 4-3 TEM micrographs of a) transverse and b) longitudinal sections of the drawn Cu-15wt%Nb wire.

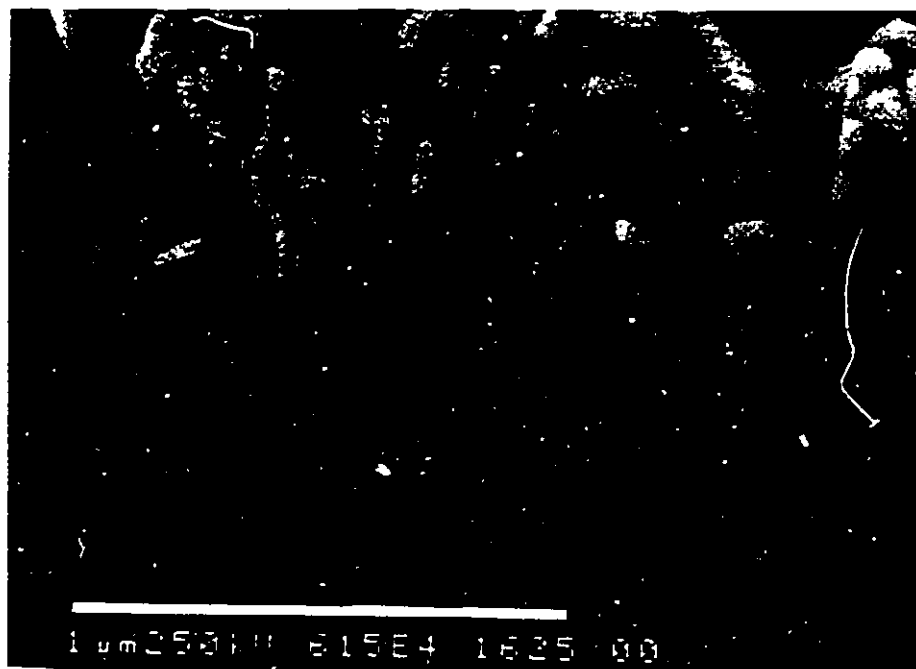


Figure 4-4 A transverse SEM micrograph of the drawn Cu-18wt%Nb wire with the copper matrix etched to reveal the niobium filaments.

copper matrix has been etched to leave the filaments exposed. The elliptical cross-section of the filaments is evident in this micrograph.

If the matrix is completely dissolved, the filaments may be examined by a number of techniques. Figure 4-5 a) and b) are SEM micrographs of niobium extracted from the Cu-1wt%Nb wire in the as-cast condition and after an imposed strain of 5. The drawn filaments are curled after extraction which indicates the presence of residual elastic stresses in the filaments before extraction.

After an imposed strain of 5, the filaments extracted from the Cu-1wt%Nb wire are thin enough to be imaged by transmission electron microscopy. Figure 4-6 is a TEM micrograph of an extracted filament. It is interesting to observe that the filaments are essentially dislocation free. This was true of all of the filaments imaged in this condition.

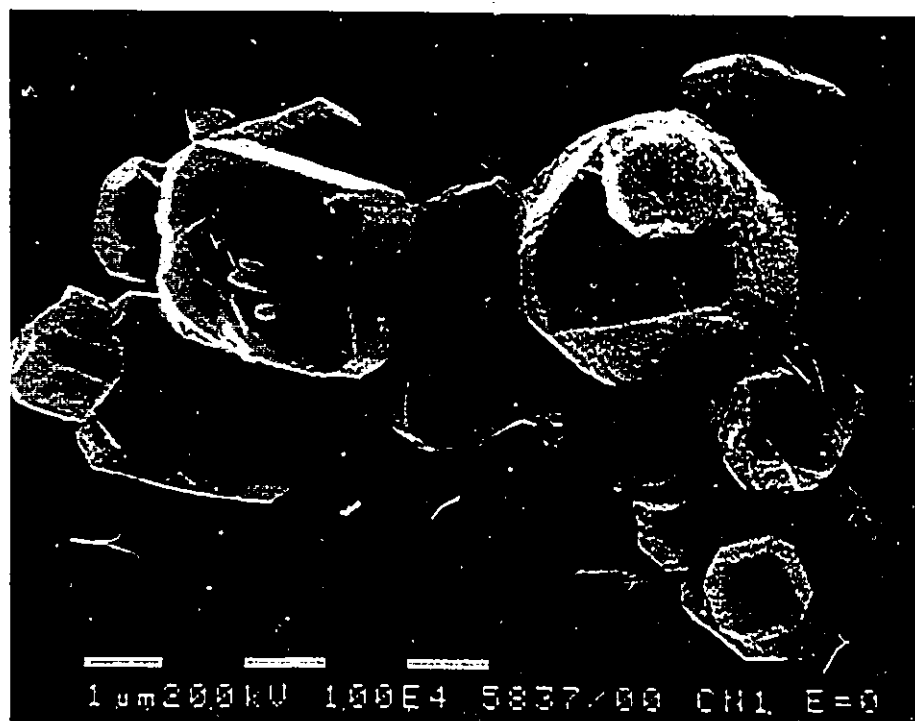


Figure 4-5 SEM micrographs of niobium extracted from the Cu-1wt%Nb wire in the a) as-cast condition and b) after a strain of 5.

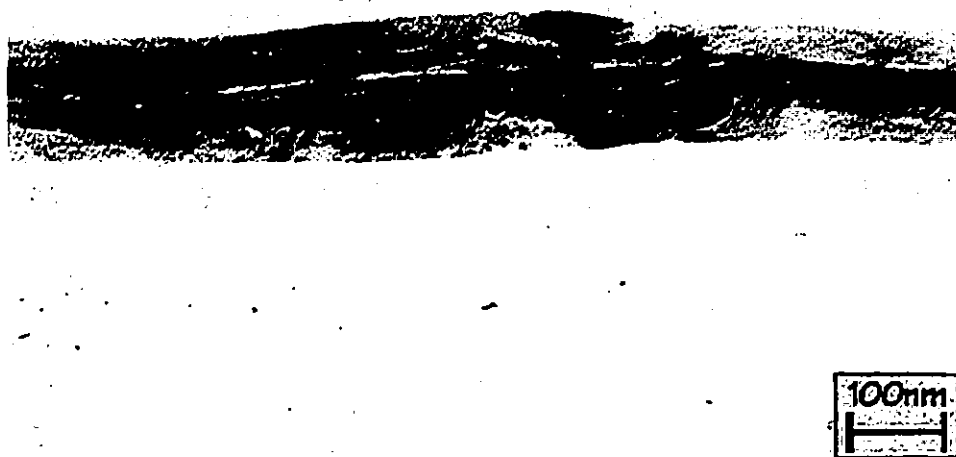


Figure 4-6 A TEM micrograph of a niobium filament extracted after a strain of 5. The filament is dislocation free.

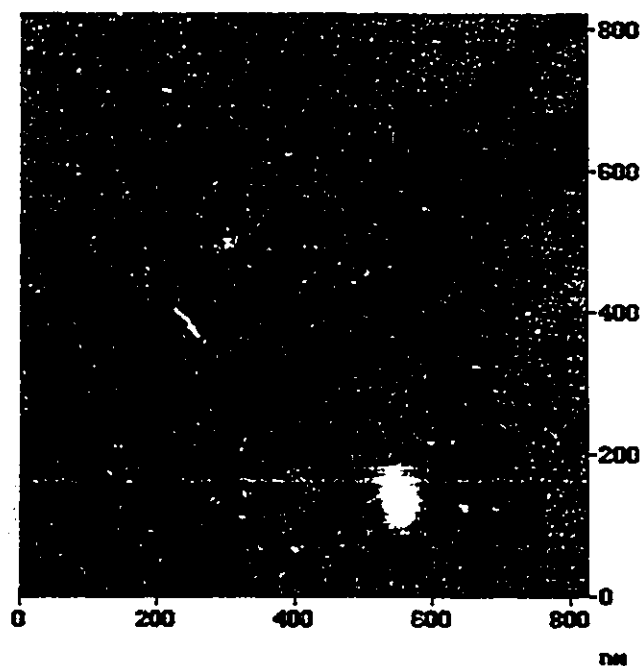


Figure 4-7 An AFM image of a niobium filament extracted after a strain of 5. The striations make an angle of 57° with the filament axis.

The extracted filaments were also imaged with the atomic force microscope. Figure 4-7 is an AFM image of a filament extracted from the Cu-1wt%Nb wire. At imposed strains greater than 4, all of the filaments exhibited striations at a measured angle of approximately 57° with the filament axis. While the presence of the striations appears to be a reproducible phenomenon, their origin is not clear. In the following Chapter, the existence of the striations will be discussed in terms of the co-deformation of the composite wires, however, the experimental evidence is not sufficient to prove or disprove the possibility that the striations are due to the relief of elastic stresses during the extraction process, or that they are a result of the extraction process itself.

4.3 Dimensional and Microstructural Stability

Three separate series of experiments were conducted to determine the dimensional and microstructural stability of the copper-silver and copper-niobium wires. The experiments included dilatometry to measure dimensional stability as well as isochronal anneals and draw-anneal-redraw sequences to test the microstructural stability of the wires.

4.3.1 Dilatometry

The dilatometry experiments were conducted to measure the dimensional stability of annealed and drawn copper as well as the drawn Cu-18wt%Nb and Cu-24wt%Ag wires. The results are plotted in Figure 4-8 on axes of specimen expansion versus temperature for all specimens tested. The annealed copper specimen behaved as expected with a linear response to temperature on the heating and cooling cycles. The drawn copper and copper-silver wires exhibited curious behaviour in that they displayed a positive deviation from

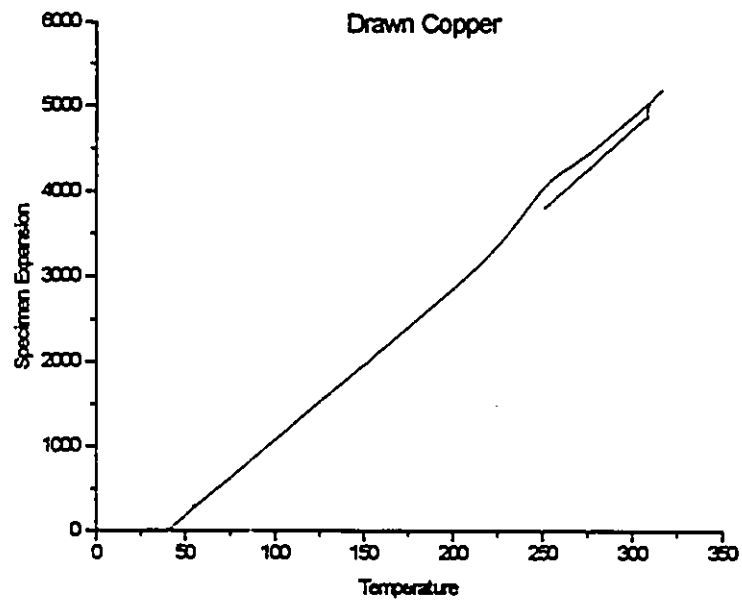
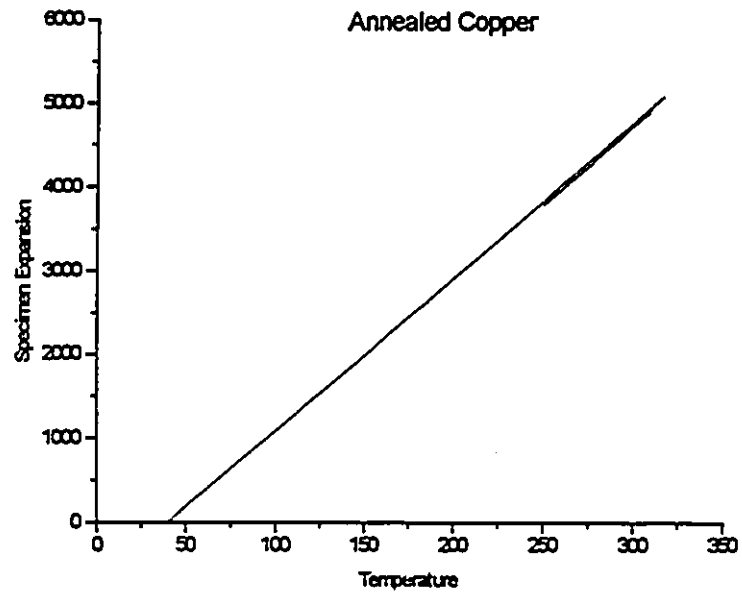


Figure 4-8 Expansion (in parts per million) versus temperature for a) annealed copper, b) drawn copper, c) drawn copper-silver, and d) drawn copper-niobium.

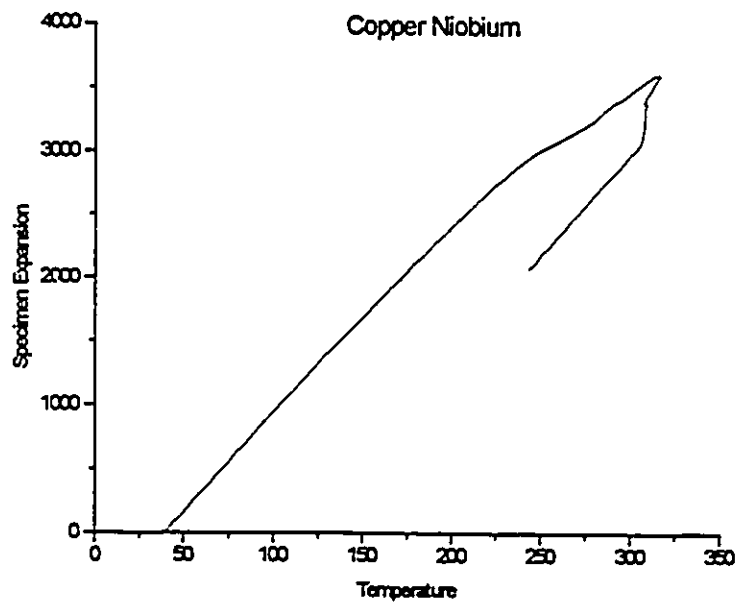
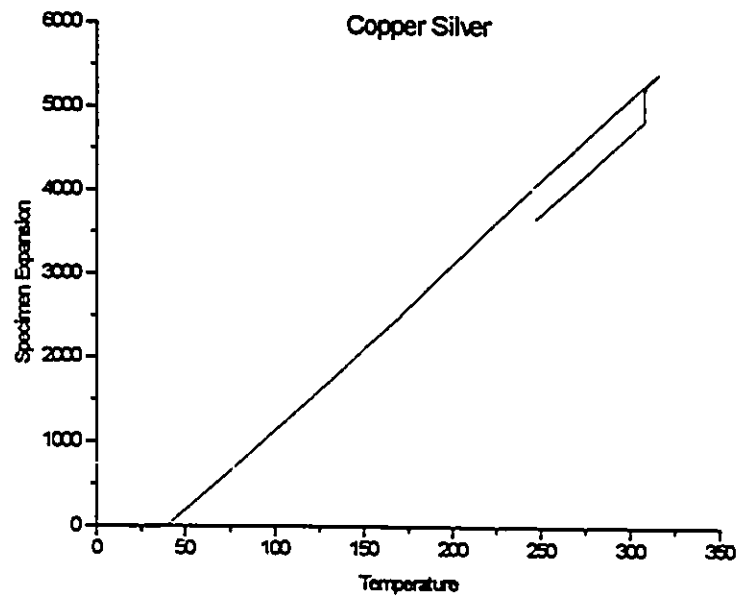


Figure 4-8 (continued) Expansion (in parts per million) versus temperature for c) drawn copper-silver and d) drawn copper-niobium.

linear behaviour. The departure from the linear relationship occurred, in both cases, in the range 200–250°C although the deviation was more marked in the case of the drawn copper. Also in both cases, the specimens exhibited creep behaviour over the 6 hour annealing period at 300°C. The creep did not occur in the annealed copper sample which indicates that the effect was not due to the finite load applied by the dilatometer. It is also interesting that the creep deformation in the drawn copper was equal in magnitude to the increased elongation during the heating ramp. (i.e. if the cooling curve is extrapolated back to room temperature, the heating and cooling curves are found to be collinear.) The copper-silver wire had a net decrease in length of approximately 0.03% measured by the difference between the extrapolated initial heating curve and the cooling curve.

The copper-niobium wire exhibited a significant, negative deviation from linearity, which also began between 200-250°C on the heating ramp. The wire continued to creep during the annealing period and displayed a permanent shortening of 0.1%. This behaviour is consistent with the relaxation of residual tensile stress in the niobium when the copper matrix begins to recover. The 0.1% decrease in length corresponds to relieving an elastic stress of approximately 100 MPa.

4.3.2 Isochronal Annealing

In order to measure the microstructural stability, a series of one hour annealing experiments were conducted over a range of temperatures. Changes in the microstructure were observed using transmission electron microscopy. Changes in the Cu-15wt%Nb microstructure were not observed after annealing below 300°C. At temperatures above

300°C, the niobium filaments began to spheroidize, and at 500°C, the niobium had completely spheroidized.

The microstructure of the Cu-24wt%Ag wires began to decompose by two processes between 200–300°C. The silver filaments were found, in some cases, to spheroidize in the same manner as the copper-niobium, however, the majority of the reactions involved the recrystallization of the copper and redistribution of the silver as either large precipitates on the recrystallized boundary, but more often as lamellar, discontinuous precipitates behind the advancing boundary. Examples of these three reactions are shown in the micrographs of Figure 4-9.

4.3.3 Intermediate Annealing Treatments

A series of draw-anneal-redraw experiments were conducted at McMaster and Los Alamos in an effort to duplicate the data of Sakai et al. (1992). After each step in the sequence described in Chapter 3, hardness measurements and TEM observations were made. It was found that the primary effect of the intermediate annealing (1 hour at 450°C) was to transform a significant fraction of the aligned, drawn structure into a coarser, misaligned structure by discontinuous precipitation as shown in Figure 4-9 c). At this point, however, the reproducibility of the degree to which the drawn microstructure is converted is in question. In the experiments conducted at Los Alamos, roughly one half of the microstructure was reprecipitated as discontinuous lamellae. The experiments conducted at McMaster converted essentially 100% of the microstructure by the discontinuous precipitation reaction. While both sets of experiments employed nominally identical temperatures

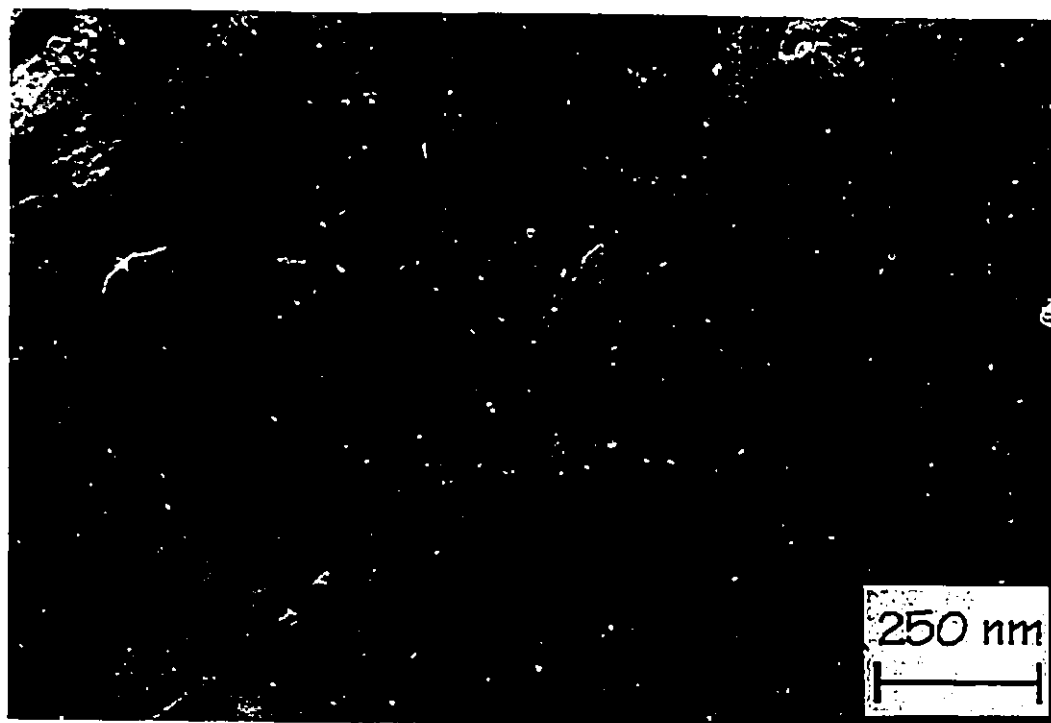


Figure 4-9 Examples of microstructural instability in annealed copper-silver wires. a) spheroidization, b) reprecipitation, and c) discontinuous coarsening.

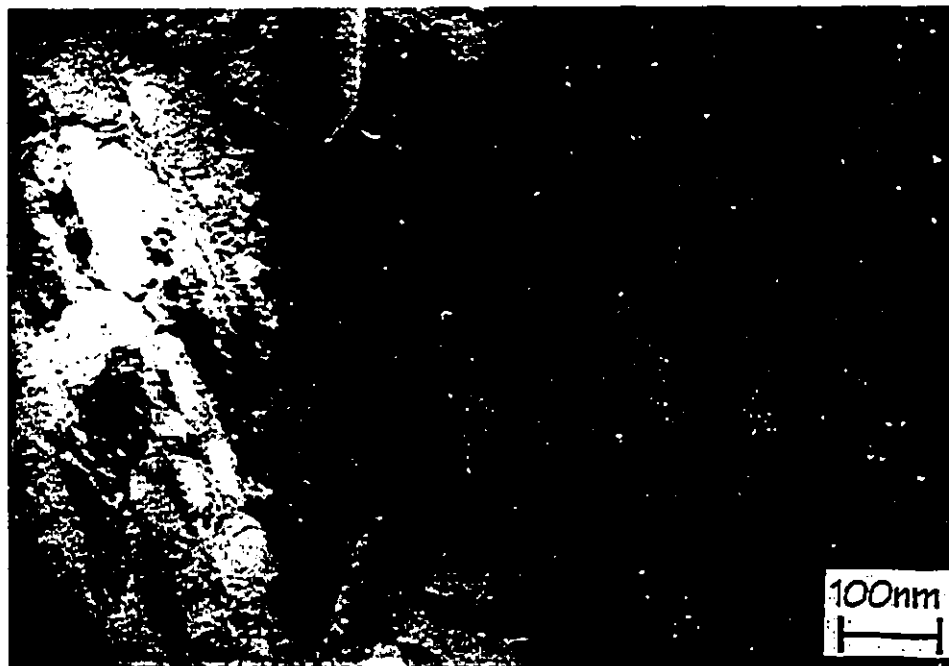


Figure 4-9 (continued) Discontinuous coarsening of the annealed copper-silver wire.

Table 4-1 Vickers hardness data from current experiments and literature for copper-silver wires subjected to intermediate heat treatments.

Condition	VHN	
	Experimental	Sakai et al. (1992)
As-cast	71 +/- 11.1	85
40% R.A.	152 +/- 9.6	169
40% R.A. + 1 H.T.	178 +/- 8.6	173
75% R.A.	174 +/- 3.6	178
40% R.A. + 1 H.T. + 35% R.A.	160 +/- 17.7	220
40% R.A. + 1 H.T. + 35% R.A. + 1 H.T.	134 +/- 5.0	215

and times, possible variations in heating and cooling times (e.g. quench versus air cooling) could be the source of the differing results.

The hardness data is presented in Table 4-1 as the mean value of eight measurements and the sample standard deviation. The original data of Sakai et al. (1992) is also presented for comparison. The general trend is for the increase in hardness with strain, however, there are a number of additional points to be considered. It was observed, particularly in the samples subjected to higher strains with intermediate heat treatments, that there were large differences in hardness (approximately 40 kg/mm^2) on different regions of the same sample which gives rise to large standard deviations in the measured hardness. It is also curious that in the sample reduced by 40%, the hardness increased after the annealing treatment. It is clear that these tests should be repeated on sufficient quantities of material to conduct tensile tests rather than relying on hardness data alone.

4.4 Mechanical Testing

A significant body of mechanical property data exists in the literature on the Cu-X composite materials. The aim of the few mechanical tests performed here was to address some specific points which can not necessarily be answered by literature data.

The analysis of tensile data on these heavily drawn, composite materials presents complications not always found in common engineering materials. The shape of the tensile stress-strain curve in these heavily drawn, two-phase wires make the analysis of yield-point phenomena difficult. The pronounced rounding of the elastic-plastic transition makes data such as the 0.2% offset yield point much less meaningful without a more detailed description

of the yielding behaviour. Therefore, for each tensile test completed at McMaster, careful measurements of 0.05, 0.10, 0.15, and 0.2% offset yield points were made.

For each stress-strain curve, the Young's modulus was determined by linear regression analysis of the elastic portion of the curve. The number of data points collected during the test allowed for a statistical accuracy of better than ± 1 GPa. The determination of offset yield points was made by fitting the yield portion of the curve with a polynomial function of the order required to get a correlation of better than 99.99%. The results of tests on the as-drawn materials are shown in Figure 4-10 a) and b) for the copper-silver and copper-niobium wires respectively.

The rounding of the yield point in the two materials is very pronounced in both cases. The 0.2% offset yield is greater than the 0.05% offset by 200 MPa for the Cu-Nb wire and almost 300 MPa for the Cu-Ag wire. This behaviour is generally attributed to the presence of residual stress in the material prior to testing. The presence of Bauschinger loops in the copper-niobium load-unload-reload cycles is further evidence of residual elastic stresses. These loops, however, are not seen in the copper-silver case. On reloading after unloading, the yield point is considerably sharper.

A second set of tests was performed on both the copper-silver and copper-niobium wires after heat treating for one hour at 250°C. This temperature was chosen after dilatometry and isochronal annealing observations to be high enough to allow for the relief of elastic stresses and yet low enough to prevent spheroidization. In the recovered condition, however, the curves of Figure 4-10 a) and b) show that the elastic-plastic transition is still gradual for both materials. The variation between the 0.05% and 0.15% offset values for copper-niobium has remained essentially unchanged, however, the variation in the copper-

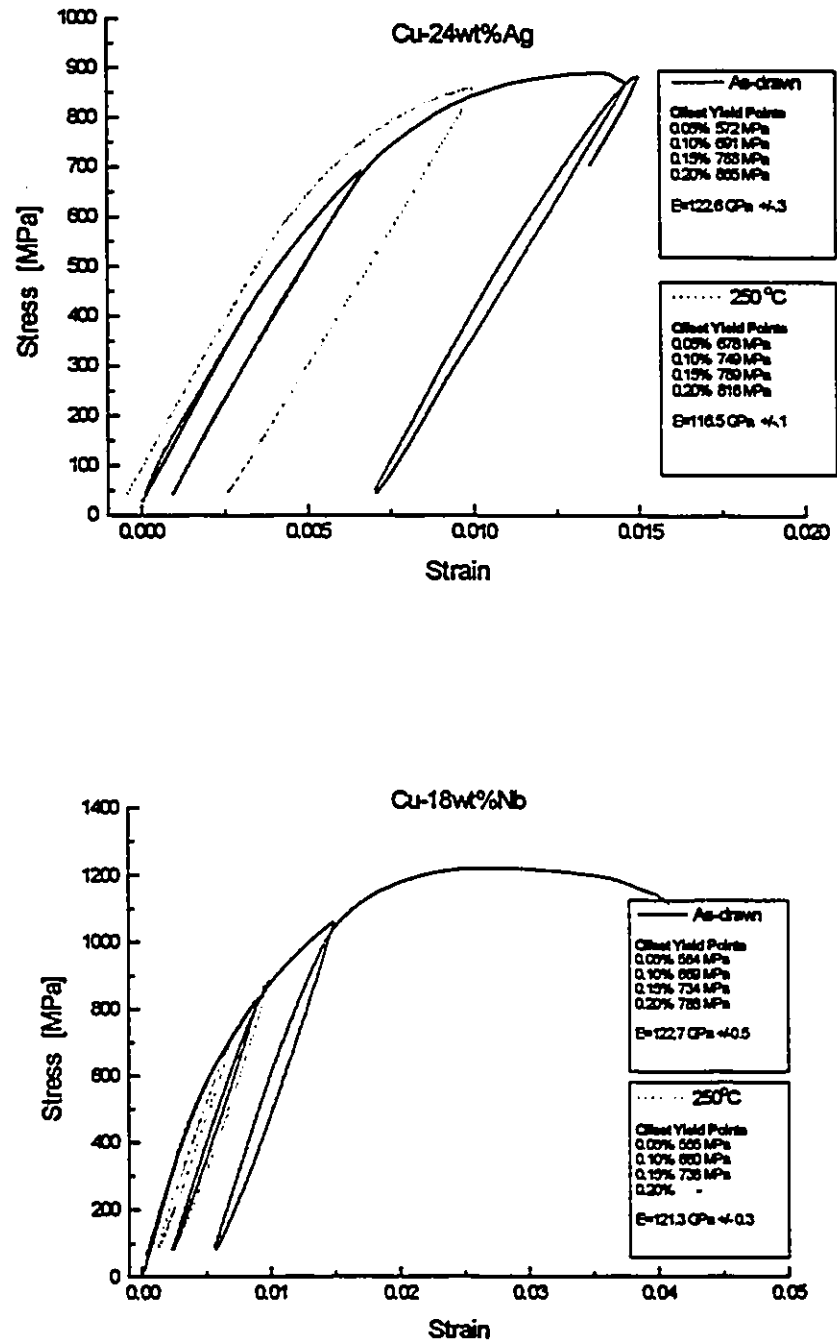


Figure 4-10 Tensile data for Cu-24wt%Ag and Cu-18wt%Nb in the as-drawn condition, and after recovery at 250°C for one hour.

Table 4-2 Tensile data for Cu-18wt%Nb measured at Los Alamos National Laboratory.

	Temperature		
	R. T.	195 K	77 K
Young's Modulus	111 +/- 4	118 +/- 2	116 +/- 11
0.2% Offset Yield	905 +/- 86	1021 +/- 35	1068 +/- 6
Ultimate Strength	1051 +/- 64	1167 +/-7	1268 +/- 13
Elong. to Failure	5.2 +/- 1.8	6.1 +/-1.3	6.6 +/- 1.1

silver wire between 0.05% and 0.2% offset has decreased to 140 MPa. A pronounced Bauschinger loop is still present in the copper-niobium data.

Tensile tests were also performed at Los Alamos National Laboratory on the identical copper-niobium wire at room temperature, 195K, and 77K. In this case, however, the data was presented only as 0.2% offset yield, ultimate strength and Young's Modulus. This data is presented in Table 4-2. The data for tests conducted at liquid nitrogen temperature are higher than both the Los Alamos and the current experimental data for room temperature. The reported room temperature data from the tests at Los Alamos, however, is also significantly higher than the current values. The most consistent approach to comparing the 77K tensile data to the test data from McMaster is to consider only the relative increase in strength over the similarly tested room temperature specimens.

4.5 Resistivity

Electrical resistivity was measured as a function of strain and temperature for three materials: i) pure copper, ii) Cu-1wt%Nb, and fullay annealed and redrawn Cu-24wt%Ag. The results are presented here in two ways. The resistivity is plotted as a function of temperature for each strain level and material in Figures 4-11, 12, 13 to show the general increase in resistivity with temperature.

In Figure 4-14, the low temperature plateau value of resistivity is plotted as a function of strain. These curves illustrate the effect of resistive mechanisms other than phonon scattering, and show the increase in resistivity with imposed strain in each material, as well as the increase in resistivity with increasing second phase volume fraction.

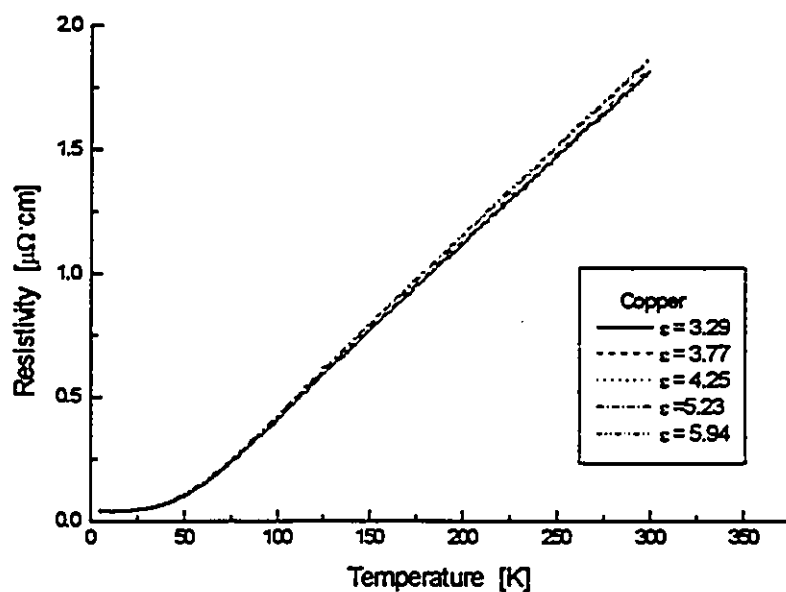


Figure 4-11 Resistivity versus temperature and strain in drawn, pure copper.

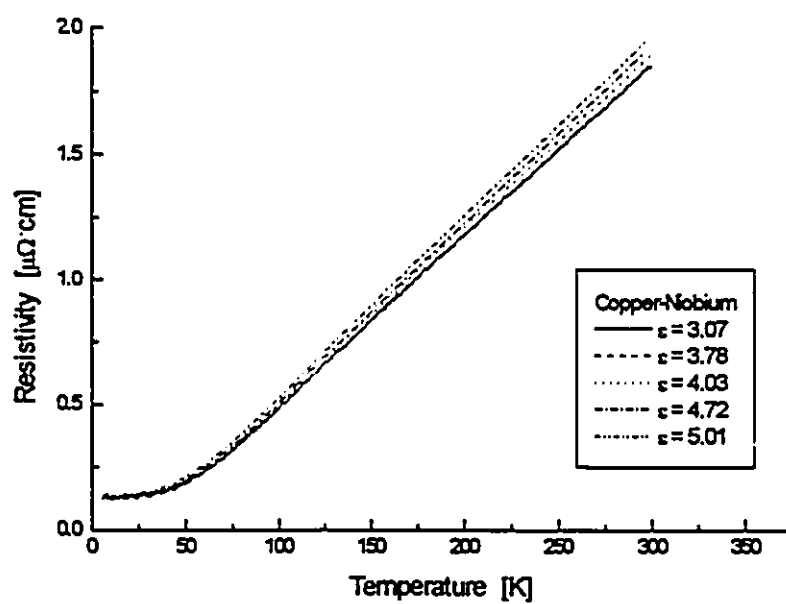


Figure 4-12 Resistivity versus temperature and strain for drawn Cu-1wt% Nb.

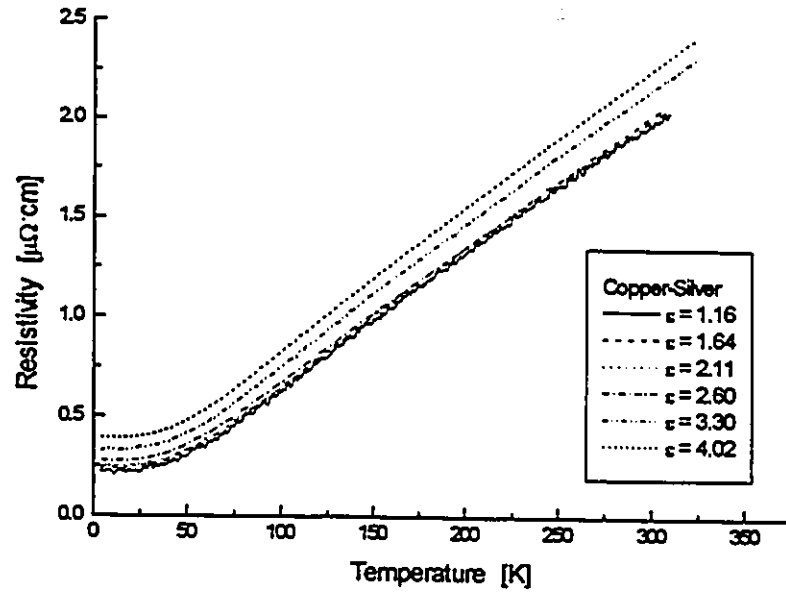


Figure 4-13 Resistivity versus temperature and strain for drawn Cu-24wt%Ag.

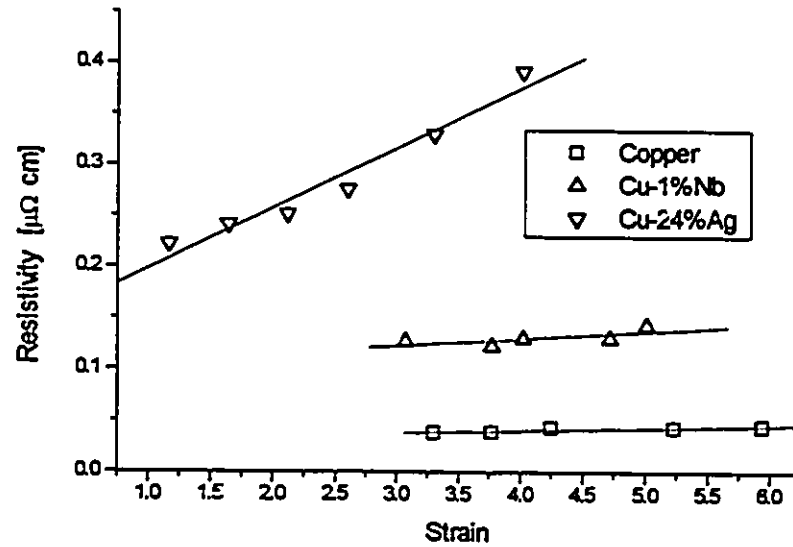


Figure 4-14 The low temperature (<10K) resistivity plateau for Cu, Cu-1wt%Nb, and Cu-24wt%Ag as a function of strain.

5. Discussion

This chapter will consider codeformation and strengthening, microstructural stability, and the evolution of electrical resistivity of two-phase alloys after large plastic deformation in light of the experimental results presented in Chapter 4 and the existing data from the literature.

5.1 The Codeformation and Strengthening of Two-Phase Alloys

The codeformation and strengthening of high-strength, two-phase wires is a very complicated subject. It has already been mentioned (Embury, 1992) that it is unlikely that one mechanism is responsible for the strengthening over the range of strains 0 to 10 found in these materials. It is also true that direct evidence to confirm or refute the operation of all of the possible mechanisms at each level of strain is not presently available. It is the purpose of this section of the discussion to bring together the observations of current experiments as well as those from the literature to form a clearer picture of the evolution of the strength of these materials and to point out those areas which need further investigation.

The observations discussed in Chapter 4 regarding the evolution of the microstructure of copper-silver and copper-niobium composites suggest that it is appropriate to divide the discussion of the codeformation and strengthening of these materials into a series of stages. While the transition from one stage to another is not necessarily well defined, the

stages may be generally described as first the alignment of the second phase followed by scale-dependent stages of refinement. The various refinement stages represent the regimes over which different hardening mechanisms appear to be dominant.

5.1.1 Starting Materials

Any investigation into the evolution of strength and microstructure requires a well defined starting point. In all cases, the starting microstructures are two-phase mixtures of the soft materials. The morphology of the copper-silver alloy is that of primary copper dendrites surrounded by regions of rod or lamellar eutectic. The copper-niobium alloys studied have an initial structure consisting of either primary niobium dendrites (for the higher volume fraction materials) or crystallographically faceted particles of niobium (for the Cu-1wt%Nb alloy). Typical dendrite arm diameters have been reported to be in the range of 1 to 10 μm (Spitzig et al., 1987; Verhoeven et al., 1989). The niobium particles of the low volume fraction alloy were found to be in the range 1 to 5 μm .

Data reported in the literature for the strength of the as-cast materials is generally reported as ultimate rather than yield strengths, and typical values are consistent with the strength of copper. For example, the data of Spitzig and Krotz (1987) is presented in Figure 5-1 and shows the ultimate strengths for two Cu-18wt%Nb alloys to be of the order of 250 MPa. The yield strength of the as-cast material should be described approximately by a rule-of-mixtures using data for the fully annealed constituents.

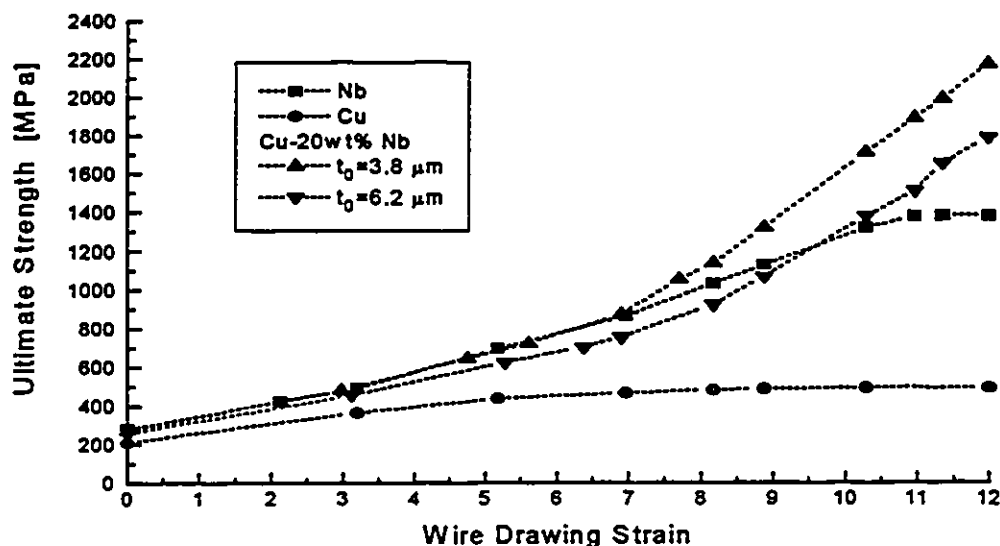


Figure 5-1 Experimental data of Spitzig and Krotz, (1987) for ultimate strengths of copper, niobium and two copper niobium composites.

5.1.2 Alignment

The first stage to be considered covers the range of strain required to align the second phase rods or plates with the drawing axis. Experimental evidence from a variety of systems (Cu-Nb, [Spitzig, et al., 1987ii]; Cu-Ag, [Sakai et al., 1991]; Fe-Fe₃C, [Embury and Fisher, 1966]) suggest that the second phase becomes aligned after imposed strains of the order of 1 to 1.5. Little attention has been given to this portion of the flow curve in the work on these high-strength materials because the high strengths are only attained after much larger deformations. In Section 5.2.2, however, arguments will be made to suggest that the hardening mechanisms involved in the alignment process can play a significant role in the processing of the copper-silver (and perhaps other) systems.

Within the alignment process are a number of events which contribute to the work hardening of the two-phase materials. The first aspect of the alignment stage is to describe the evolution of the geometry. In the simplest case, the second phase could be considered as a fiducial marker in the matrix which does not alter the flow in any way (i.e. it codeforms with the matrix at the same stress). This situation is shown in Figure 5-2. The progression in Figure 5-2 a) shows the geometric evolution in a rectangular piece of the material, the size and shape of which is determined by the initial misorientation of the second phase with the drawing axis, Θ_0 . If we consider the change in angle with respect to the deformation axis after a strain ϵ_i , the dimensions of the rectangle will have changed according to the relations:

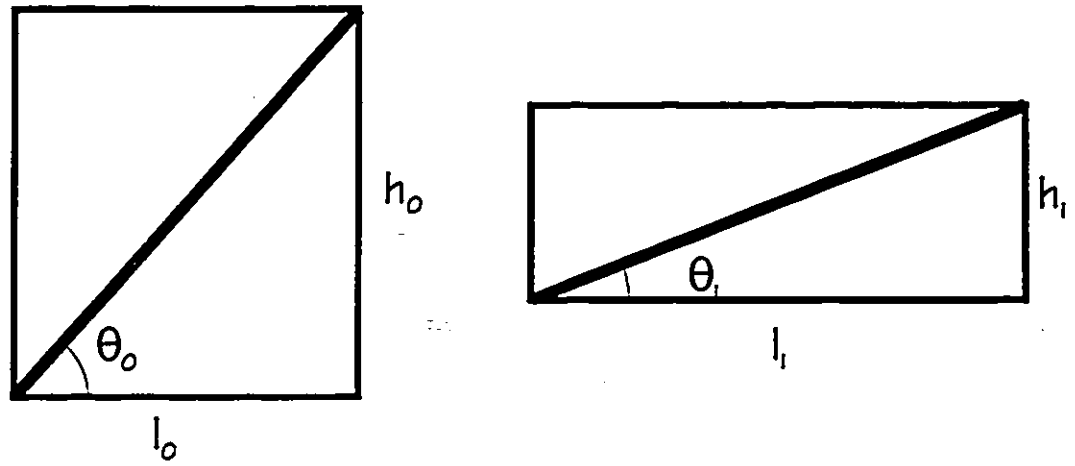
$$\begin{aligned} h_i &= \frac{h_0}{\exp(\epsilon_i/2)} \\ l_i &= l_0 \exp(\epsilon_i) \end{aligned} \quad (5.1)$$

The instantaneous angle of misorientation, Θ_i , may be calculated as a function of the initial misorientation and the imposed strain:

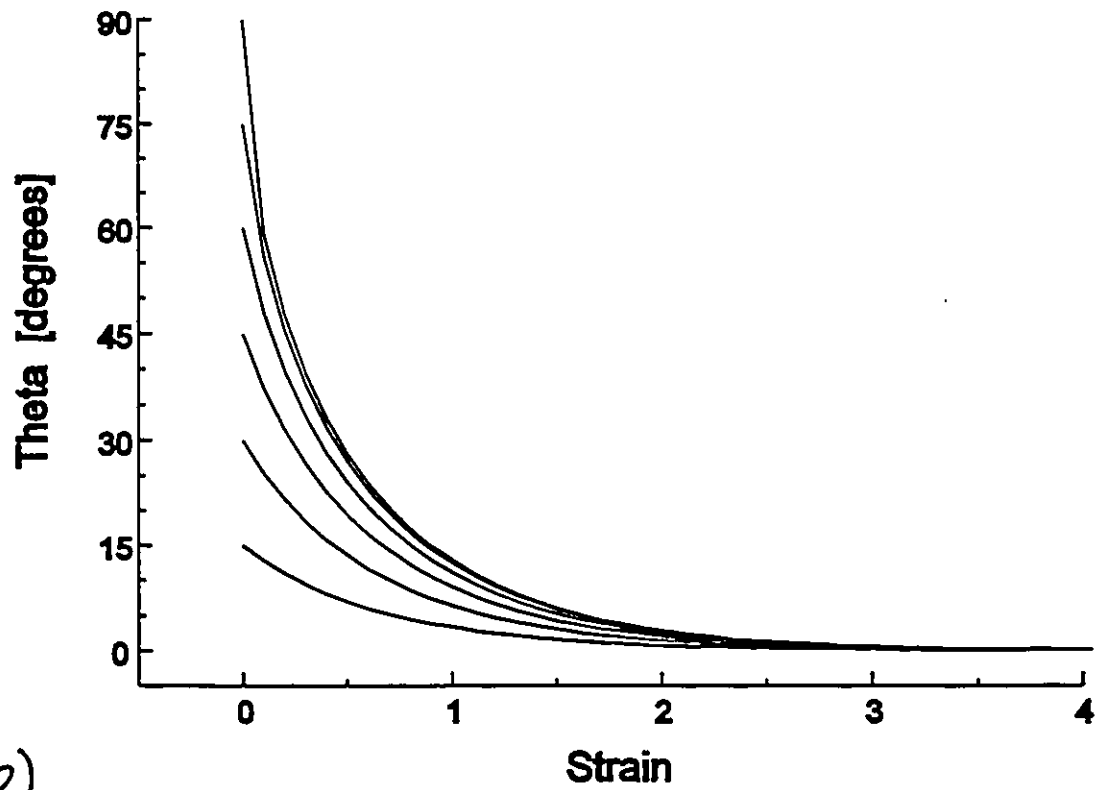
$$\begin{aligned} \Theta_i &= \sin^{-1} \left(\frac{h_i}{l_i} \right) \\ \Theta_i &= \sin^{-1} \left[\frac{\sin(\Theta_0)}{\exp(3\epsilon_i/2)} \right] \end{aligned} \quad (5.2)$$

This equation is plotted as a function of strain for various initial misorientations in Figure 5-2 b).

By employing the same assumptions regarding the deformation of the second phase, it is also possible to calculate the change in spacing of two, parallel fibres or plates with imposed strain. Figure 5-3 shows this process. Using the same initial rectangle from



a)



b)

Figure 5-2 The evolution of the misorientation angle, θ , with strain.

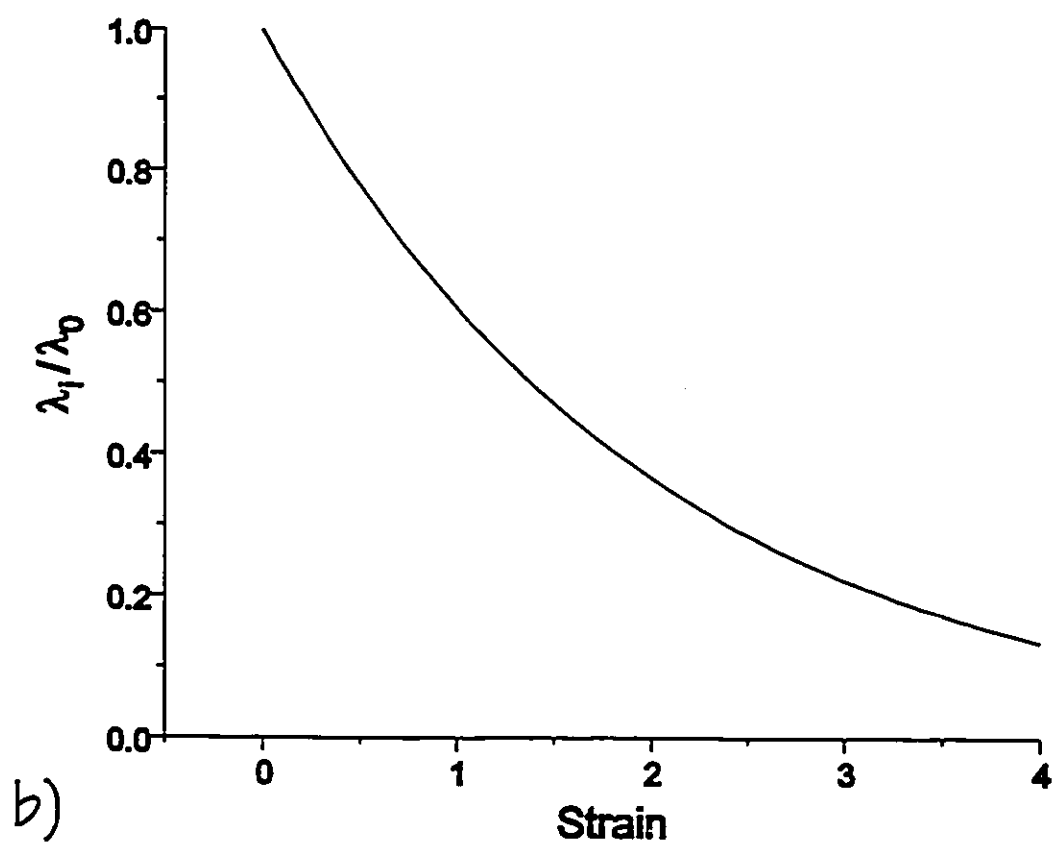
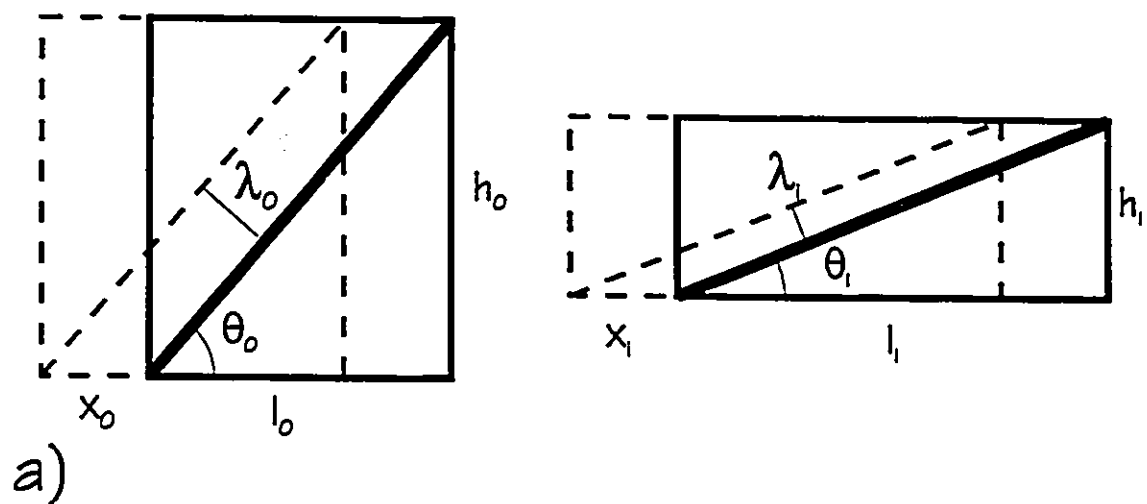


Figure 5-3 The evolution of interphase spacing with strain during the alignment process.

Figure 5-2, a second, similar rectangle has been superimposed with a horizontal offset of $x_0 = \lambda_0 / \sin(\theta_0)$. The value of the offset, x_i , will vary with strain as:

$$\begin{aligned} x_i &= x_0 \exp(\epsilon_i) \\ x_i &= \frac{\lambda_0}{\sin(\theta_0)} \exp(\epsilon_i) \end{aligned} \quad (5.3)$$

The interphase spacing can be calculated as a function of strain by combining Equations 5.2 and 5.3 as:

$$\begin{aligned} \lambda_i &= x_i \sin(\theta_i) \\ \lambda_i &= \frac{\lambda_0}{\sin(\theta_0)} \exp(\epsilon_i) \cdot \frac{\sin(\theta_0)}{\exp(\beta \epsilon_i / 2)} \\ \lambda_i &= \frac{\lambda_0}{\exp(\epsilon_i / 2)} \end{aligned} \quad (5.4)$$

The combination of Equations 5.2 and 5.4, as was mentioned at the outset, describe the geometric evolution for two co-deforming materials. If there is a difference in flow stress between the two phases, then deviations from this behaviour may be expected.

If the second phase limits the motion of dislocations, then the primary result of the alignment process will be the decrease in the average slip line length. Figure 5-4 illustrates this effect. The average slip line length is determined by the minimum length of two lines drawn at 45° to the drawing axis and bounded by two second phase plates or rods. From the geometry shown in Figure 5-4, the average slip line length is given by:

$$\bar{d} = \frac{\lambda}{\cos(\theta - 45^\circ)} \quad (5.5)$$

With the appropriate substitutions from Equations 5.2 and 5.4, the average slip line length is given by:

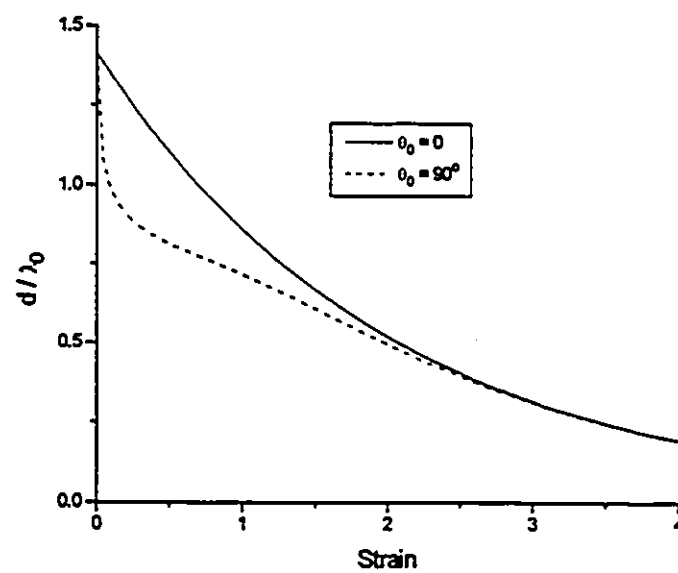
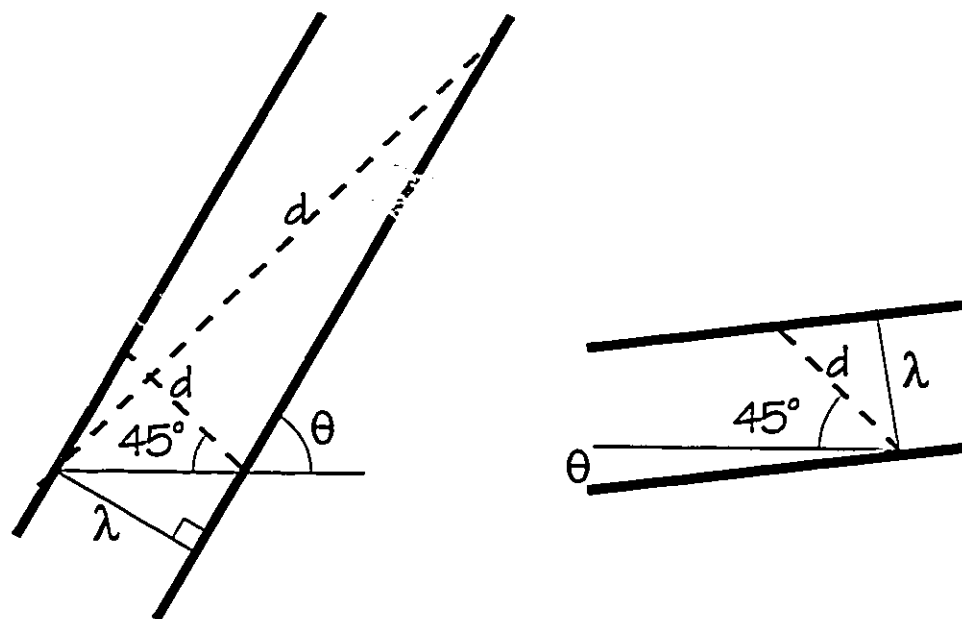


Figure 5-4 The change in mean slip line length with strain for various initial misorientation angles.

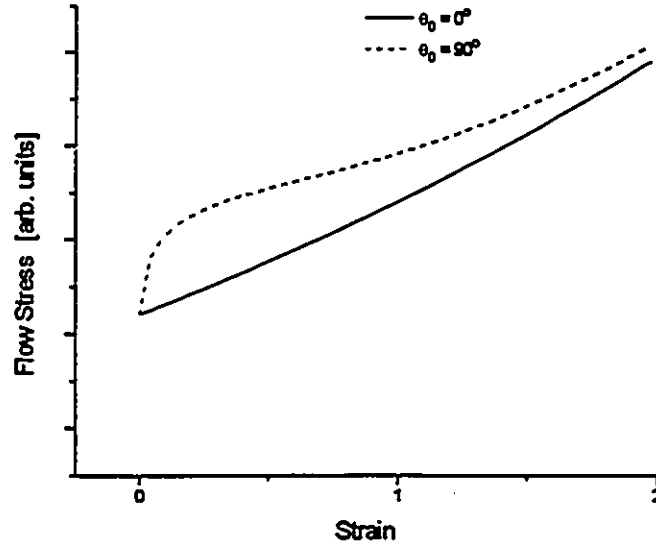


Figure 5-5 The shape of the flow curve predicted during the alignment phase by an inverse square root relationship.

$$\bar{d} = \frac{\lambda_0}{\exp(\epsilon/2) \cos \left[\sin^{-1} \left(\frac{\sin(\theta_0)}{\exp(3\epsilon/2)} \right) - 45^\circ \right]} \quad (5.6)$$

Equation 5.6 is plotted in Figure 5-4 showing the extreme cases of aligned and perpendicular second phases. The curves show that the slip line length decreases more rapidly than the interphase spacing or the misalignment angle. The general result that the flow stress is proportional to the inverse square root of the slip line length (i.e. the Hall-Petch formulation), leads to the expectation that a misaligned structure will have an initially very high hardening rate depending on the degree of misorientation. The general shape of the flow curve predicted by an inverse square root relationship is shown in Figure 5-5. Based on the contribution of the slip line length, it is expected that the alignment phase will begin with an initially high work hardening rate followed by a much lower rate once the second phase becomes parallel to the deformation axis.

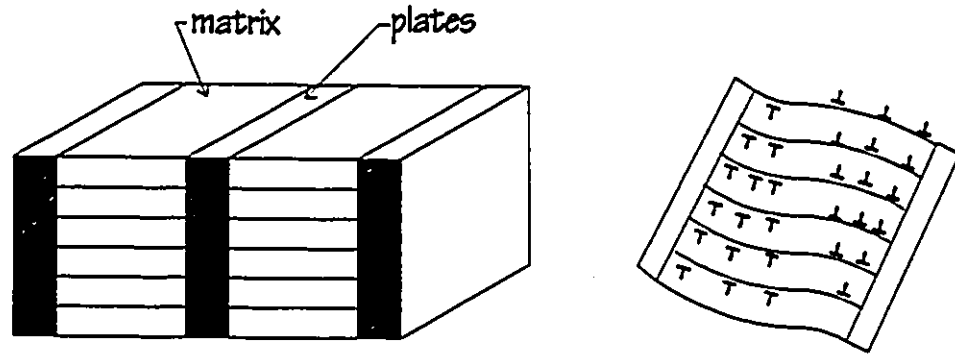


Figure 5-6 The generation of geometrically necessary dislocations to accomodate the curvature due to a non-deforming second phase. (from Ashby, 1971)

If the second phase is impenetrable to dislocations, then the alignment process is also precisely the situation described by Ashby (1971) for the generation of geometrically necessary dislocations. Figure 5-6 shows schematically how the lattice of the matrix is forced to bend to accomodate the rotation of a non-deforming second phase. The density of geometrically necessary dislocations generated for a given strain is given by Equation 2.22:

$$n^G = \frac{c \gamma}{b \lambda^G} \quad (5.7)$$

where c is a constant equal to 2 for one dimensional and 4 for two-dimensional constraints.

For a rod morphology, the geometric slip distance, λ^G is given by:

$$\lambda^G = \frac{r}{f} \quad (5.8)$$

where r is the radius and f is the volume fraction of the second phase.

During the early stages of deformation, the two phases have roughly the same flow stress. This would suggest that deformation of the second phase would occur and, therefore, fewer geometrically necessary dislocations would be generated than is predicted by Equation 2.22. This effectively amounts to choosing a lower value for the constant, c .

The increase in strength due to the generated dislocations is given by:

$$\begin{aligned}\Delta\tau &= \alpha \mu b \sqrt{n} \\ \Delta\tau &= \alpha \mu b \sqrt{\frac{c\gamma}{b\lambda G}}\end{aligned}\tag{5.9}$$

where γ is the shear strain. The contribution to the hardening rate is, therefore:

$$\frac{d\tau}{d\gamma} = \alpha \mu \sqrt{\frac{b c}{\gamma \lambda G}}\tag{5.10}$$

For an initial spacing of 1 μm , the hardening rate would be of the order:

$$\frac{d\tau}{d\gamma} = \frac{\mu}{2000 \gamma^{1/2}}\tag{5.11}$$

This suggests that, during the early stages of alignment, the hardening rate should be very high (of the order $\mu/200$), falling off as the strain increases. In the limit of very low strains, Equation 5.11 would predict an infinite hardening rate. In actuality, the measured hardening rate must have an upper limit set by the elastic modulus of the second phase multiplied by the volume fraction. That is, if:

$$\sigma = \sigma_f V_f + \sigma_m (1 - V_f)$$

then when the matrix begins to yield:

$$\frac{d\sigma}{d\varepsilon} = E_f V_f + \frac{d\sigma_m}{d\varepsilon} (1 - V_f)$$

The first term in this equation will always dominate.

The third factor to consider in the process of microstructural alignment is that of the evolution of texture in the material. Although the development of texture in two-phase materials is generally observed to be slower than in the pure matrix, it will develop so as to align the primary slip systems into the most favourable position to accommodate the imposed strain. In a material that had no other hardening mechanism – an elastic-perfectly plastic material – the net effect of the texture development will be a slight decrease in the hardening rate, although this effect would be small compared to the mechanisms discussed previously.

During the alignment phase, predictions of strengthening based on both changes in slip line length and the generation of geometrically necessary dislocations predict that this process leads to a very high work hardening rate compared to that of an aligned structure. This result will be important in the discussion of the effects of intermediate heat treatments on copper-silver alloys in Section 5.2.2.

5.1.3 Refinement

The bulk of the work on heavily deformed, two-phase materials has been focussed on attempting to understand what is responsible for their strength after large imposed strains. It is this very broad range of strain following microstructural alignment which can be termed the refinement stage. The bulk of the debate over which mechanisms are operating during this stage is summarized in the series of articles and replies by Funkenbusch and Courtney (1989, 1990a, b) and Spitzig et al. (1990a, b). Before continuing with this section, it is worthwhile to recall some of the significant points of these arguments in light of various pieces of experimental evidence.

The central issue of the debate is whether the refinement of microstructural scale by cold deformation forces the increased generation and storage of dislocations (substructural strengthening, Funkenbusch and Courtney) or whether it strengthens the material by decreasing the spacing of the obstacles to dislocation motion (barrier strengthening, Spitzig et al.).

To be efficient, the generation of geometrically necessary dislocations requires hard second phase particles and large strain gradients. The scale of the second phase must also be large enough so that the strain gradient is not relieved by short-range diffusion processes. TEM evidence for large strain gradients such as that observed by Ashby and Russell (1971) in the aluminum-copper system is not apparent in the micrographs of the copper-niobium and copper-silver systems. Also, as will be discussed in more detail later in this section, the widespread observations of extensive co-deformation of the niobium and silver filaments suggest that they do not act as “hard” particles. Finally, the most compelling evidence against the substructural hardening proposition is the absence of large dislocation densities at large plastic strains. In fact, the observations suggest that dislocations are being removed from the system at large strains. Interestingly, Funkenbusch and Courtney suggest that, contrary to the assertions of Spitzig et al., their model requires dislocation densities of the order of $10^{15} - 10^{16} \text{ m}^{-2}$ in the copper are sufficient to explain the strength of the composite. Simple calculations based on the equation $\sigma = \alpha \mu b \sqrt{\rho}$, however, give strength estimates of the order of 200 MPa. To reach composite strengths in excess of 1 GPa would require considerably higher inherent strength from the matrix.

When the second phase has become aligned with the wire axis, the mechanisms responsible for hardening the material during the alignment phase are no longer effective.

The rotation of the microstructure has ceased, eliminating the generation of geometrically necessary dislocations and significantly decreasing the rate of change of the slip line length. The observations that, in both the copper-niobium and copper-silver cases, the second phase remains continuous to very large strains raises two questions. What mechanism(s) is (are) responsible for the continued hardening, and, how do the two phases sustain codeformation?

It is possible to examine these two-phase systems from two perspectives. The first, and simplest, approach is to treat the materials in a quasi-continuous fashion in which a rule-of-mixtures relationship will model the strengthening. The second approach arises from examining the co-deformation process which leads to certain conclusions regarding the nature of the dislocation motion in these systems. For simplicity in both cases, let us assume that, at the start of the refinement stage, the microstructure consists of aligned, stress-free, single crystal, second-phase rods surrounded by a continuous matrix of single crystal copper. The primary assumption being the second-phase shape as the niobium will deform into a ribbon, rather than a rod-like shape. Due to their similar crystal structures, the silver filaments in the copper-silver wires maintain their cylindrical shape.

5.1.3.1 Continuum Considerations

The two material combinations under consideration here are qualitatively different in that, while silver is an fcc material which, in the bulk, does not work harden more than the copper matrix, niobium is a bcc metal which can attain strengths of the order of 1 GPa after extensive cold working. Both the copper-silver and copper-niobium composites can attain strengths up to 2 GPa, which suggests that the work hardening of the second phase does not make a major contribution to the final strength of the wire.

At intermediate strains (between approximately 2 and 5 for the materials shown in Figure 5-1) the niobium work hardens to much higher strengths than the copper matrix. This will lead to the build up of elastic tensile stresses in the niobium and compressive stresses in the copper matrix. The series of extracted niobium filaments in Figure 5-7 show direct evidence of these elastic stresses. Filaments from wires drawn to a strain of 3 are elongated as expected and remain straight after extraction. The filaments extracted after drawing to strains of 4 and 5 show increasing degrees of curling. If, however, the wire drawn to a strain of 5 was annealed at 500°C for one hour, the extracted filaments are straight, indicating that they are free of residual elastic stresses. From simple beam theory, the stress required to bend the filament to a given radius (or to straighten a bent filament) is given by:

$$\sigma = \frac{-Ey}{r} \quad (5.12)$$

where E is the Young's modulus, y is the distance from the neutral axis and r is the radius of curvature. Measuring average thicknesses and radii from Figure 5-7 c) and substituting into Equation 5.12 yields values of elastic stress of the order of $E/20$. While this is certainly a very rough estimate of the actual residual stress, it does indicate that the niobium filaments are reaching strengths that are approaching the theoretical limits.

Knowing now that the drawn niobium filaments are supporting stresses approaching the theoretical limit, it is of interest to investigate how this is accomplished. Examination of the extracted niobium filaments by transmission electron microscopy reveal them to be essentially dislocation free. This suggests that it is not unreasonable to consider the material in terms of a copper matrix strengthened by niobium whiskers. This concept is in accord with the original proposition of Bevk et al. (1978) to treat the strength as a rule-of mixtures based on the theoretical strengths of the constituent materials.

a) $\epsilon=3$ b) $\epsilon=4$

Figure S-7 Extracted niobium filaments after various strains and heat treatments. a) $\epsilon=3$, b) $\epsilon=4$, c) $\epsilon=5$, d) $\epsilon=5$ extracted after annealing for one hour at 500°C .



c) $\epsilon=5$



d) $\epsilon=5$, 500°C for 1hr

Figure 5-7 (continued) Extracted niobium filaments.

The concept of whisker reinforcement is worth further consideration to examine the relative contributions of matrix and second phase. Funkenbusch and Courtney (1989) said that substructural strengthening did not rely on the inherent strength of the matrix for the overall strength of the composite, and thus the relatively low observed dislocation densities were not in contradiction with their model. If we continue to consider the case of the Cu-20wt%Nb (21vol%) data of Spitzig and Krotz (1987), and take the approach that the wire strength may be calculated as a rule-of-mixtures with the theoretically strong second phase, it is possible to calculate the contribution that must be made by the copper matrix.

Assuming:

$$\sigma_{Nb} = \frac{E_{Nb}}{65} \approx 1600 \text{ MPa}$$

$$V_{Nb} = 0.21$$

$$\sigma_{Cu} = \frac{\sigma_{wire} - 330}{0.79} \text{ [MPa]}$$

From Figure 5-1, after a strain of 5, the matrix must “contribute” a strength of roughly 350 MPa. After strains of 10 or 11, however, the required strength is of the order of 1 GPa. If the two-phase wires may be treated as continua, then the experimental data requires that the matrix, as well as the second phase, approach its theoretical strength.

Before leaving the continuum approach, it is worth looking further into the role of the elastic stresses as a method of strengthening. In “conventional” fibre composites, at least part of their enhanced strength is due to the load transfer to a stiffer second phase. Due to prior deformation or differences in thermal expansion coefficients, the reinforcing phase carries residual tensile stress while the weaker phase is held in compression. The increase in the tensile yield point in these materials is a result of having to relieve the residual

compressive stress before placing the matrix in tension. If the same mechanism is operative in the copper-niobium and copper-silver systems, then tensile tests of samples in the as-drawn and stress-relieved conditions should exhibit yield points which differ by an amount of the order of the magnitude of the residual stress multiplied by the volume fraction of the second phase.

Tensile tests were performed on Cu-24wt%Ag and Cu-18%Nb in the as-drawn condition and after annealing at 250°C for one hour. The magnitude of the residual stress in the copper-silver case is not known, however, the niobium filaments (by their curvature) have residual stresses of at least 1 GPa. If this strengthening mechanism were operating, a yield point drop of the order of 200 MPa would be expected for these volume fractions. The 0.05% offset yield point of the copper-niobium wires showed a decrease of approximately 30 MPa. Yield points measured at 0.1% and 0.15% offset differed by less than 10 MPa.

It is important to note here that the interpretation of data by the approach outlined above requires great care in the determination of the yield point. Materials with large elastic stresses generally do not have a sharp yield point and, therefore, using a 0.2% offset yield point will typically not capture the true behaviour of the material. This point is illustrated by the 200 MPa difference in yield point measured by 0.05% and 0.2% offset methods respectively.

5.1.3.2 Scale-Dependent Considerations

In considering the scale dependence of the flow stress, there are essentially two cases to be examined. When the interphase spacing is large compared to the mean slip distance of a dislocation (in the early stages of refinement) dislocations will be stored in the matrix

and a dislocation substructure will develop. This is the case described in Chapter 2 for which the statistical slip distance is less than the geometric slip distance. As deformation continues, however, the scale of the microstructure will reach a point at which dislocation may only be stored in the interface.

If we now consider the refinement stage from a detailed, geometric point of view, a series of new observations may be made. The basic premise that these two-phase wires deform by slip leads to the conclusion that dislocations must traverse the structure and, therefore, must overcome the barriers presented by the second phase. Because the morphology of the second phase precludes the dislocations climbing to avoid the obstacles, there are only two possibilities. The second phase may act as a "hard" constituent, in which case the dislocation will bow between and eventually leave loops around the obstacles, or, they will be "soft" and, therefore, cut by the dislocation after it has bowed through some angle less than 90° .

The question as to whether the second phase behaves as a hard or soft obstacle is answered by the response to deformation. If it behaved as a hard obstacle, there would be no co-deformation of the two phases and there would be microstructural evidence of particle fracture. The fact that the two-phases continue to co-deform to the highest observed strains indicates that the second phase does behave as a shearable obstacle.

It is interesting now, to explore the implications of treating the second phase as a soft obstacle. The obvious place to start is to examine the relationship governing the strength of such a material. This relationship is discussed in the review by Brown and Ham (1971), and is given by:

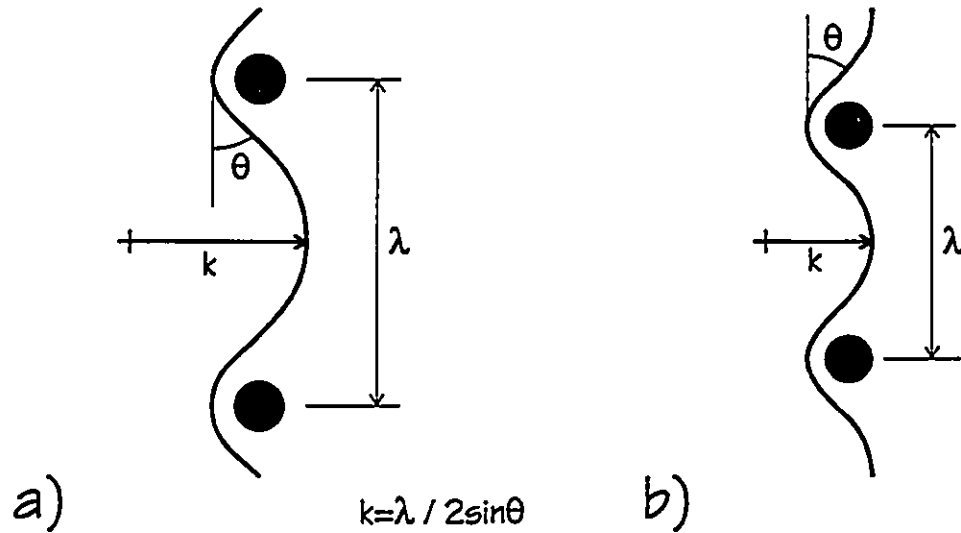


Figure 5-8 Schematic diagram of a dislocation bowing through obstacles of different spacings.

$$\tau = \frac{2 (\gamma b)^{3/2}}{b \lambda \left(\frac{\mu b^2}{2} \right)^{1/2}} \quad (5.13)$$

$$\tau = \frac{2 \gamma^{3/2}}{\lambda \left(\frac{\mu b}{2} \right)^{1/2}}$$

where γ is the surface energy of the particle and λ is the spacing. Equation 5.13 reflects the forces involved in overcoming the obstacle. The particle exerts a force on the dislocation equal to the interface surface energy multiplied by the amount of new surface generated ($2\gamma b$). The inverse relationship between the flow stress and the particle spacing is best described by the diagrams in Figure 5-8. The force exerted on the particle by the dislocation is given by the line tension ($\mu b^2/2$) multiplied by the sine of the angle (θ) through which it

has bent. The applied stress required to bend a dislocation to a prescribed radius, k , is given by:

$$\begin{aligned}\tau &= \frac{\mu b}{2k} \\ \tau &= \frac{\mu b \sin\theta}{\lambda}\end{aligned}\tag{5.14}$$

An obstacle of a given strength requires that the dislocation bend through a critical angle before it will be sheared. However, if the obstacles are closer together, then the dislocation must be bent to a smaller radius to achieve that critical angle and, therefore, the applied stress must be higher.

Equation 5.13 predicts that both the strength and the work hardening rate will increase exponentially with strain (λ decreases exponentially with strain). In order to apply this, however, it is necessary to set a practical limit on the minimum value for the interphase spacing. The extreme limit would be of the order of a few unit cells. Stability considerations, as will be discussed further in the Section 5.2, will determine a microstructural scale at which the diffusion distances are sufficiently small to allow spontaneous spheroidization. If we assume that the tensile strength is twice the shear strength, and estimate values of $\gamma = 0.5 \text{ J/m}^2$, $\mu = 47 \text{ GPa}$, $b = 1 \text{ Å}$ and set λ at 5 nm, then Equation 5.13 estimates the flow stress to be of the order of 200 MPa. This is far below the observed strength levels in the copper-niobium and copper-silver systems. For this reason, it is worthwhile to re-examine the force balance implied in Equation 5.13 in some detail.

From Equation 5.14, if the example material considered above is to have a tensile flow stress of 1 GPa, then the shear strength must reach approximately 500 MPa, and the second phase must be strong enough to force the dislocation to bend through an angle:

$$\theta = \sin^{-1} \left(\frac{\tau \lambda}{\mu b} \right)$$

$$\theta \approx 32^\circ$$

The force balance at the particle yields the expression:

$$2 \gamma b_{Nb} = \mu_{Cu} b_{Cu}^2 \sin(\theta) \quad (5.15)$$

Assuming the Burger's vectors are approximately equal in both phases, the critical angle required to shear the particle is:

$$\theta = \sin^{-1} \left(\frac{2 \gamma}{\mu_{Cu} b} \right)$$

$$\theta \approx 12^\circ$$

The critical angle predicted by the force balance is considerably less than that required to explain the observed strength. It is unlikely that the shear modulus or Burger vectors will change appreciably and, therefore, the only possibility for increasing the critical angle is an increase in the effective surface energy. To continue this example, if a critical angle of 32° is required to attain a tensile strength of 1 GPa, then the effective surface energy must be:

$$\gamma = \frac{\mu_{Cu} b \sin(\theta)}{2}$$

$$\gamma \approx 1.2 \text{ J/m}^2$$

or, roughly two to three times the equilibrium value.

Mechanisms responsible for increasing the effective surface energy have been discussed by a number of researchers. Embury and Hirth (1994), discussed the situation for lamellar structures of hard and soft phases, in which deformation effectively plates dislocations in the interface, storing elastic strain energy in the harder phase and increasing the surface energy by placing the interface under traction.

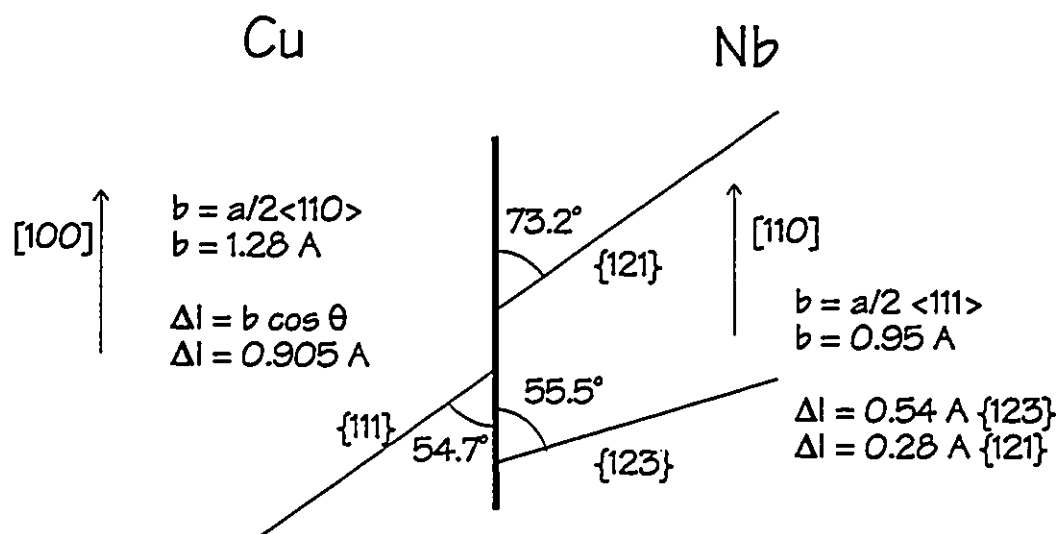


Figure 5-9 The difference in strain across an interface caused by unequal Burger's vectors.

For the case of a soft second phase, a detailed examination of the particle shearing process reveals an additional contribution to the stored energy. When a dislocation in the copper matrix shears a second phase particle, the resulting elongation of each phase is not equal due to the difference in the magnitude of the Burger's vector in each phase and the angle the slip plane makes with the wire axis. The difference in elongation will give rise to a build up of elastic stress in the two phases. One possible manifestation of this process is illustrated in Figure 5-9 for the case of copper and niobium assuming the experimentally measured textures and that both phases are deforming on their normal slip systems. The simple calculations shown in Figure 5-9 demonstrate that, if the second phase is cut by a single dislocation, the matrix will elongate an additional 0.37 Å compared to the second phase. If the second phase continues to be cut, the elastic strains will build until the stress exceeds the strength of the filament.

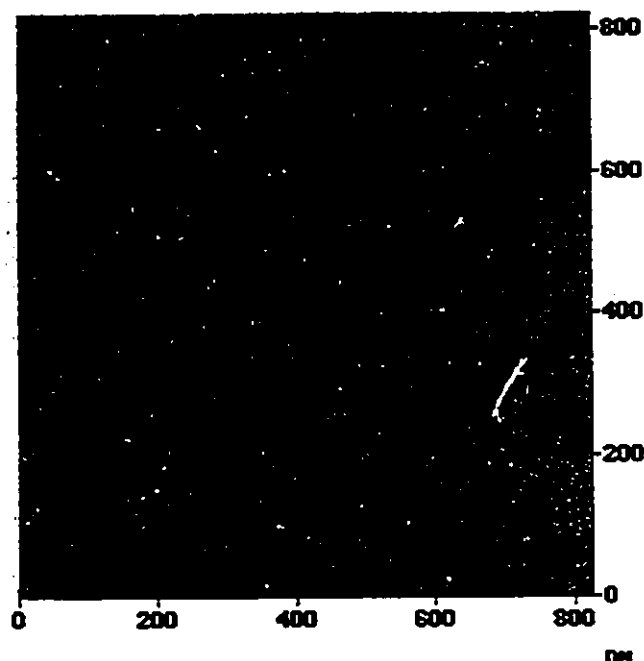


Figure 5-10 An AFM image of a niobium filament extracted from the wire after an imposed strain of 5.

It is conceivable that the excess stress in the second phase could be relieved in one of two ways. The first possibility is that the second phase could spontaneously nucleate an additional slip dislocation to achieve an elongation $b\cos\theta$. The second possibility is the generation of prismatic loops analogous to the misfit dislocations seen in strained layer structures.

The two phases continue to co-deform to sizes of 10 nm and below which is a remarkable observation. Considering that slip steps on the surface of polished and deformed copper crystals can be seen with an optical microscope, the fact that these second phase filaments are not sheared off during deformation means that the process of slip must be very homogeneous throughout the material. Figure 5-10 is an atomic force microscope image of an extracted niobium filament. If the niobium deforms by rational slip, then the slip steps are too fine to be seen in the AFM images. The diagonal markings on the filament make a

consistent angle of between 53° and 58° with the filament axis. The origin of these striations is not known. This angle does not correspond with any of the primary bcc slip planes so it is unlikely that they are slip steps from the niobium. The (111) plane of <100> textured copper, however, makes an angle of approximately 55° with the wire axis so it is possible that these markings are a result the niobium conforming to the deformation in the copper. It is clear that the resolution of this issue will require a detailed investigation of the nature of the interface by lattice resolution TEM.

There is one final aspect to consider for the contribution it has to the work hardening of the composite. Because the two phases continue to codeform to very large strains, there is necessarily an increase in the interface surface area to second phase volume ratio. This will increase the flow stress by an amount given by (Gil Sevillano et al., 1981):

$$\sigma^{\text{int}} = \frac{d(SA/V)}{d\varepsilon} \gamma \quad (5.16)$$

assuming γ does not vary with strain (see Section 5.2.1). If the second phase is assumed to be cylindrical and deforms by similitude with the wire, then the expressions in Figure 5-11 are valid and the contribution to the flow stress is given by

$$\sigma^{\text{int}} = \left(\frac{-2}{l_0 \exp(\varepsilon/2)} + \frac{2 \exp(\varepsilon/2)}{d_0} \right) \gamma \quad (5.17)$$

The first term quickly becomes negligible and the equation reduces to:

$$\sigma^{\text{int}} = \frac{2\gamma}{d_0} \exp(\varepsilon/2) \quad (5.18)$$

The contribution to the work hardening rate may also be calculated:

$$\theta^{\text{int}} = \frac{d\sigma^{\text{int}}}{d\varepsilon} = \frac{\gamma}{d_0} \exp(\varepsilon/2) \quad (5.19)$$

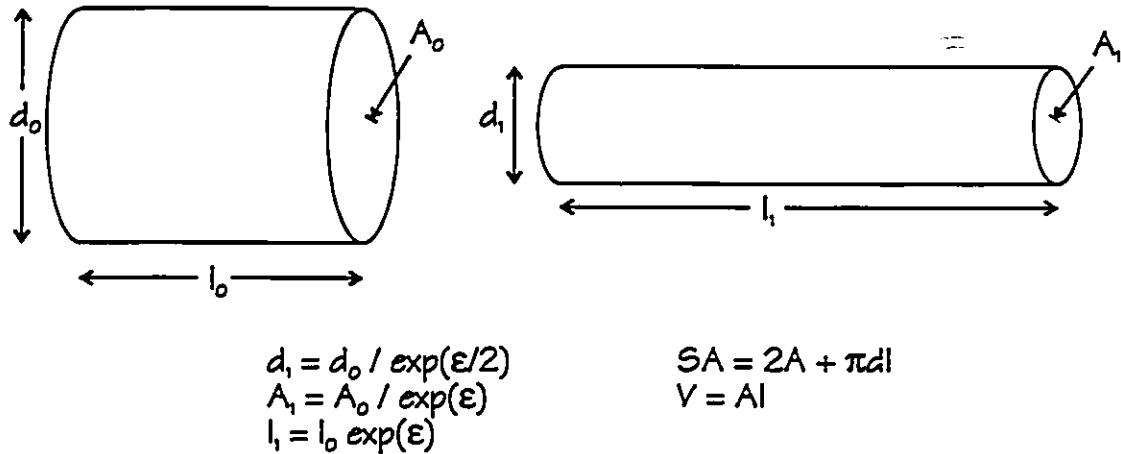


Figure 5-11 The evolution with strain of the surface area to volume ratio of a drawn cylinder.

Care must be taken in employing Equations 5.18 and 5.19 to maintain a physical basis for the calculations. At first glance, it would appear that, with sufficient strain, very large strengths are attainable due to the exponential dependence. However, the physical limit is set, for this geometry, by the quantity $d_1 = \exp(\epsilon/2)/d_o$. As in the case made regarding the minimum spacing of the obstacles, stability considerations would set a lower limit to the filament size.

It is still instructive to apply numbers to Equations 5.18 and 5.19 to explore the limits of this mechanism. If a value of 0.5 J/m^2 is chosen for the interface surface energy and a lower limit for d_1 is set at 5 nm, then the potential increase in strength due to the creation of surface area is 200 MPa and the instantaneous contribution to the hardening rate is 100 MPa.

5.2 Microstructural and Dimensional Stability

In service, the windings of a high-field magnet coil are subject to nominal temperature excursions from 77 to 300K. Due to eddy current heating, however, the skin temperature of the individual windings can reach large fractions of the melting temperature – albeit for very short periods of time. Since the coils are expected to endure thousands of pulses, if the strength of these heavily drawn materials is to be of practical use, it is essential that the factors affecting microstructural stability are understood.

The isochronal annealing experiments performed on the drawn copper-niobium and copper-silver samples revealed classical spheroidization after exposure to temperatures above 300°C for one hour as shown in the micrographs of Figure 5-12. From the model of Nichols and Mullins (1965) described in Section 2.3, Equation 2.28 describes the growth rate of a sinusoidal perturbation on an infinite cylinder assuming interface diffusion is the controlling mechanism.

$$\frac{d\delta}{dt} = \delta \frac{D_I \gamma v \Omega^2}{k T} \omega^2 \left(\frac{1}{r_0^2} - \omega^2 \right)$$

This equation is valid when the amplitude of the perturbation, δ , is small compared to the radius of the cylinder, r_0 . Solutions for large amplitudes require the use of numerical methods. A rough estimate of the spheroidization time, however, may be made by integrating Equation 2.28. Making the substitutions $B(T) = D_I \gamma v \Omega^2 / k T$ and $C(r_0, \omega) = \omega^2 \left(\frac{1}{r_0^2} - \omega^2 \right)$, the rate equation may be written as:

$$\frac{d\delta}{dt} = \delta B(T) \cdot C(r_0, \omega) \quad (5.20)$$

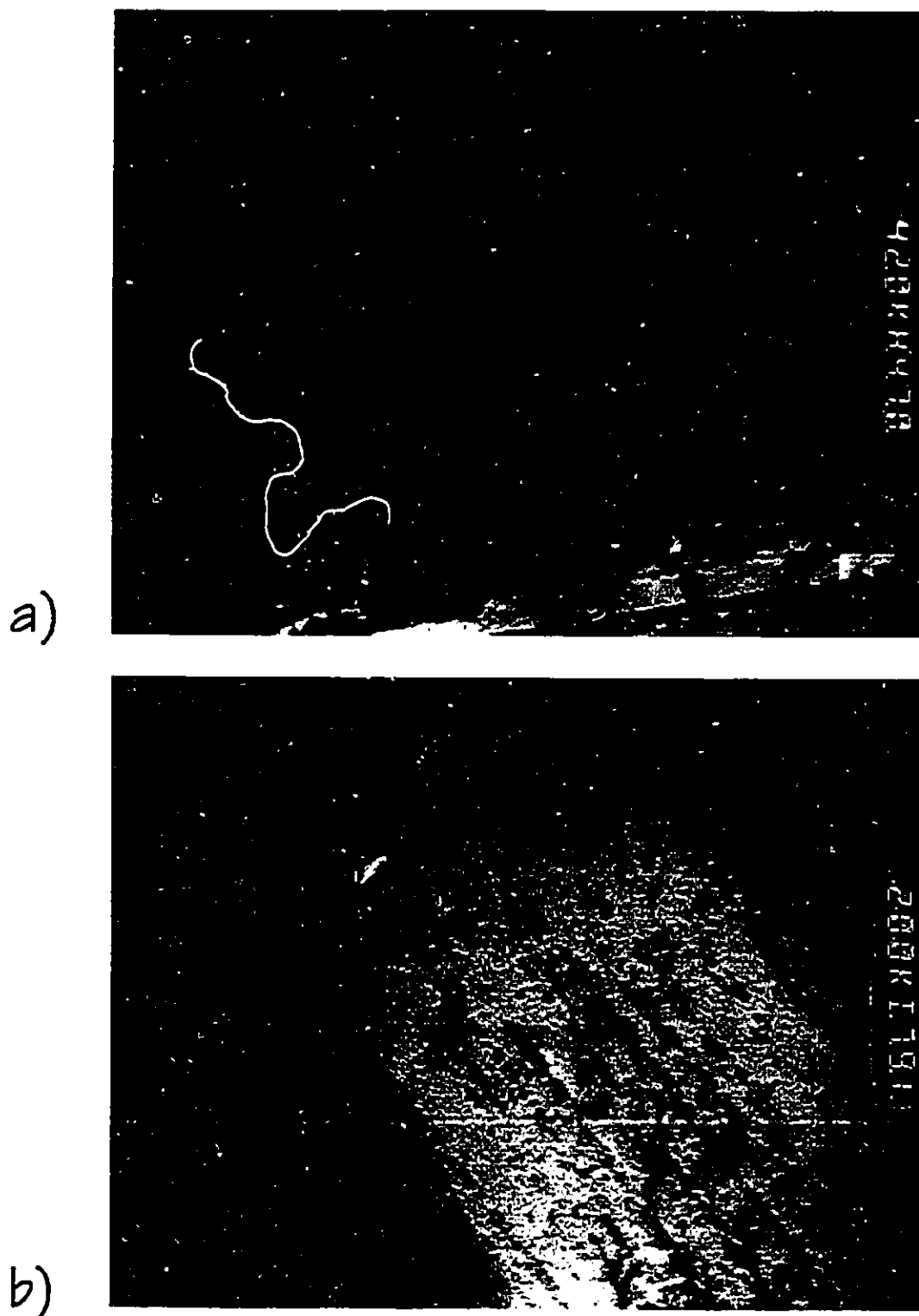


Figure 5-12 Spheroidization of a) niobium and b) silver filaments in a copper matrix after exposure to 400°C for one hour.

Integrating over the entire spheroidization process gives:

$$\int_{\delta_0}^{r_0} \frac{d\delta}{\delta} = B(T) \cdot C(r_0, \omega) \cdot \int_0^{t_s} dt \quad (5.21)$$

$$t_s = \frac{\ln(r_0/\delta_0)}{B(T) \cdot C(r_0, \omega)} \quad (5.22)$$

The appropriate data for the diffusion of niobium at a copper-niobium interface are not commonly found. Thus the question is now one of determining values to substitute into Equation 5.22. Values may be calculated for v and ω with reasonable certainty and estimates may be made for δ_0 , γ , and Ω . The uncertainty remains in choosing the appropriate diffusion coefficients. One approach is to use an interdiffusion coefficient, D_I calculated as:

$$D_I = X_A D_B + X_B D_A \quad (5.23)$$

using the interface, self-diffusion coefficients, D_A and D_B which are more readily estimated, and the relative concentrations of A and B atoms at the interface, X_A and X_B .

Using data obtained from Frost and Ashby [1982], Equation 5.22 was used to estimate the spheroidization times for the copper-niobium and copper-silver systems with various microstructural dimensions. The results are plotted in Figure 5-13, and are in general agreement with the TEM observations that the silver filaments spheroidize at lower temperatures than similar scale niobium filaments. The solution to the spheroidization reaction is based on the reduction of surface energy in the system, and thus the driving force for the reaction enters as the equilibrium surface energy, γ , in Equation 2.3.1. In the case of heavily-drawn, two-phase wires, however, the interface between the two phases will be under traction and the true value of the surface energy is not known. For now, this point

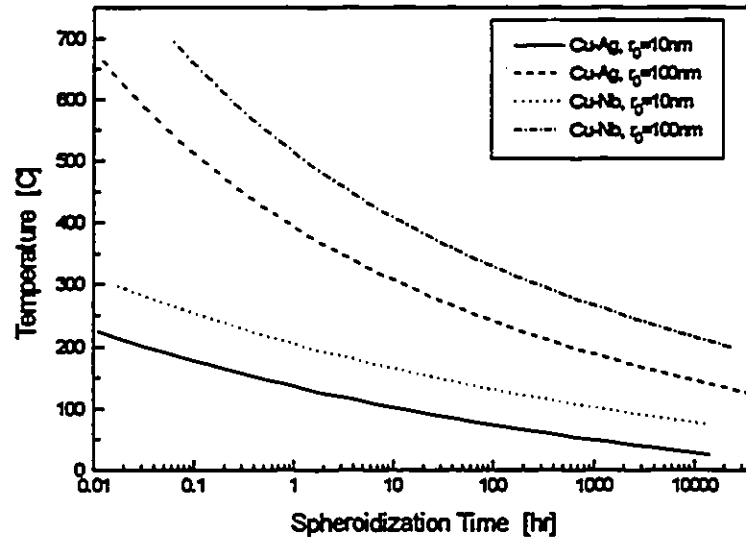


Figure 5-13 Spheroidization times for copper-niobium and copper-silver wires as a function of temperature predicted by Equation 5.22.

will not be considered. Approaches to determining the energy of an interface under traction will be considered in Section 5.2.1.

While spheroidization of silver filaments in the copper-silver wires was observed, the far more prevalent form of instability in the copper-silver system was found to be the discontinuous coarsening reaction shown in Figure 5-14. In the case of drawn, hypoeutectic alloys, as in the study of Sakai et al. (1991), there exist large regions of deformed pure copper adjacent to regions of drawn eutectic. This is a direct result of the as-cast structure of copper dendrites surrounded by the copper-silver eutectic (Cu-60at%Ag). Although there will be energy stored in the areas of pure copper (due to stored dislocations), it will necessarily be less than the energy stored in the drawn eutectic regions because of the extra interphase surface found there. The juxtaposition of these two regions will create a very large gradient of stored energy due to the sharp boundary between them. This energy gradient provides



Figure S-14 Discontinuous coarsening in a Cu-24wt%Ag wire after exposure to 450°C for one hour.

the driving force for the discontinuous coarsening reaction described by Livingston and Cahn (1974) and shown schematically in Figure 5-15.

In their model of a lamellar eutectic, the rate of the discontinuous reaction is given by:

$$V = \frac{8C_b}{(C_\beta - C_\alpha)f_\alpha^2 f_\beta^2} \frac{D_b}{\lambda_2^2} \frac{\gamma v}{\lambda_1 RT} (1 - r^{-1}) \quad (5.24)$$

where C_b is the equilibrium concentration of B atoms on a flat boundary; $C_{\alpha\beta}$ are the concentrations of B atoms in the α and β phases; $f_{\alpha\beta}$ are the volume fractions of the α and β phases; D_b is the boundary diffusion coefficient which includes a boundary thickness correction; $\lambda_{1,2}$ are the wavelengths of the initial and final lamella; γ is the interphase surface energy; v is the molar volume, r is the ratio λ_1/λ_2 ; and RT has its usual meaning. As in the case of the spheroidization reaction, the driving force for this discontinuous reaction is the

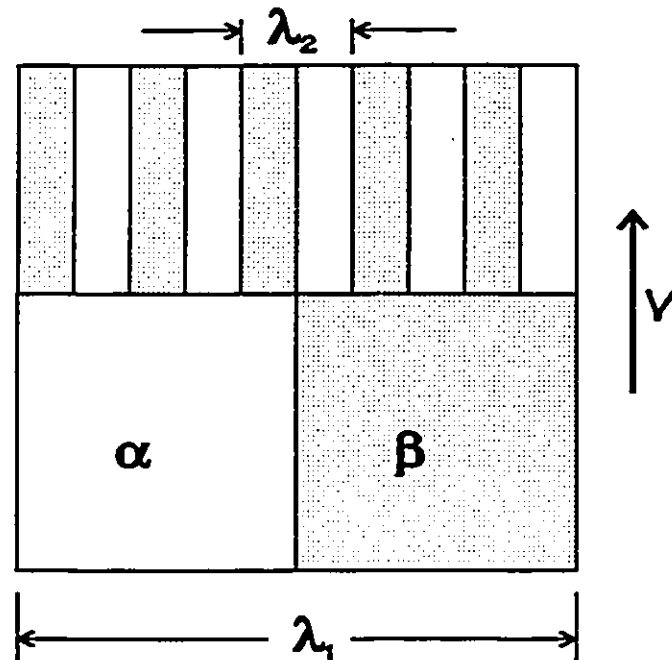


Figure 5-15 A schematic representation of the discontinuous coarsening reaction from Livingston and Cahn, (1974).

reduction in surface area. As was mentioned in the discussion of spheroidization, the correct value of surface energy for a strained interface is not known.

Of equal importance in discussing the rates of the spheroidization and discontinuous coarsening reactions is the potential for nucleation of each event. The data presented in Figure 5-13 for spheroidization times was calculated assuming an initial perturbation, δ_0 , of 3 \AA , which corresponds to a length of roughly 2 Burgers vectors. It is a reasonable assumption that a perturbation of this size would always be present on the surface of the second phase from the co-deformation process.

The discontinuous coarsening reaction, on the other hand, requires a grain boundary from which to grow into the region of higher stored energy. Although the experimental evidence is not conclusive, the observations of no discontinuous coarsening in the homoge-

neous, copper-niobium wires or in the central areas of drawn copper-silver eutectic, but only from boundaries of silver-free regions in the eutectic, suggest that the nucleation time for the discontinuous coarsening reaction is not negligible. In light of the observations to be discussed in Section 5.2.2, there is a need for further study of this reaction.

5.2.1 The Energy of Strained Interfaces

In co-deforming materials, there are essentially two processes which may occur at the interface which will affect the stored energy of the system, (Greer, 1993). If the second phase deforms ideally with the matrix, then the total surface area will change, but the nature of the interface will remain the same. In this case, the appropriate interfacial energy is the equilibrium value, and the work done is $\gamma d(SA)/dV$, as it was calculated at the end of Section 5.1.3.2. If, however, the co-deformation leaves dislocation debris or other sources of elastic stress at the interface, the interfacial energy will be greater than the equilibrium value.

The origin of the residual stress on the interface is important in any calculation of the energy associated with it. Depending on the magnitude of the strain, the energy may be minimized through coherency-type distortions of the lattice, while at higher strains, the formation of dislocations at the interface may minimize the overall energy. Estimates of the correction to the equilibrium interfacial energy (Greer, 1993; Brechet, 1993) suggest that the strained interface may have a free energy of the order of twice the equilibrium value. Due to the nature of the coarsening process and the range of temperatures over which it can occur, calorimetric measurement of these energies prove difficult. However, in conjunction

with direct lattice imaging via TEM, better estimates may be made of both the mechanism and magnitude of the energy increase.

5.2.2 Intermediate Heat Treatments

The reorientation and change in scale caused by the discontinuous coarsening in the copper-silver system can explain the increased work hardening seen in the data of Sakai et al. (1992) on drawn wires subject to intermediate heat treatments. The process described by Sakai et al. involves drawing to 40% reduction in area, annealing the material for one hour at 450°C, and then redrawing. A similar annealing treatment was also performed after 75% reduction in area.

Microstructural observations have revealed that the copper-silver wires begin with an as-cast structure of randomly oriented eutectic colonies which align with the wire axis on drawing. The initial, high work hardening rate is associated with this alignment process. The subsequent, lower hardening rate is associated with the refinement of the aligned microstructure. The observation of the increased work hardening rate accompanied by a decrease in strength following intermediate annealing treatments has led to an attempt to model this behaviour in terms of “renewing” the materials ability to work harden by returning a portion of the drawn structure to its “initial”, misaligned state.

To provide a basic framework for a model of this behaviour, let us consider a simple, two-stage linear approximation of the flow curve for the initial and subsequent rates of work hardening as shown in Figure 5-16 based on the data of Sakai et al. The slope of the two stages may be determined from the data for the non-heat-treated sample. The effect of an intermediate annealing treatment would be to restore some fraction of the microstructure to

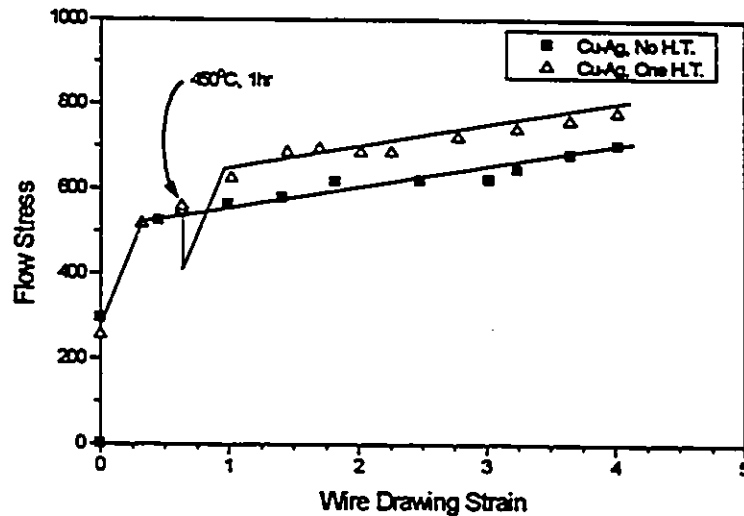


Figure 5-16 A two-stage, linear hardening model base on the data of Sakai et al. (1992). See text for a description of the modelling methodology.

its “original” state causing both a decrease in flow stress and a return to the initial higher work hardening rate. The extremes to this approach would be a) 0% recrystallization with no drop in flow stress or change in hardening rate; and b) 100% recrystallization in which case the flow stress would return to the as-cast value and the extent of the initial hardening rate would be fully restored. A degree of recrystallization between these two extremes can be approximated as a fractional drop in flow stress and a partial return to the initial hardening rate.

There is currently insufficient data to predict the magnitude of the drop in flow stress with percent recrystallization. Tensile tests on copper-silver wires drawn to 40% reduction in area have shown a drop in ultimate strength of 150 MPa after annealing at 450°C for one hour. If the assumption is made that a similar drop in flow stress occurs, the modelling

methodology may be applied. The results are plotted in Figure 5-16 for the wire which was given one intermediate heat treatment, and shows reasonable agreement.

The details of this approach to modelling the effects of intermediate heat treatments in the copper-silver system require further attention, and considerable additional experimental work is required for its verification. The key element of this work, however, is the observation that similar strength levels may be obtained through a variety of thermo-mechanical treatments and thus there is the potential for optimization of the processing technique. This point will be considered again in the next Chapter.

5.3 Electrical Resistivity

The experimental work in this thesis was not primarily concerned with the measurement of electrical resistivity. The combination of strength and resistivity, however, are of prime importance for the construction of high-field magnets and thus, it is useful to make some general comments regarding the effects of microstructural scale on the resistivity.

It is worthwhile, at this point, to reconsider the various resistive mechanisms discussed in Chapter 2 in light of the data collected in this work and in the literature. At temperatures greater than roughly 20 K, the phonon contribution to resistivity typically dominates the overall resistivity. It is often useful, therefore, to examine the resistivity at liquid helium temperature so that observations may be made on the other contributions to the total resistivity.

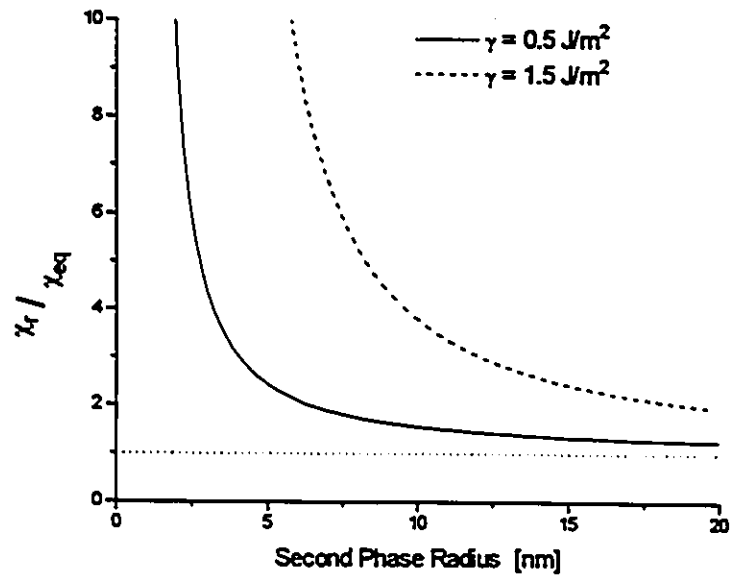


Figure 5-17 The effect of second phase radius on the concentration of niobium atoms in the copper matrix.

5.3.1 Solute Concentration

In general, the measurements made in this thesis with regard to the effects of imposed strain on resistivity should not be affected by solute content because the measurements were made on samples drawn from the same starting material and, therefore, each sample will have the same concentration of impurities. The possible exception to this was discussed by Greer (1993) with regard to the heavily drawn, two-phase materials. Due to the very fine scales attained by the second phase, it is possible that capillarity effects could drive a greater than equilibrium concentration of second phase atoms into solution in the matrix. Greer presents the formula:

$$\ln \left(\frac{(\chi_a^B)_r}{(\chi_a^B)_{r=\infty}} \right) = \frac{V_B^B}{RT} \left(\frac{2\gamma}{r} \right) \quad (5.25)$$

where χ_{α}^B is the mole fraction of B atoms in the α phase, V_{β}^B is the molar volume of B atoms in the β phase, γ is the interfacial energy, and r is the radius of the interface. The ratio of $(\chi_{\alpha}^B)_{\infty}/(\chi_{\alpha}^B)_{\infty}$ is plotted as a function of second phase radius and surface energy in Figure 5-17, and illustrates that the change in concentration can be significant. In terms of the effect on the electrical properties of the wire, if an additional one atomic percent were forced into solution, an increase of the order of 0.1 to 1 $\mu\Omega\text{-cm}$ could be expected in the bulk resistivity.

5.3.2 Dislocation Density

In pure materials such as copper, even order of magnitude estimates of the dislocation density based on changes in resistivity are difficult without extremely accurate measurements. For example, the measurements made here indicate an increase in resistivity of 0.007 $\mu\Omega\text{-cm}$ which would correspond to an increase in dislocation density of 10^{10} to 10^{11} cm^{-2} (Basinski and Saimoto, 1967). The estimated error of 1 to 2% due to the shape factor measurement, however, translates directly to the dislocation density calculation as $\pm 10^9 \text{ cm}^{-2}$. It is difficult, therefore, to draw any hard conclusions with regard to this data. In the case of pure copper, however, it is reasonable to explain the increase in resistivity by an increase in dislocation density, simply because of the lack of other available scattering mechanisms.

5.3.3 Interface Scattering

In heavily drawn, two-phase materials, the effects of interface scattering appear to dominate the bulk resistivity. Frommeyer and Wassermann (1975b) found reasonable agreement between their data on drawn Cu-60at%Ag and the interface scattering model of

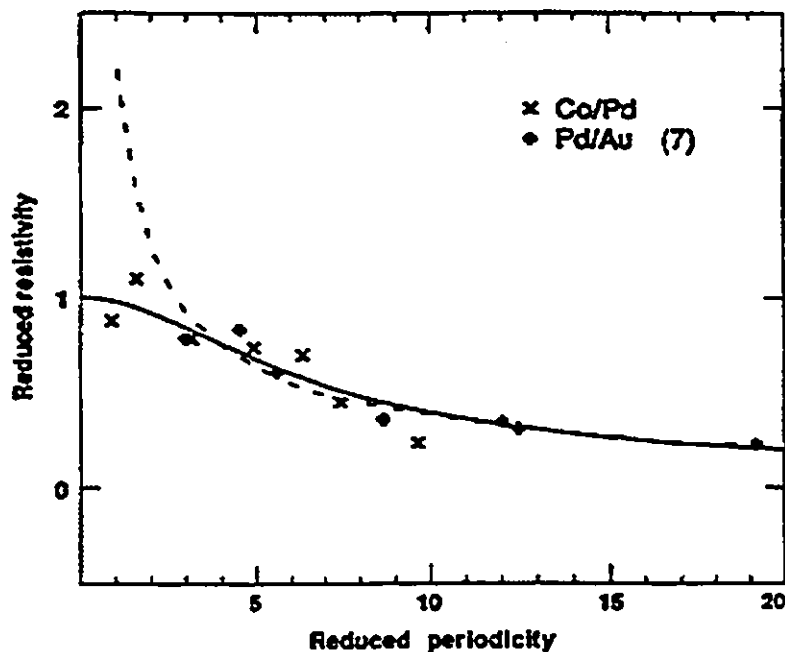


Figure 5-18 The models of Dingle (1950) and Sondheimer (1952), Skomski et al. (1992), and experimental data for resistivity as a function of microstructural scale.

Dingle (1950) and Sondheimer (1952) discussed in Chapter 2. There are, however, two difficulties in applying this type of scattering model. The first arises in determining the value of p ($0 \leq p \leq 1$), the specular scattering factor. Typically, p is chosen to equal 0 which means there is purely diffuse scattering at the interface. Frommeyer and Wassermann found the best fit to their data with $p = 0.15$. The difficulty here is that the value of p is not known *a priori* and the modelling is reduced to a curve fitting exercise.

The second difficulty with this formulation is found in the limit of very fine scale structures where the predicted resistivity goes to infinity. The upper limit should, in fact, be set by the value for the homogeneous solid solution. Skomski et al. (1992) have formulated a model based on this approach which considers the nominally two-phase material as three separate conductors – the α and β phases and an interfacial “phase” of the substitutional solid solution of A and B atoms. This model predicts a plateau in the resistivity

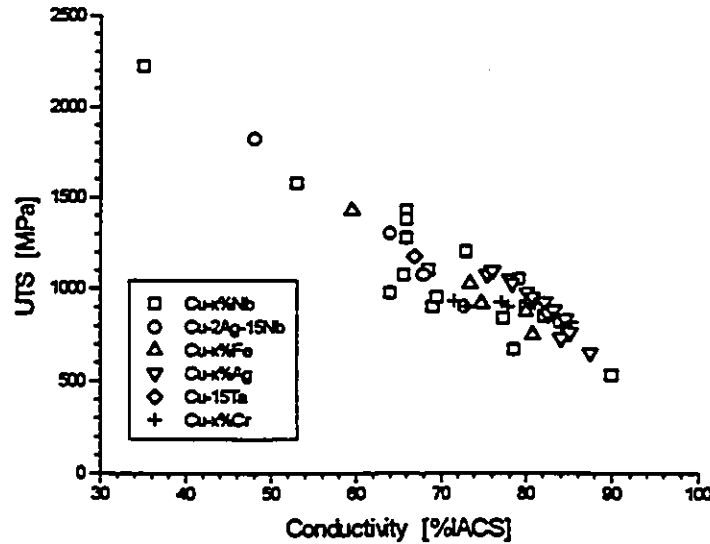


Figure 5-19 A collection of data for high-strength, high-conductivity, two-phase materials showing the general inverse relationship between strength and conductivity

at very fine scales which is in accordance with experimental measurements. Their data is presented in Figure 5-18. This model is still not predictive, however, because it is required to know both the width and the resistivity of the interfacial phase to predict the bulk resistivity.

The general observation which may be made regarding the resistivity of high-strength, two-phase materials is summarized in the graph compiled by Gielisse and Bai, (1993) shown in Figure 5-19. While the strength is proportional to the inverse of the interphase spacing (λ^{-1}), the resistivity is directly proportional to the same spacing which gives rise to the general behaviour shown in Figure 5-19. For use in the construction of high-field magnets, it is preferable to have a winding material with both high strength and high conductivity. As long as the strength and resistivity are governed by the same length scale, it is very unlikely that significant deviation from this behaviour will occur.

6. Materials Selection for Pulsed Magnet Design

The investigations into materials exhibiting a combination of high mechanical strength and high electrical conductivity have led to the representation of the data in the form of graphs of strength versus conductivity. In a similar manner, the requirements of high-field, pulsed magnets for materials with high strength and high conductivity have led to the use of these charts for purposes of comparison and selection of materials. An investigation into the design parameters for pulsed magnets, following the approach of Ashby (1992) outlined in Chapter 2, reveals a more appropriate method of presenting data for both materials selection and the comparison of processing methods. The development of the charts is detailed below.

6.1 Selection Chart Development

The objective in pulsed magnet design is to maximize the generated field. The objective function, therefore, is the equation for the field strength (Equation 2.8) defined in Chapter 2:

$$H_0 = j\lambda a_1 F(\alpha, \beta)$$

The first constraint comes from the requirement of the coil to be able to withstand the Lorentz force generated in the energized coil. For the simple, unsupported coil shown in Figure 2-2, this required strength is given by Equation 2.15:

$$\sigma_y \geq \frac{H_0^2}{F(\alpha, \beta)}$$

This equation yields the first performance index directly, as the equation may be rearranged to solve for the field strength:

$$H \leq \sqrt{\sigma_y F(\alpha, \beta)} \quad (6.1)$$

The first performance index and coupling term are thus:

$$M_1 = \sqrt{\sigma_y} \quad C_1 = \sqrt{F(\alpha, \beta)} \quad (6.2)$$

and to maximize the generated field it is necessary to maximize $\sqrt{\sigma_y}$.

The second constraint is due to the effect of resistive heating. The coil is generally immersed in liquid nitrogen before energizing and there will be a prescribed allowable temperature increase (typically to room temperature) which defines the maximum length of the pulse. As was discussed in Chapter 2, the resistivity and specific heat of materials are temperature dependent; for simplicity, however, room temperature values of these properties will be used here. Assuming adiabatic heating, the temperature increase during the pulse is given by Equation 2.10:

$$\Delta T = \frac{j^2 \rho \lambda t}{c_p d}$$

Rearranging for current density and substituting into the objective function yields:

$$H_0 = \left(\frac{\Delta T \lambda c_p d}{t \rho} \right)^{1/2} a_1 F(\alpha, \beta) \quad (6.3)$$

The second performance index and coupling term are, therefore:

$$M_2 = \left(\frac{c_p d}{\rho} \right)^{1/2} \quad C_2 = \left(\frac{\Delta T \lambda}{t} \right)^{1/2} a_1 F(\alpha, \beta) \quad (6.4)$$

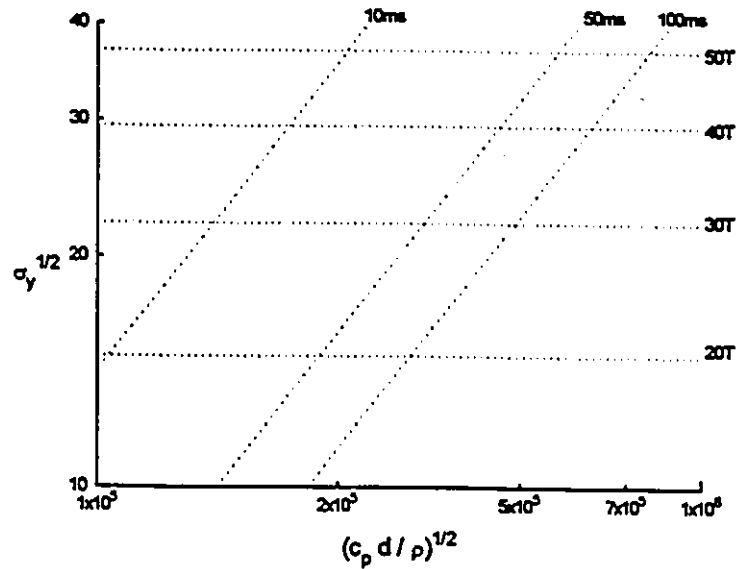


Figure 6-1 The proposed selection chart for high-field, pulsed magnets.

At this point in the analysis, it is important to note that the effects of eddy current heating (proportional to dH/dt) have not been considered, although these can be significant for short pulse times (when dH/dt is large).

This analysis suggests that, rather than axes of strength versus conductivity, materials selection and comparison should be made using charts which plot M_1 vs. M_2 , or $\sqrt{\sigma_y}$ vs. $\sqrt{c_p d / \rho}$. A chart with these axes is shown in Figure 6-1. Because these axes are directly linked to the operation of the magnet, performance lines may also be plotted. Once the geometry of the coil is defined, horizontal lines of attainable field strength may be plotted directly from Equation 6.1. These lines effectively describe minimum strength levels required to generate a given field regardless of pulse time.

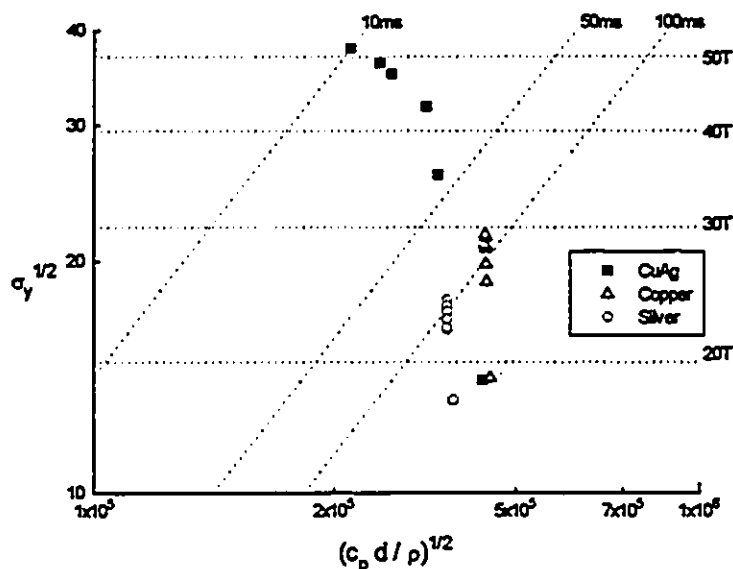


Figure 6-2 The data of Frommeyer and Wassermann (1975a, b) showing the effects of cold work on single and two-phase materials on the materials selection chart.

Coupling lines may also be plotted by combining both constraints as described in Chapter 2. By prescribing the coil geometry, filling factor, and maximum temperature increase, the coupling lines define requirements for given pulse times. For example, assuming the geometry used to construct the selection chart in Figure 6-1, to construct an unsupported coil capable of generating 20T for 50ms, requires a material above the 20T line and to the right of the intersection point of the 20T and 50ms lines.

Again, it is important to point out that this is a somewhat simplified model in that the increased heating due to eddy currents is not considered, nor are the decreased strength requirements that can arise due to external reinforcement and the use of concentric coils to generate large fields. It is possible, however, to extend the method to incorporate these aspects of the design problem.

6.2 Processing and Selection Charts

Having derived the appropriate performance indices and selection charts, their use may be extended to plot the effectiveness of a given processing route and potentially lead to improvements in the manufacturing process. Figure 6-2 plots the data of Frommeyer and Wassermann (1975a,b) on the selection chart for pulsed magnet construction. The data points follow the evolution of properties of pure copper, pure silver and the copper-silver eutectic (Cu-60at%Ag) over a range of imposed strains of 0 to 9.2. The data shows the considerable increase of strength on drawing in the two-phase material compared to the single-phase constituent materials. At the higher strains, however, the same fine scale that leads to high strength also causes a significant increase in resistivity in which interface scattering appears to dominate.

This behaviour can be adequately modelled during the refinement stage by the Hall-Petch prediction of strength and Dingle-Sondheimer predictions of resistivity presented earlier. The results of these models are presented in Figure 6-3 a) as a function of strain for various initial interphase spacings. When the data is plotted on the pulsed magnet selection chart (Figure 6-3 b), several points become apparent and merit emphasis. Because the strength and resistivity are dependent upon the same length scale, their values follow the same path with strain. This underlines the increased efficiency gained by starting with a finer initial microstructure (i.e. the same properties are attainable by conventional casting and extensive cold deformation or by rapid solidification and minimal cold deformation). However, it also illustrates that this combination of material and processing method is limited in terms of producing materials with a range of final properties.

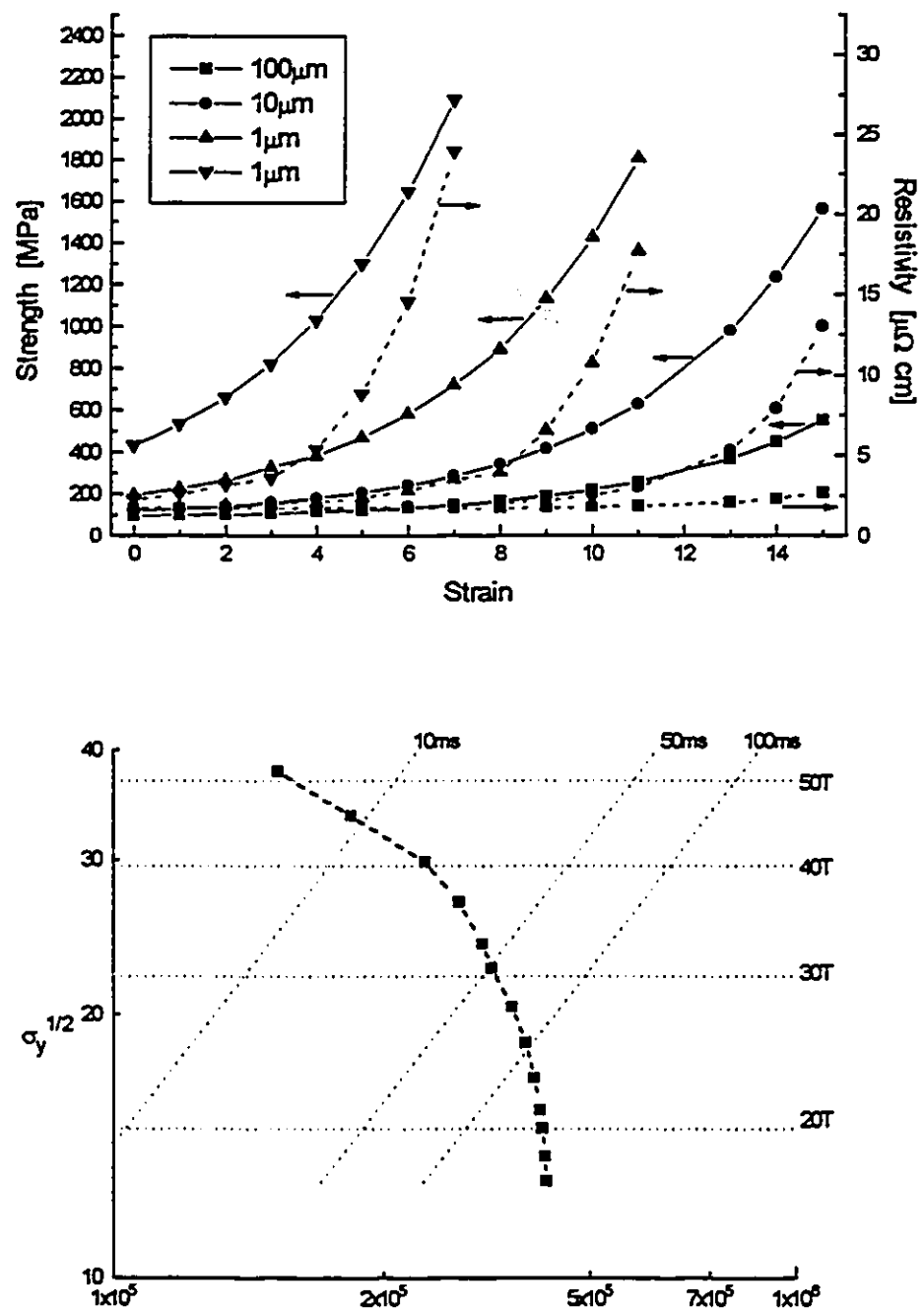


Figure 6-3 Modelled strength and resistivity data plotted a) as functions of strain and b) on the materials selection chart.

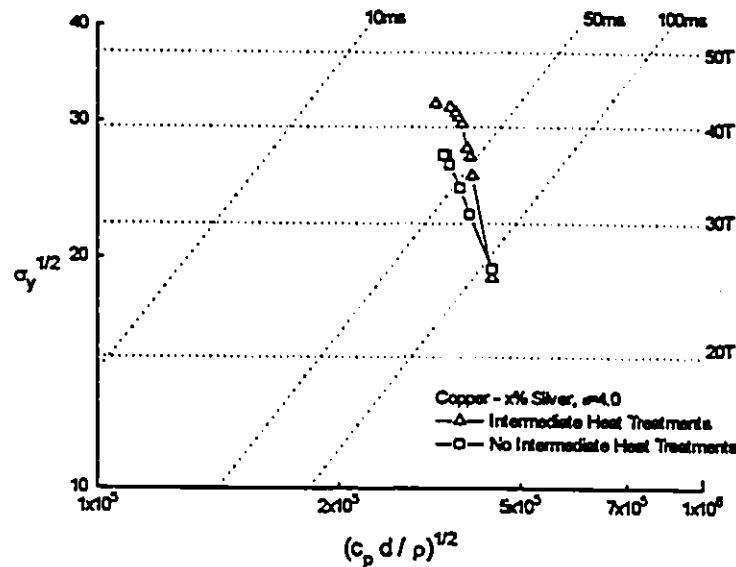


Figure 6-4 The data of Sakai et al. (1992) for copper-silver wires subjected to intermediate heat treatments plotted on the pulsed magnet material selection chart.

In this light, it is interesting to plot the data of Sakai et al. (1992) on the selection chart for pulsed magnets. Figure 6-4 plots data for copper-silver wires drawn to a total strain of $\epsilon = 8.2$. The progression of data points to higher strength levels is the result of increasing the silver content from 0 to 16 atomic percent. The effect of the intermediate heat treatments, as was discussed in Chapter 5, is to temporarily alter the work hardening rate and thereby cause a deviation from the predicted curve to higher strength values at the same value of resistivity.

6.3 Alternate Processing Technologies

The modelling data presented in Figure 6-3 b) suggests that the potential combinations of strength and resistivity in “conventionally” processed, two-phase materials are limited to follow a single curve. This conclusion is also supported by the range of

experimental data presented in Figure 5-19. There are, therefore, three general approaches to the processing of high-strength, high-conductivity materials that may be investigated. The first approach is to alter the initial scale of the composite to optimize the fabrication (e.g., casting and drawing) process. The second alternative involves the optimization of the thermo-mechanical treatments employed by Sakai et al. (1992) which essentially increase the efficiency of the strengthening process without increasing the electrical resistivity. This has been discussed previously in this thesis and will be the subject of future investigation.

The largest potential for gains in high-strength, high-conductivity wires will be made if the strength and resistivity dependence on scale can be decoupled. That is, in the materials studied so far, strength and resistivity have been controlled by the same interphase spacing and thus, an increase in strength could only be achieved at the expense of an increase in resistivity.

A technology currently used in the superconducting wire industry may allow for significant deviations from the predicted curve of Figure 6-3 b). The “jelly-roll” structure shown in Figures 6-5 a) and b) is produced by winding, in this case, a copper and niobium sheet on a copper mandrel as shown in Figure 6-6. This structure is then drawn, bundled with similarly drawn wires, and drawn further to produce the structure shown in Figure 6-5. A simple, descriptive model of these materials can be constructed in the following way.

The strength of the wire can be predicted by a rule-of-mixtures formulation using the copper core and the outer, Cu-X layered shell as:

$$\sigma = \sigma_{\text{core}} V_{\text{core}} + \sigma_{\text{shell}} V_{\text{shell}} \quad (6.5)$$

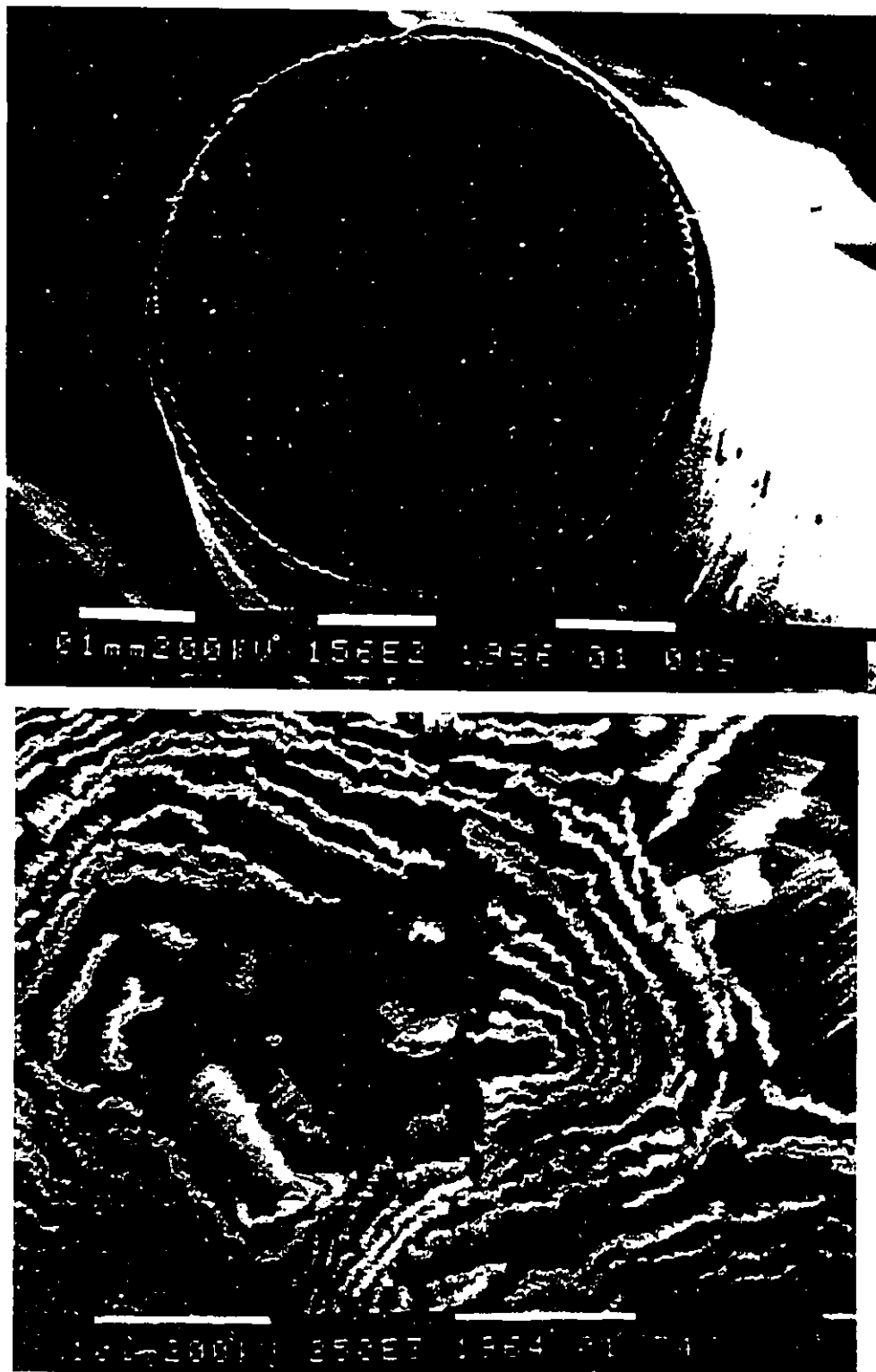


Figure 6-5 Micrographs of the "jelly-roll" structured copper-niobium composite.

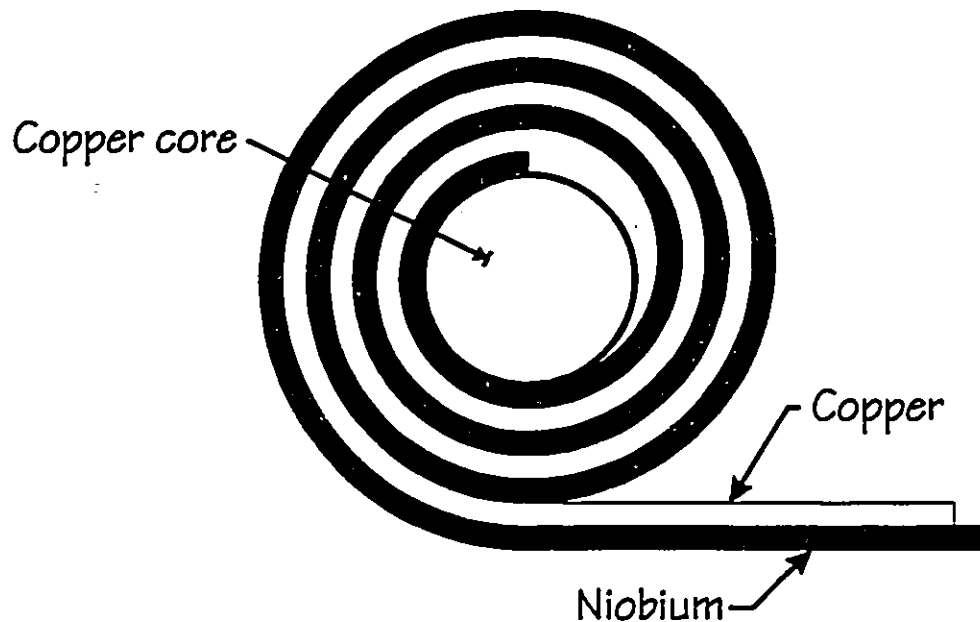


Figure 6-6 A schematic drawing of the “jelly-roll” fabrication technique.

The resistivity can be calculated from a parallel circuit equation, again using the copper core and outer shell.

$$\rho = \frac{\rho_{\text{core}} \rho_{\text{shell}}}{\rho_{\text{core}} V_{\text{shell}} + \rho_{\text{shell}} V_{\text{core}}} \quad (6.6)$$

The characteristic lengths for strength and resistivity are now decoupled — the strength being controlled by the spacing in the outer shell while the resistivity is controlled by the dimensions of the copper core.

Preliminary experimental work on a Cu-18%Nb, jelly-roll wire has indicated that the artificially structured wire has considerably better conductivity at comparable strength levels when compared to the conventionally prepared wire of the same volume fraction (Hill, 1994). Considerably more experimental work is required on these materials to confirm these

results and to explore the stability of these structures. It is possible, however, to construct a preliminary model to explore their potential.

The evolution of strength with strain of the core should be aptly described by that of pure copper. A power-law fit of the data of Frommeyer and Wassermann (1975a) yields the relationship:

$$\sigma_{\text{core}} = 316 \varepsilon^{0.19} \quad (6.7)$$

The strength of the shell can be described by the Hall-Petch formulation described previously. Fitting the parameters to the data of Verhoeven et al. (1989) for a Cu-18wt%Nb composite yields the relationship:

$$\sigma_{\text{shell}} = 100 + \frac{980}{\sqrt{\lambda_0}} \exp(\varepsilon/4) \quad (6.8)$$

and thus the strength of the total wire would be described by:

$$\sigma = V_{\text{shell}} \left[100 + \frac{980}{\sqrt{\lambda_0}} \exp(\varepsilon/4) \right] + V_{\text{core}} 316 \varepsilon^{0.19} \quad (6.9)$$

The resistivity of the core can be taken to be that of pure copper, as work hardening will have a negligible effect compared to the effects of interface scattering. The resistivity of the shell will be described by Equation 2.33, and thus the resistivity of the wire will be described by:

$$\rho = \begin{cases} \rho_{\text{core}} \left[\frac{1 + 0.75 \frac{\bar{x}}{\lambda_0} \exp(\varepsilon/2)}{V_{\text{shell}} + V_{\text{core}} (1 + 0.75 \frac{\bar{x}}{\lambda_0} \exp(\varepsilon/2))} \right] & \lambda \gg \bar{x} \\ \rho_{\text{core}} \left[\frac{\frac{\bar{x}}{\lambda_0} \exp(\varepsilon/2)}{V_{\text{shell}} + V_{\text{core}} \frac{\bar{x}}{\lambda_0} \exp(\varepsilon/2)} \right] & \lambda \ll \bar{x} \end{cases} \quad (6.10)$$

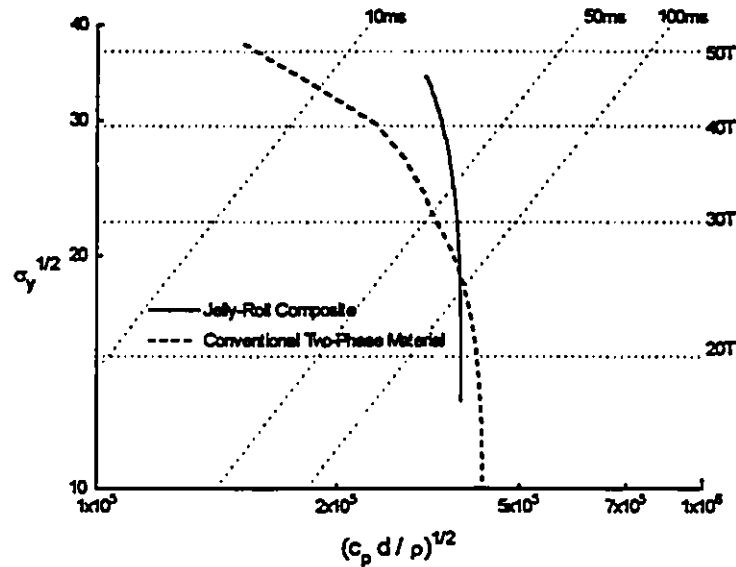


Figure 6-7 The modelled results of the “jelly-roll” structure compared to the conventionally cast and drawn material.

where λ is the microstructural scale and \bar{x} is the mean free path of the electrons. The results of these models are plotted in Figure 6-7 and show the increased potential of the jelly-roll structure over the conventionally cast material.

This approach to materials selection is capable of addressing a wide variety of design applications. It has been shown here to be useful in the design of solenoid magnets for high-field, pulsed operation. The ability to follow the effects of various processing routes on the final properties of a material and relate this directly to the performance of the design is of value, not only for optimizing particular processing methods, but also for indicating novel approaches to manufacturing techniques.

7. Conclusions and Future Work

The objectives of the work outlined in this thesis were set out in Chapter 1. They were:

1. To develop a methodology for optimizing the selection of materials for high-field, pulsed magnets.
2. To identify the mechanism(s) responsible for the evolution of the mechanical and electrical properties of these high-strength, high-conductivity, two-phase materials produced by wire drawing.
3. To investigate the stability of these materials related to changes in temperature.
4. To relate the desired properties to processing variables and thus to help optimize the processing route and, if possible, increase the efficiency of producing the desired final product.

This brief chapter will consider the extent to which these objectives have been met and suggest directions for future research.

Materials Selection

The materials selection procedure of Ashby (1992) has proved to be useful in providing performance indices for the construction of high-field, pulsed magnets. The

development presented in this thesis allows the direct comparison of materials in terms of the design objectives, and also enables a comparison of processing techniques. The approach could be readily extended to consider aspects of design such as the ability to incorporate the effect of reinforced solenoids or multiple (concentric) coil systems. In addition, factors such as eddy current losses or the incorporation of temperature dependent material properties would make the analysis more complex and may perhaps yield alternative selection parameters which are appropriate for other modes of utilization.

Strengthening Mechanisms

It has proved useful to describe the morphological evolution of heavily-drawn, two-phase materials in terms of two regimes — *alignment* ($\epsilon \leq 1$) and *refinement* ($\epsilon \geq 1$). The alignment regime is characterized by a high work hardening rate which may be explained by continuum arguments regarding the average slip line length. The refinement regime covers a very wide range of imposed strain; the present work has allowed a series of conclusions to be drawn regarding the operative strengthening mechanisms in this regime.

The key observations made here regard the sustained co-deformation of the two phases, from which a number of conclusions follow. First, the continued co-deformation indicates that the second phase must be shearable and, therefore, act as a “soft” obstacle to dislocation motion in the matrix. This does not necessarily imply that the second phase deforms by rational slip and, in fact, AFM observations made on extracted niobium filaments suggest that the bcc niobium accommodates the imposed deformation of the copper matrix. This behaviour contradicts strengthening models based on geometrically necessary dislocations due to incompatible deformation in the two phases and those based on dislocation pile-ups in the matrix due to impenetrable obstacles.

In order to explain the high strengths attained in these materials, the classical particle shearing model requires that the interfacial energy of the sheared phase be two to three times greater than the equilibrium value. While the interfacial energy is experimentally very difficult to measure, the large elastic stress borne by the second phase suggests that doubling the effective surface energy due to the imposed traction is not unreasonable, and has, in fact, been predicted by various researchers (Greer, 1993; Embury and Hirth, 1994). The increase in interfacial energy could be explained in terms of interface dislocations which will arise due to the debris caused by the Burger's vector mismatch between the two phases, and/or misfit dislocations created in a manner analogous to those found in strained layer structures. It would be particularly useful to investigate the nature of the interface by high-resolution TEM to gain a better understanding of the energy associated with it.

There are a number of additional aspects of these two-phase materials that have not yet been explored, but merit investigation. In reaching these very high strength levels, the drawing process enforces stable deformation well beyond the Considere point of mechanical instability in tension. Thus it would be of practical and academic interest to understand the failure process and the organization of deformation in the neck under tensile loading conditions.

The combination of fcc and bcc phases in the copper-niobium wire will also permit interesting experiments relating to the deformation of two-phase materials because changes in temperature will change the flow stress of the niobium without significantly altering the flow stress of the copper-matrix. The possibility exists to probe the co-deformation process by altering the drawing temperature (and, therefore, the relative flow stress of the two components); to investigate the temperature dependence of mechanical properties of a given

microstructure; and to explore the effects of temperature and scale on the failure mechanism. At low temperatures, it is expected that the bcc niobium will fail by cleavage. If the niobium is fine enough, it is possible that cleavage will be avoided.

Resistivity

In fine-scale, two-phase structures, resistivity has been shown to increase significantly with decreasing interphase spacing, although a truly predictive model does not exist for this phenomenon. Because the strength of the wire also depends on the interphase spacing, it is important to understand the true nature of the dependence of resistivity on microstructural scale so that the combination of strength and resistivity may be tailored to a particular use (e.g. high-field magnets). The current thin film fabrication technology has been developed to the point that it is possible to create well-defined, layered structures. It would be beneficial to the understanding of the interface scattering mechanism to fabricate two-phase, layered structures with various interlayer spacings and material combinations to measure the resistivity as a function of temperature. This type of experiment will alter the relative magnitudes of the experimentally fixed interlayer spacing and the temperature dependent mean free path of the conduction electrons. It would also be of interest to examine the local chemistry of the interface to determine the degree of mixing and possibly gain greater insight into the interface scattering process.

Stability

The copper-silver and copper-niobium alloys, after large strains, become microstructurally unstable at elevated temperatures. The copper-silver alloys begin their transfor-

mation at a slightly lower temperature (200 – 250°C) than the copper niobium alloys (250 – 300°C). In all cases, the copper matrix begins to recover at approximately 200°C.

In general, the niobium filaments spheroidize at elevated temperatures while the silver in the copper-silver structure discontinuously coarsens. It is not known if this is controlled by the relative diffusion rates or by the density of potential nucleation sites. An interesting experiment would be to anneal the Cu-Ag eutectic (with no silver-free regions) and compare this with an artificially produced microstructure with regions of pure copper beside copper-niobium to determine the importance of these aspects. It would also be of importance in the processing of these materials to investigate the kinetics of the spheroidization and discontinuous coarsening reactions at various temperatures as functions of both imposed strain and microstructural scale.

The increased work hardening observed by Sakai et al. (1992) after intermediate annealing treatments may be explained in terms of the misaligned microstructure produced by the discontinuous reaction which, when subsequently deformed, work hardens at a higher rate. A simple model has been developed to describe this behaviour. Intermediate annealing appears to provide a means of altering the potential combinations of strength and resistivity in the copper-silver alloys. Further experimental work is required to determine if this process is controllable and, therefore, able to be optimized to produce wires with prescribed combinations of mechanical and electrical properties.

Materials Processing and Design

The combination of materials selection procedures and investigations into the strengthening and resistive mechanisms has led to a new approach to the design of

non-uniform composites such as the “jelly-roll” structure to optimize strength and resistivity in two-phase materials. Potential also exists to engineer materials to optimize other combinations of properties. For example, a wire could be designed to minimize eddy current losses by sheathing a copper-niobium composite with a pure copper layer to minimize the surface resistance. These non-uniform, engineered composites represent new approaches to combining the optimization of processing and function, and are worthy of further consideration.

References

- M. F. Ashby: in *Strengthening Mechanisms in Crystals*, A. Kelly and R.B. Nicholson, eds., Applied Science Publishers, Chapter 3, 1971.
- M. F. Ashby: *Materials Selection in Mechanical Design*, Pergamon Press, Tarrytown, NY, 1992.
- Z. S. Basinski and S. Saimoto: *Can. J. Phys.*, 1967, vol. 45, pp. 1167—76.
- Z. S. Basinski, P. J. Jackson, and M. S. Duesbery: *Phil. Mag.*, 1977, vol. 36 pg.255.
- M. B. Bever, D. L. Holt, and A. L. Titchener: *Progress in Materials Science*, 1973, vol. 17.
- J. Bevk, J. P. Harbison, and J. L. Bell: *J. Appl. Phys.*, 1978, vol. 49, no. 12, pp. 6031—38.
- J. Bevk and K. R. Karasek: in *New Developments and Applications in Composites*, D. Kuhlmann-Wilsdorf and W. C. Harrigan, eds., AIME, Warrendale, PA, 1979.
- Y. Brechet: *Private Communication*, 1993.
- L. M. Brown and R. K. Ham: in *Strengthening Mechanisms in Crystals*, A. Kelly and R. B. Nicholson, eds., Applied Science Publishers, Chapter 2, 1971.
- J. A. Charles and F. A. A. Crane: *Selection and Use of Engineering Materials*, 2nd edition, Butterworth & Co., 1989.
- K. K. Chawla: *Composite Materials*, Springer-Verlag, New York, 1987.

- A. H. Cottrell: *Dislocations and Plastic Flow in Crystals*, Oxford University Press, 1956.
- G. E. Dieter: *Engineering Design: A Materials and Processing Approach*, 2nd edition, McGraw-Hill, 1991.
- R. B. Dingle: *Proc. Roy. Soc. (London)*, 1950, vol. A201, pp. 545—60.
- J. D. Embury and R. M. Fisher: *Acta Metall.*, 1966, vol. 14, no. 2, pp. 147—59.
- J. D. Embury: *Scripta Met. et Mat.*, 1992, vol. 27, pp. 981—986.
- J. D. Embury and J. P. Hirth: *Acta Met. et Mat.*, 1994, vol. 42, no. 6, pp. 2051—56.
- R. K. Everett: *Scripta Met.*, 1988, vol. 22, pp. 1227—30.
- G. Frommeyer and G. Wassermann: *Acta Met.*, 1975a, vol. 23, pp. 1353—60.
- G. Frommeyer and G. Wassermann: *Phys. Stat. Sol. A*, 1975b, vol. 27, pp. 99—105.
- H. J. Frost and M. F. Ashby: *Deformation Mechanism Maps*, 1st edition, Pergamon Press, 1982.
- P. D. Funkenbusch and T. H. Courtney: *Scripta Met.*, 1989, vol. 24, pp. 1719—24.
- J. Gil Sevilliano, P. van Houtte, and E. Aernoudt: *Prog. Mat. Sci.*, 1981, vol. 25, pp. 69—412.
- G. T. Gray III and J. D. Embury: *Mat. Res. Soc. Symp. Proc.*, 1993, vol. 288, pp. 585—590.
- L. Greer: in *Mechanical Properties and Deformation Behaviour of Materials Having Ultra-Fine Microstructures*. M. Nastasi, D.M. Parkin, H. Gleiter, eds. Kluwer Academic Publishers, Boston, 1993, pp. 53—77.

E. O. Hall: *Proc. Roy. Soc. (London)*, 1951, vol. B64, p. 26.

J. P. Harbison and J. Bevk: *J. Appl. Phys.*: 1977, vol. 48, no. 2, pp. 5180—87.

M. A. Hill: Private Communication, 1994.

W. Hodge, R. I. Jaffee, J. G. Dunleavy, and H. R. Ogden: *Metals Trans.*, 1949, vol. 185, pp. 340—41.

W. Hodge, R. A. Happe, and B. W. Gonser: *Wire and Wire Products*, 1951, vol. 26, no. 11 p.1033.

W. F. Hosford Jr: *Trans. Met. Soc. AIME*, 1964, vol. 230, pp. 12—15.

A. Kelly and N. H. Macmillan: *Strong Solids*, 3rd edition, Oxford Science Publications, 1986.

G. Langford: *Metall. Trans. A*, 1977, vol. 8A, pp. 861—875.

C. W. Marschall and R. E. Maringer: *Dimensional Instability: An Introduction*. Pergamon Press, Oxford, 1977.

D. B. Montgomery: *Solenoid Magnet Design*. New York, Wiley-Interscience, 1969.

NHMFL Reports, 1992, vol. 1, No. 1, National High Magnetic Field Laboratory, Tallahassee, Florida. 1992.

F. A. Nichols and W. W. Mullins: *Trans. Met. Soc. AIME.*, 1965, vol. 233, pp. 1840—48.

J. Nutting: in *Proc. 8th Intl. Congress on Electron Microscopy*, 1974, vol. 1, p. 580, Canberra, Australia, 1974.

H. Okamoto and T. B. Massalski: *J. Phase Equil.*, 1991, vol. 12, no. 2, pp. 148—68.

N. J. Petch: *J. Iron and Steel Institute*, 1953, vol. 174, p. 25.

D. A. Porter and K. E. Easterling: *Phase Transformations in Metals and Alloys*, Van Nostrand Reinhold, Berkshire, 1988.

Y. Sakai, K. Inoue, T. Asano, and H. Maeda: *J. Japan Inst. Met.*, 1991, vol. 55, no. 12, pp. 1382—91.

Y. Sakai, K. Inoue, T. Asano, and H. Maeda: *IEEE Trans. Mag.*, 1992, vol. 28, no. 1, pp. 888—91.

J. R. Sims, T. Dominguez, T. E. Northington, M. D. Pacheco, D. G. Rickel, E. L. Robinson, J. D. Rogers, and J. B. Schillig: 1993, presented at the *13th Intl. Conf. on Magnet Technology*, Sept. 20—24, Victoria, BC, Canada.

R. Skomski, M. Enrech, and J. M. D. Coey: *Nanostructured Materials*, 1992, vol. 1, pp. 337—45.

E. H. Sondheimer: *Adv. Phys.*, 1952, vol. 1, p. 1.

W. A. Spitzig, A. R. Pelton, and F. C. Labs: *Acta Metall.*, 1987i, vol. 35, no. 10, pp. 2427—42.

W. A. Spitzig and P. D. Krotz: *Scripta Met.*, 1987ii, vol. 21, pp. 1143—46.

W. A. Spitzig and P. D. Krotz: *Acta Met.*, 1988, vol. 36, no. 7, pp. 1709—15.

W. A. Spitzig, J. D. Verhoeven, C. L. Trybus, and L. S. Chumbley: *Scripta Met.*, 1990, vol. 24, pp. 1171—1174.

P. R. Subramanian and J. H. Perepezko: *J. Phase Equil.*, 1993, vol. 14, no. 1, pp. 62—75.

J. D. Verhoeven, F. A. Schmidt, E. D. Gibson, and W. A. Spitzig: *J. of Metals*, 1986, vol. 38, no. 9, pp. 20—24.

J. D. Verhoeven, W. A. Spitzig, F. A. Schmidt, P. D. Krotz, and E. D. Gibson: *J. Mat. Sci.*, 1989, vol. 24, pp. 1015—1020.

Weatherly, G.C. *Treatise on Materials Science and Technology*, 8, pg 121, 1975.

Weiss, R.J., *Solid State Physics for Metallurgists*. Pergamon Press, Oxford, 1963.